2019

Two-dimensional magnetohydrodynamic modeling of cylindrical plasma jets confined magneto-inertial fusion targets

Seth Thompson

Two-Dimensional Magnetohydrodynamic Modeling of Cylindrical Plasma Jets Confined Magneto-Inertial Fusion Targets

by

Seth Thompson

A Dissertation

Submitted in partial fulfillment of the requirements
For the degree of Doctor of Philosophy
in
The Department of Mechanical and Aerospace Engineering
of
The School of Graduate Studies
of
The University of Alabama in Huntsville

HUNTSVILLE, ALABAMA

2019

In presenting this thesis in partial fulfillment of the requirements for a doctor of philosophy degree from The University of Alabama in Huntsville, I agree that the Library of this University shall make it freely available for inspection. I further agree that permission for extensive copying for scholarly purposes may be granted by my advisor or, in his/her absence, by the Chair of the Department or the Dean of the School of Graduate Studies. It is also understood that due recognition shall be given to me and to The University of Alabama in Huntsville in any scholarly use which may be made of any material in this thesis.

Seth Thompson 16 Dec 2019

(student signature) (date)

DISSERTATION APPROVAL FORM

Submitted by Seth Thompson in partial fulfillment of the requirements for the degree of Doctor of Philosophy in Aerospace Systems Engineering and accepted on behalf of the Faculty of the School of Graduate Studies by the thesis committee.

We, the undersigned members of the Graduate Faculty of the University of Alabama in Huntsville, certify that we have advised and/or supervised the candidate on the work described in this thesis. We further certify that we have reviewed the thesis manuscript and approve it in partial fulfillment of the requirements of the degree of Doctor of Philosophy of in Aerospace Systems Engineering.

Dr. Jason T. Cassibry — 12/9/19 (Date) — Committee Chair

Dr. Kader Frendi — 12/13/19 (Date) — Committee Member

Dr. Babak Shotorban — 12/9/19 (Date) — Committee Member

Dr. Qiang Hu — 12/6/2019 (Date) — Committee Member

Dr. Mark Gilmore — 12/13/19 (Date) — Committee Member

Dr. Keith Hollingsworth — 12/17/19 (Date) — Department Chair

Dr. Shankar Mahalingam — 12/18/19 (Date) — College Dean

Dr. David Berkowitz — 12/19/19 (Date) — Graduate Dean

ABSTRACT
The School of Graduate Studies
The University of Alabama in Huntsville

Degree Doctor of Philosophy College/Dept. Engineering/Mechanical and Aerospace Engineering

Name of Candidate Seth Thompson
Two-Dimensional Magnetohydrodynamic Modeling of Cylindrical Plasma Liner Driving Magneto-Inertial Fusion Targets

A set of 2D time-dependent simulations of an imploding cylindrical target and liner are presented. The 2D model developed for this dissertation was used to evaluate these assumptions and explore the ignition space for PJMIF in cylindrical geometries. The 2D magnetohydrodynamic (MHD) model was discretized using smoothed particle hydrodynamics (SPH). The energy term within the equations was augmented with three volumetric power models, including the fusion power produced by alpha particle heating, Bremsstrahlung radiation, and thermal conduction. The original power balance models guided the choice of a reference case for the new 2D MHD simulation. This baseline case consisted of a cylindrical target and liner with a hot inner target at a temperature of 5 keV compressed by a cold multilayer liner at 2.5 eV. The multilayer liner consisted of an inner layer of deuterium and tritium (DT) and an outer thicker layer of Argon to act as a confinement device. The initial density and radius of the target were 5.5 kg/m^3 and 30 cm giving a $\rho R = 0.165$ g/cm^2. The reference case produced a gain of three. A parametric analysis was then conducted, varying the target: density, temperature, radius, and liner inner/outer thickness ratio to understand scaling of gain sensitivity while assessing the assumptions of simpler models that have established the original motivations and theoretical underpinnings of PJMIF and more generally MIF.

This work did not find a region in which compression by a plasma liner was capable of bringing a target to ignition conditions. However, it was determined that a multilayer plasma liner was able to contain a thermally conditioned target and allow it to achieve fusion ignition and positive gain. Numerical analysis indicated that energy conducted from the target to the inner liner was able to ignite the inner liner DT. Liner ignition enabled the overall fusion gain to increase and shows that secondary burn of a surrounding cold fuel layer is possible. It was found that thermal conduction from the hotspot to the cold fuel layer was important for this secondary burn. Additionally, a comparison of these results to previous analysis showed agreement between the regions of positive heating.

Abstract Approval:

Committee Chair _____ 12/16/19
(Date)

Department Chair _____ 12/17/19
(Date)

Graduate Dean _____ 12/19/19
(Date)

ACKNOWLEDGEMENTS

I want to thank my family and friends for standing by me while I completed this work. It truly means a lot!

TABLE OF CONTENTS

LIST OF FIGURES

LIST OF TABLES

LIST OF SYMBOLS

SYMBOL	DEFINITION
ρ	Mass density
P	Pressure
v	velocity
$\mathcal{M}$	Stress tensor of magnetic field and pressure
B	Magnetic field
μ_o	Permeability of free space
$\mathcal{I}$	Identity matrix
u	Internal Energy
n_D	Number density of deuterium
n_T	Number density of tritium
$\overline{\sigma v}$	Cross-sectional area of the fusion reaction rate
E_α	Alpha particle fusion reaction energy
η	Deposition fraction
T	Temperature
T_{ev}	Temperature in electron volts
$k_\perp$	Thermal conductivity
k	Boltzmann Constant
n	Number density
ω_{ce}	Electron gyro frequency
τ_e	Electron collision time

λ	Coulomb Logarithm
q	r_{ij}/h_i, the ratio of the particle distance to the smoothing parameter
h_i	Particle smoothing parameter of particle *i*
W	Smoothing function
dW/dr	Smoothing particle spatial derivative
m_i	Mass of a smooth particle
ρ_i	Particles mass density
$\vec{r}_{ij}$	$\vec{r}_i - \vec{r}_j$, distance between particle *i* and particle *j*
R	Radius of the target
M_s	Mass of the system
V	Volume
t	time
q	r/h
e	Basic charge
c	Speed of light
γ	Ratio of specific heats
$\hbar$	Planck's constant
m_e	Mass of electron
$\mathcal{E}_o$	Permittivity of free space
B	Magnetic field
κ	Smoothing length cutoff distance
σ	Normalization factor for interpolant

L	Lagrangian
Ω_{i}	Scale factor for adaptive h_i parameter
a	Speed of sound
MW	Molecular weight
m_a	Mass of molecule
t_{sh}	Hot spot ignition time
t_{con}	Confinement time
th	Liner thickness

CHAPTER 1. INTRODUCTION

1.1 Problem Statement

Our analysis starts with a question: Do multidimensional effects change the predictions of current 0D power balance analysis for estimation of the fusion ignition conditions for small, magnetized, plasma targets? Additionally, do time-dependent effects alter the ignition predictions of past 0D power balance models? Finally, does modeling the effects of magnetohydrodynamics on target compression improve or reduce fusion gain compared to past analysis? A smoothed particle magnetohydrodynamic method was coupled with the power balance model of earlier analysis to investigate fusion ignition conditions, and sensitivities.

Analyses of fusion ignition conditions of a magnetized target compressed by a plasma liner were limited in scope [1] [2] [3] [4] [5]. Before this study, only a few focused investigations had looked at compression of a target to fusion ignition in the region of plasma jets driven magneto-inertial fusion (PJMIF). Previous studies focused on zero-order thermodynamic models that investigated ignition conditions [6] [7] [8] [9] [10] [11] [12] [13] [14]. Trends in modeling have focused on plasma jet merger and liner formation [15] [2] or centered on the creation of plasma targets for use in the PJMIF process. Earlier work used time-independent power balance models to estimate fusion ignition and plasma burn inside magnetized targets [16]. This study extends prior analysis by incorporation of a two-dimensional magnetohydrodynamic method with a fusion power balance model based on Lindl-Widner diagrams [17]. This study created a simple and accurate time-dependent fusion burn model for cylindrical magneto-inertial targets.

A complete power balance model with accurate fluid dynamics provided a mechanism for evaluation of earlier studies and gave new insight into time-dependent compression and fusion reaction phenomena inherent in the MIF process.

1.2 Survey of Previous Engineering and Scientific Work

Initial research into the MIF parameter space started in the 1970s at the Los Alamos National Laboratory [9]. This research primarily focused on the ignition of solid pellets for inertial confinement fusion. The need to understand the necessary conditions for inertial confinement ignition led to the creation of a power balance model. This model focused on the thermodynamic properties of the system. The goal was to find a parameter space that could delineate regions of positive temperature increase versus regions that would not ignite. Kirkpatrick created the first parameter space focused on areal density (ρR) vs. temperature. This ρR parameter space linked the target radius and density to temperature. That research produced what is now known as a Lindl-Widner diagram.

Kirkpatrick continued to explore this parameter space looking at reduced density and larger radius targets with magnetic fields. This parameter space was considered a viable and possibly more straightforward way to achieve fusion ignition within a target. Later research focused on how to build a liner and compress a target. The FRX-L experiments of Sandia and Los Alamos National Labs explored the possibility of a metallic liner to compress a target [18] [19] [20]. Thio and Cassibry looked at the possibility of using PJMIF as a propulsion source for in-space exploration. Significant progress was made in the modeling of plasma jets and their ability to merge and compress into a uniform liner [21] [15] [22]. Initial one-dimensional models of hydrodynamics and power balance had been used to improve the applicability of the L-W diagrams. To date, minimal higher

dimensional modeling of the process had been done. Most of the analysis was focused on the magnetohydrodynamic compression of a target, and neglected the fusion power deposition of energy by alpha particles, loss due to radiation and thermal conduction. This work aimed to incorporate these models into the two-dimensional space and explore the regions of ignition and their sensitivity to specific parameters: target density, target temperature, target radius, and liner DT to argon mixture ratio.

1.3 Objectives of this dissertation

Our goal was to increase the current understanding of ignition conditions for PJMIF. PJMIF might provide a unique approach to break-even fusion [21] [23]. Past research trends had focused on 0D and 1D models of fusion ignition. This work extended previous understanding by the addition of multidimensional magnetohydrodynamic equations into the power balance model. The creation of a multidimensional time-dependent power model increased insight into the time-dependent power transfer processes of the PJMIF target compression and ignition space. The power balance of the target and liner was analyzed using a variety of time-dependent physics. Each process had a time dependence scale that was different for each power model. The mismatched time scales provided a difficult simulation space because the smallest time scale became the dominant parameter and increased simulation times. A graphics processor (GPU) was used to alleviate the challenges posed by the simulation. The GPU allowed for reduced simulation times by parallel calculations of each particle in the smoothed particle hydrodynamic (SPH) simulation that was written specifically for this analysis.

1.4 Summary of the Approach

The model of the PJMIF process worked by simulation of the compression of a plasma target, made of an equal mixture of Deuterium and Tritium (DT). The target had an axial magnetic field to mitigate thermal conduction loss. Initially, the target was hot, but below fusion ignition temperature. The magnetic field within the target provided partial containment of fusion alpha particles and thermal energy. Prevention of alpha particle loss from the system allowed the target to heat up and ignite. The target was compressed and confined by a plasma liner. The liner consisted of two parts, an inner DT liner and an outer liner made of Argon. The inner liner provided additional fuel and a means of capturing lost thermal energy from the target. The target conducted energy to the inner liner, and our simulations utilized this process to heat the inner liner. This analysis found that it was possible to ignite the inner liner and increased the overall fusion gain of a system [24] [25] [26].

Previous models of the ignition process were limited to simplified thermodynamic models that estimated power balances of the heating and cooling aspects of the PJMIF system [7] [8] [9] [10] [11]. Those models estimated the time-dependent processes. Similar to prior analysis, this power balance model for PJMIF ignition had four critical elements: fusion deposition, compressional work, Bremsstrahlung radiation, and thermal conduction. Alpha particle heating was an essential mechanism for fusion ignition. Alpha particles created in a DT reaction have 3.5 MeV of energy, which is three orders of magnitude higher than the target ignition energy [27] [28]. Alpha particles had been the primary source of maintaining and heating the target and inner liner. Capture and control of their energy deposition were mandatory for a system to reach break-even energy

production. The second term incorporated into the power balance model was mechanical work done by compression. This provided the initial "spark" to ignite the fusion reaction and heat the target. The third term was Bremsstrahlung radiation loss. Bremsstrahlung radiation was the primary radiation loss mechanism for the system [9]. The fourth term was the thermal conduction. Thermal conduction was a significant source of thermal loss in the target. The axial magnetic field prevented some of the thermal loss by control of electron motion about the magnetic field lines. Another mechanism that provided a way to utilize thermal loss was to capture it in the inner liner. The capture of the "lost" heat to the inner liner bootstrapped the fusion ignition and gain of the system.

The purpose of our study was to produce time-dependent models of all of the power balance terms using a two-dimensional magneto-hydrodynamic SPH method. Our purpose was to identify an improved space for fusion ignition and identify departures from the ideal 0D models which were previously published. A comparison of these results to the previous thermodynamic analysis provided a way to evaluate both works and gain insight into the time-dependent fusion ignition process for MIF targets.

1.5 Synopsis of the Dissertation

The following chapters will discuss previous work, methodology, results, and conclusion. Chapter two will focus on previous work and relevant literature to the PJMIF parameter space and current trends being researched. Chapter three covers the mathematical models used for the magneto-hydrodynamics, fusion power, radiation, and thermal conduction. Chapter three also contains the test and verification tests for validation of the SPH model. The fourth chapter focuses on the results of this study and its relation back to previous

research done. Finally, a conclusion chapter summarizes the work presented here, its relevance to the greater community, and future analysis that should be performed.

CHAPTER 2. LITERATURE REVIEW

2.1 Related Work

The late 1970s was the conception point for the idea of magnetized target fusion. The Phi experiments were the first magnetized target fusion experiments [17]. In these experiments, a small solid shell containing Deuterium gas was impinged upon by a relativistic electron beam. The beam focused to the size of a pencil caused the shell to explode and implode simultaneously. The electron beam caused a uniform compression, which caused the outer shell to explode and the inner shell to implode upon the deuterium-deuterium (DD) gas. These experiments successfully produced neutrons that were a product of thermal nuclear fusion. Kirkpatrick was exploring the burn physics of inertial confinement targets in these experiments [9] [29] [16]. During that period, Kirkpatrick researched structured target designs for use in electron beam fusion.

A consequence of this research was the need to heat a cold target to high temperatures in a short period. Unfortunately, Kirkpatrick found that as the target heated up and reached ignition conditions, power loss due to conduction and radiation become important [29]. At the time, limited computing power was available, and the need to have a concise physics model drove research into a 0D power balance model [9]. In this work, Kirkpatrick developed a power balance model for modeling small target fusion in a variety of regimes. A simplified hydrodynamic equation was developed to be able to approximate implosion and shock physics. The implosion and shock of a target is

inherently a three-dimensional process but was simplified to a one-dimensional process under proper assumptions [30]. Kirkpatrick noted that a simplified 0D hydrodynamic model is acceptable as long as the significant characteristics of the implosion remain consistent with a more accurate model [31] [32]. Kirkpatrick's assumptions for the power balance were:

1. A DT target was surrounded by a shell of homogenous material.
2. The shell was homogeneous in all properties such that: $\frac{dv}{dr} = 0$, $\frac{d\rho}{dr} = 0$, and $\frac{du}{dr} = 0$.
3. The DT experienced homogeneous compression, $\frac{dv}{dr} = \frac{v}{R}$.
4. Self-compression of the shell had occurred, where $M_s u_s = M_s u_{so} - P dV_s$
5. No external energy was added after $t = 0$

The outcome of that research was a model for mechanical work, which became:

$$\left(\frac{du}{dt}\right)_{work} = P\frac{dV}{dt}. \tag{2-1}$$

Energy would be lost due to radiation and thermal conduction, and produced by fusion reactions based on equal parts DT. The power balance model became:

$$\frac{du}{dt} = \left(\frac{du}{dt}\right)_{work} + \left(\frac{du}{dt}\right)_{fus} - \left(\frac{du}{dt}\right)_{rad} - \left(\frac{du}{dt}\right)_{cond}. \tag{2-2}$$

The power balance includes four terms: compressional work, radiation loss, thermal conduction, and fusion deposition. This work had the first comparison of temperature to density plots called Lindl-Widner diagrams. With this work, Kirkpatrick was able to map out regions of positive fusion yield, which guided experimental and numerical designs. Figure 2-1 shows the L-W diagram for a cylindrical plasma target. The x-axis represents the target's initial starting aerial density, which is a function of target radius and density.

The y-axis is the initial temperature of the target. The grey region is the positive power region calculated from Equation 2-2. L-W diagrams estimate the hydrodynamics by modeling with 0D time-independent physics.

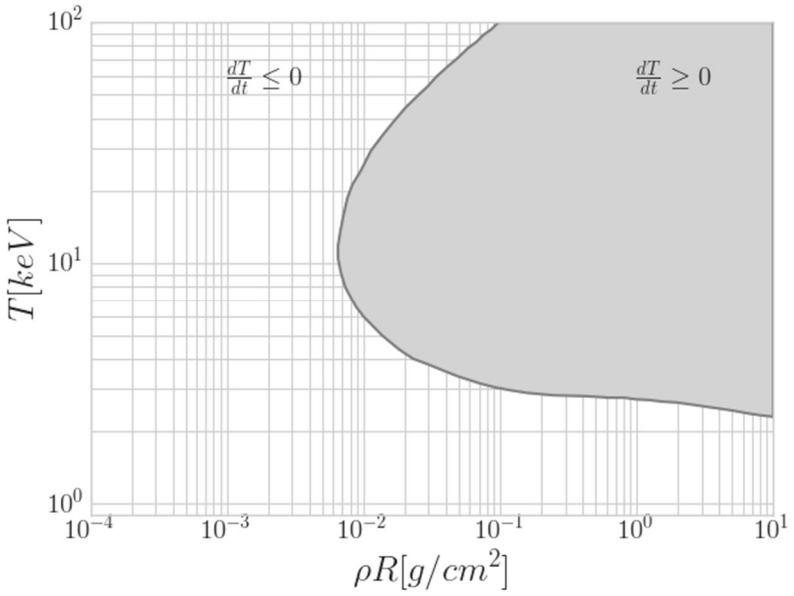

Figure 2-1: Shows a representative Lindl-Widner diagram. This diagram represents the contour space of positive heating for a cylindrical target. The region in grey represents the positive heating area as a function of initial target aerial density and temperature.

Following Kirkpatrick's initial work was Lindemuth who incorporated a magnetic field into the target process [11]. In this work, Lindemuth explored the parameter space for using azimuthal magnetic fields in a spherical target for increasing gain/reducing thermal energy loss. The magnetic field prevented thermal conduction perpendicular to the field lines providing a mechanism to limit the thermal conduction of energy out of the target. Control of the thermal conduction term showed improved system gain. Improved gain

and reduced requirements on implosion drivers opened up the concept of plasma targets in place of solid targets. Lindemuth compared these results to two-dimensional MHD modeling of electron beam imploded solid targets [33] In this work, Lindemuth found that the fuel behavior modeled by a two-dimensional model was in agreement with the results of the power balance model formulated by Kirkpatrick. An undesired outcome of Lindemuth's paper was the recognition that preheating of a target was necessary to achieve ignition conditions [11]. Lindemuth stated that to achieve a 4 keV target temperature by compression of a spherical target required a convergence ratio of at least 100 [11]. Determined during this analysis was that compression alone was insufficient to compress the target to fusion ignition, which is consistent with the results of Lindemuth. Our target is cylindrical, which required more compression due to the scaling of cylinder vs. a sphere [12]. This analysis had a preheated target at 5 keV, which is similar to the requirements Lindemuth set forward in his work [11].

Kirkpatrick's power balance model had been and still is a critical tool for delineating regions of inertial confinement fusion. Lindl used this process to further solid target studies in the late 1980s to improve ICF targets [13]. The early 1990s led to more research into the design of plasma targets with magnetic fields for fusion power [34] [23] [17] and developed the initial concepts for the PLX-alpha and FRL-X experiments.

Extensive research at the beginning of this century led to plasma and metallic liners as driver concepts for magnetized target compression. The FRX-L experiment examined compressing a target with a liner, the formation of a liner, and the formation of a target [18] [19]. Cylindrical targets with an axial magnetic field were explored by Basko and Kemp [6]. In their research, they looked at the travel distance of an alpha particle

produced by a fusion reaction. This travel distance was then related to the magnetic field strength and density of the plasma to determine a time-averaged energy deposition into a target. The deposition model of Basko and Kemp became the basis for the deposition fraction in this analysis. Thompson looked at the same type of dynamics for a spherical target with closed field lines [14]. In that work, it was found that alpha particle heating of a spherical target with a magnetic field would yield positive gain.

Current research trends have focused on the modeling and experimental formation of plasma liners. The Plasma Liner Experiment-Alpha (PLX-α) project is a multi-faceted approach to demonstrating the creation of a plasma target, implosion by stand-off plasma jets and positive fusion gain is an ongoing effort [20] [2] [15]. This research has been working on plasma jet formation, and its viability to form a liner [2] [22].

2.2 Specific Modeling Efforts in PJMIF

This effort focused on the numerical modeling of plasma jets magneto-inertial fusion. While the L-W methodology for outlining spaces of positive yield is important, it estimates the impact of heating and cooling rates without factoring in spatial and temporal processes which continuously evolve during implosion/burn/expansion [29]. A full investigation into their effects wasn't performed and, only recent research into multi-dimensional effects have been explored [5] [2] [3]. The research of Cassibry and Stanic has shown the capability of discrete jets to merge into a uniform liner [2]. In that work, discrete plasma jets arrayed in a spherical setup. The jets were propagated through a vacuum to merge and form a discrete liner. The interesting outcome of the work was that even though discrete jets merged, they were able to form a liner that was consistent with a uniform shell in the ideal model. This work demonstrated that modeling a plasma

liner formation by the merger of plasma jets was able to achieve the desired effect of a uniform merged liner.

One-dimensional models had been used to improve upon the modeling space done by earlier researchers. Recently Langendorf and Hsu showed the capabilities of standoff drivers using the LASNEX software to model spherically imploding targets by plasma jets [35]. In this research, the liner was modeled as a set of equal mass shells. The compression and propagation of the shells were done analytically and used the acceleration of the zonal shell interfaces to calculate changes in energy and pressure in the liner. This research suggested that gains of 3-30 are possible with spherical liners that have a convergence ratio of less than 15 [35]. This work compared its results to previous one-dimensional models and found good agreement between the models. The important outcome was that gains could achieve without the need of "afterburner" which implies fuel burnup by heat transfer from the target to the liner. While the analysis performed here agrees, it is noted that the use of "afterburner" is desirable in improving overall gain.

To date, a few efforts into multi-dimensional models of PJMIF had been published. Parks' et al. looked at simplified models that were not favorable to PJMIF concepts [5] [36]. Their findings used a 1-D quasi-time-dependent model for their study. Parks' research did not find the ability to heat an inner portion of a DT liner to achieve appreciable gain. In that work, Parks's assumed that the only heating mechanism of the liner would be through alpha particle deposition. This assumption neglected the heat transfer by conduction to the target, which is a significant source of energy for the inner liner.

In contrast, this work demonstrated that liner heating is possible and had an impact on total system gain. Parks' work used several assumptions to mimic the effects of cooling by radiation in place of directly modeling it. Specifically, Parks used a reduced specific heat ratio in place of radiation. Their justification was based on previous work that modeled Z-pinch targets using a similar method. While computationally efficient, this led to a need to qualify a reasonable starting point. Without test data, this work left a significant gap in possible solution spaces. The one-dimensional approximations do leave out the interaction of a second dimension, which may be necessary for determining the impacts of instabilities and other hydrodynamic processes.

Thompson and Cassibry were able to corroborate the merger of the experimental jets merger thorough the use of a smoothed particle hydrodynamic method. In that work, the experimental jets merger was modeled using an SPH code and compared favorably to the experimental results. In that work, they found that the numerical modeling of the jets merger and shock region was in agreement with the experiments. Post-shock densities, temperatures, and velocities were in close agreement between the experiment and the numerical analysis. In the PLX-α experiment, an odd low-density region at the center of the jets merger was discovered. This low-density region is an outcome of the jets merger process. Thompson and Cassibry characterized this anomaly and compared a detailed analysis of the formation of a Kelvin-Helmholtz instability to the experimental merger of the jets. Thompson and Cassibry found that this region may be the beginnings of a Kelvin-Helmholtz instability forming but not able to manifest ultimately due to the expansion of the jets.

2.3 Solid liner MIF

The FRL-X methods established a parallel effort. This process focused on using a solid liner such as Beryllium to compress a magnetized target to fusion conditions. The significant difference between efforts is the choice of liner material and implosion methodology [37]. The MagLIF experiment is an ongoing experiment looking to compress a Field Reverse Configuration target by a solid liner [38]. The current modeling research using LASNEX demonstrated that high gain is possible with this concept. Aside from the solid liner a major difference was the use of laser heating to preheat the target to fusion temperatures to help drive the fusion process. Slutz numerically showed that a gain of 100 was possible with their current concept.

2.4 PJMIF Summary

A large body of research into the magnetized target concept has been done over the last 40 years. The experimentation of MIF is still in its infancy and progressing each year. Two parallel concepts have emerged from the initial work of Kirkpatrick et al. Sandia, and Los Alamos National Labs are exploring the concept of a solid liner as the implosion device of a target. The other concept, which is the primary concern of this report, is using standoff plasma jets to compress around a magnetized target and achieve fusion ignition and gains greater than unity. To date, there have been no full scale complete PJMIF experiments; it is hoped that future research and funding will support continued effort for this concept.

CHAPTER 3. METHODS

3.1 Introduction

To answer the questions posed in chapter one: do time-dependent processes affect the power balance of PJMIF? We started with the ideal single fluid magnetohydrodynamics equations to represent the time evolution of the system. The ideal equations represent the conservation of mass, momentum, energy, and charge. They have been used to model fusion power systems from ICF to MCF regimes [27] [25]. We then augmented the time rate of change of the energy term to include the source and sink terms provided by the power balance equation in Equation 2-2. The ideal form of the MHD equations made several assumptions that must be justified to proceed.

The first assumption in the MHD equations was the relative mass of the ions was more substantial than the electron. The mass of an electron is significantly less than the mass of an ion for DT plasmas. The mass ratio difference is on the order of 10^4, with the DT ions inertia controlling fluid flow. Argon being singly ionized and more massive had a more substantial mass difference. The relative velocity between species was small; thus, the fluid moved with the bulk velocity of the ions [25], and the ions towed the electrons. The second assumption was that the fluid was perfectly conducting, and regions of high current concentration are small and negligible in size.

The power balance model used by Kirkpatrick was an idealized Lawson criterion and required four main elements, a compressive work term, a fusion power term, a radiative loss term, and a conduction term. While the power balance is not temporally dependent, our approach was to update the model for time dependence by accounting for each of the four energy terms. The MHD equations already incorporated the mechanical work term through the energy equation. The fusion power, thermal conduction, and radiation became separate models. The PJMIF process did not contact any walls and required only boundary conditions that handle a vacuum. The PJMIF liner and target existed in a vacuum chamber. This made the modeling uniquely suited to the SPH methodology, which required no additional boundary treatments at a vacuum interface.

The loss due to Radiation was modeled using the Bremsstrahlung radiation equation, which was identified as the critical radiative loss term by Kirkpatrick [29] [16] [17]. Thermal conduction was the other loss term; the inner liner of the plasma liner was significantly cooler than the target. This led to thermal conduction loss from the target to the liner. The addition of a magnetic field was used to control thermal conduction [14], based on previous analysis.

The following chapter will introduce and develop the models used in this study. We start off with the augmented ideal MHD equations. These equations incorporated the power balance terms used in the L-W diagrams. The additional models to the MHD equations were developed after the introduction of the MHD equations. Next, we developed the basic theory for the SPH interpolation methodology to orient the reader to SPH concepts. The MHD SPH equations were derived using the Lagrangian formulation given by Price [39] and Vanaverbeke [40]. Once the equations are developed, they were amended to

include artificial terms to stabilize the numerical solution, which are presented in Equations 3-52:3-55. The final form of the equations used in the study are presented with all terms in Equations 3-63:3-66.

3.2 Models for the Governing Equations

The overall goal of this research is to incorporate time dependence into the power balance solutions. The ideal MHD equations of motion were used to represent the evolution of the fluid and magnetic fields. The MHD equations were not derived in this report, but the interested reader is referred to the following excellent references by Chen [27], Goedbloed and Poedts [25], and Goldston and Rutherford [26]. The ideal MHD equations in the Lagrangian form with modification for power balance terms are presented below

$$\frac{d\rho}{dt} = -\rho\left(\vec{\nabla}\cdot\vec{v}\right), \tag{3-1}$$

$$\frac{d\vec{v}}{dt} = \frac{\vec{\nabla}\cdot\mathcal{M}}{\rho}, \tag{3-2}$$

$$\frac{du}{dt} = -\frac{P}{\rho}\left(\vec{\nabla}\cdot\vec{v}\right) + \left(\frac{du}{dt}\right)_{fus} - \left(\frac{du}{dt}\right)_{rad} - \left(\frac{du}{dt}\right)_{cnd}, \tag{3-3}$$

$$\frac{d\vec{B}}{dt} = \left(\vec{B}\cdot\vec{\nabla}\right)\vec{v} - \vec{B}\left(\vec{\nabla}\cdot\vec{v}\right), \tag{3-4}$$

$$\mathcal{M} = \frac{\vec{B}\vec{B}}{\mu_o} - \left(\frac{1}{2}\frac{\vec{B}^2}{\mu_o} + P\right)\mathcal{I}, \tag{3-5}$$

where equation 3-1 is the continuity equation. This equation represents the conservation of mass within the system and models a change in density based on time and spatial relations. Equation 3-2 represents the momentum of the system. Momentum change was effected through either the pressure gradient or magnetic field. Equation 3-3 represents

the internal energy change of the system and is augmented by the additional power balance terms for alpha deposition, Bremsstrahlung radiation, and thermal conduction. Equation 3-4 is the time dependence of the magnetic field, with the magnetic field change based on the geometry of the system evolved in time and space. The final equation 3-5 is the magnetic stress tensor of the system. The fluid pressure and magnetic field create a 3×3 system that has off-axis components that differ from the standard pressure gradient of a hydrodynamic system.

The power balance in Equation 3-3 represents the change of energy; therefore, additional power balance terms are included based on the L-W power model. Fusion power was the second term in the power balance model. This term related the number density of the fuel sources to the cross-sectional area of the reaction and the energy produced [41].

$$\left(\frac{du}{dt}\right)_{fus} = \eta n_D n_T \overline{\sigma v} E_\alpha / \rho \tag{3-6}$$

Fusion power is a function of the number density of the fuel terms n_D and n_T, the cross-section of the fusion reaction $\overline{\sigma v}$, and the energy of an alpha particle at the creation of a DT reaction (3.5 MeV). The fusion power equation in 3-6 is augmented to include two additional terms. The first term, η represents the fraction of energy deposition into the plasma. The second term is the mass density, the fusion power equation is a function of per volume and by dividing by density makes it a function of per mass, which is required in the SPH equations. The SPH formulation use a per mass basis. The fractional deposition is a function of the target parameters, given by [6]

$$\eta = \frac{x_\alpha + x_\alpha^2}{1 + \frac{13 x_\alpha}{9} + x_\alpha^2} \tag{3-7}$$

the η parameter assumed a value between zero and one, with one being complete deposition. The parameter x_a is the independent variable inside the curve fit shown by Equation 3-7. The value of x_a was calculated in the equation below

$$x_\alpha = \frac{8}{3}\left(\bar{R} + \frac{b^2}{\sqrt{9b^2 + 1000}}\right) \quad 3\text{-}8$$

where the parameter $\bar{R}$ was defined by

$$\bar{R} = \frac{R}{l_\alpha}. \quad 3\text{-}9$$

This equation related the target radius R and the collision path l_α of an alpha particle. By doing this a non-dimensional straight line path of an alpha particle through the target is formed. This path provides a means of representing the straight line distance the alpha particle traveled and deposited energy. The b parameter is

$$b = \frac{R}{r_{\alpha L}}. \quad 3\text{-}10$$

The $r_{\alpha L}$ parameter is the Larmor radius of the alpha particle at its creation. The Larmor radius is the "orbit" that the alpha particle moves about the magnetic field lines. The b term is a way of representing the curved path; the alpha particle travels through the magnetized target. The parameter l_α is estimated to be

$$l_\alpha = \frac{v_{\alpha 0}}{\nu_\alpha} \quad 3\text{-}11$$

where ν_α is the collision frequency, $v_{\alpha 0}$ is the velocity of the alpha particle at creation. In our problem the initial target radius was used for the deposition and remained relatively constant for the simulation and was not tracked in time. Equation 3-8 formed a non-dimensional path of the alpha particle as it traveled through the target. It accounted for the magnetic field of the target, and when the field strength is zero collapsed to a

straight-line path that the alpha particle would take through the plasma. Equation 3-8 provided a model of how the particle traveled and deposited its energy. This deposition model adjusted the total energy change of an SPH particle that modeled the fusion reactions as the source of heating inside the target and liner at each time step. Analysis of the deposition model found that it was unity for the parameter choices in this study. This was applied to local deposition based on the local SPH particle, which is consistent with earlier work by Kirkpatrick and Knapp [10].

The radiation lost to Bremsstrahlung radiation is the first loss term [29] [16] [9] [17],

$$\left(\frac{du}{dt}\right)_{rad} = -\frac{64\pi^2 e^6}{3\sqrt{6\pi}} \frac{1}{m_e c^2 \hbar (4\pi \mathcal{E}_o)} \sqrt{\frac{kT_e}{m_e c^2}} \frac{Z_i^3 \rho^3}{(MW m_a)^2}. \qquad 3\text{-}12$$

Equation 3-12 uses temperature in units of electron volt (eV), where 1 eV is 11605 K. The e term is the elementary charge value. The $\mathcal{E}_o$ is the permittivity of free space, c is the speed of light in a vacuum, $\hbar$ is the Planck constant, MW is the molecular weight, m_a is the mass of the ion species, Z_i is the charge value, and m_e is the electron mass. Bremsstrahlung radiation was treated as a loss term, and this analysis did not attempt calculation of its re-absorption into the plasma. This was an intentionally conservative approach, and remains consistent with the way radiation was modeled inside the original L-W models. Calculation of the Bremsstrahlung radiation at 10 keV shows the peak spectrum of photon energy is at 4 keV, and rapidly falls off away from the peak. The optical depth of the plasma is longer than the particle size, thus radiation absorption is a nonlocal phenomenon. While absorption would have a role in maintaining target plasma

temperature, it was decided to neglect absorption to remain conservative in fusion gain estimation.

Thermal conduction is given by

$$\left(\frac{du}{dt}\right)_{cnd} = \frac{1}{\rho}\nabla \cdot k_{\perp}\nabla T \qquad 3\text{-}13$$

Equation 3-13 represents the heat transfer due to thermal conduction away from the target. The coefficient of thermal conductivity is given by $k_{\perp}$, where the perpendicular subscript refers to the direction of conduction based on the Braginskii model [42]. Braginskii showed that there were different rates of conduction when a magnetic field is incorporated into the thermal conduction. This analysis was concerned with an axial field in a cylindrical target. In three-dimensions the thermal conduction has three components, however in this analysis the magnetic field is in the z direction and the properties are axisymmetric about the z-axis, leaving only the perpendicular conduction to be the source of a temperature gradient. The liner compressed the target perpendicular to the field direction; because of this we limited our thermal conduction to be only in the perpendicular direction. The thermal conductivity is calculated using the equation below [42] [43], given by

$$\mathrm{k}_{\perp}^{\mathrm{e}} = \frac{4.7\mathrm{nkT}}{\mathrm{m_e}\omega_{\mathrm{ce}}^2\tau_{\mathrm{e}}} \qquad 3\text{-}14$$

Equation 3-14 is a function of the temperature of the plasma, its number density, the mass of an electron, the collison rate of an electron, and gyrofrequency. Gyrofrequency is determined by the local field strength. Kirkpatrick and Lindemuth's addition of a magnetic field was critical to lowering the minimum aerial density necessary for ignition. The expression fo the electron collsion frequency is

$$\omega_{ce} = \frac{qB}{m_e}. \tag{3-15}$$

Electrons were the primary heat transfer mechanics for conduction. The electron collision frequency is significantly higher than ions. This higher rate means that electrons collide and transfer energy more often than ions and they act as the conduit if energy transfer. The collisonality is a function of particle number density, temperature, and the coulomb logarithm.

$$\tau_e = 3.44 \times 10^5 \frac{T_e^{\frac{3}{2}}}{n\lambda} \tag{3-16}$$

The Coulomb logarithm for this analysis was taken to be 10, which is an average value across many orders of magnitude range in temperature and density. Since the full properties of a test a problem are uncertain, an exact value of the coulomb logarithm was unnecessary. Chen [27] and the NRL plasma formulary [28], both estimate that λ may take on any value ranging from 5-20. The influence into the conductivity was minor, and typical values of thermal conductivity for this analysis are on the order of $10^8 W/m$. The impact of using a fixed Coulomb logarithm was minimal, as the heat transfer rate is high, and the logarithm is between 5 and 20 causing only minor changes to the magnitude of the heat transfer coefficient.

3.3 Smoothed Particle Hydrodynamics

The above equations were cast into the smooth particle hydrodynamic (SPH) form. The SPH form was conceived in the 1970s by Gingold and Monaghan [44] [45] [39], and separately by Lucy [46] at about the same time. The method arose from the need for a fast, efficient, 3-D model for astrodynamics modeling [45]. Since its inception, SPH has gained popularity in a diverse set of fields ranging from astrophysics and engineering to

computer graphics and fluid modeling for games [47] [48] [49]. Its methodology is to discretize the differential equations by replacing the integrations with weighted summations over a local neighborhood of particles [45] [39] [50]. The discrete summations model the differential equations at each time evolution and particle positions and velocities updated.

3.3.1 Function Approximation by a Weighting function

Before the MHD and power balance terms are implemented into SPH form, we present the background SPH formalism for function approximation. A function was approximated by its kernel representation [45] [51] [52] [53]. Equation 3-17 represents a function locally approximated by an integral,

$$f(x) = \int_{\Omega} f(x')\delta(x - x')dx'. \tag{3-17}$$

where $\delta(x - x')$ is the delta Dirac Delta function, taking the form given by equation 3-18,

$$\delta(x - x') = \begin{cases} 1, x = x' \\ 0\ x \neq x' \end{cases}, \tag{3-18}$$

The Ω term represented the volume of the integral that contains x. The Delta function is only a point representation of the function and not able to represent the function for a discrete set of particles [49]. To remedy this situation the Delta function is replaced with a smooth continuous function with finite spatial dimension [54] [55],

$$\langle f(x) \rangle = \int_{\Omega} f(x')W(x - x', h)dx'. \tag{3-19}$$

Equation 3-19 replaces the Dirac function with a smooth weighting function

$W(x - x', h)$ of compact support over a distance of h. The parameter h represents the region of space where the smoothing kernel will operate on particles. There are several properties that the smoothing kernel must have. First,

$$\int_{\Omega} W(x - x', h)dx' = 1, \tag{3-20}$$

and the integration of W over the domain must equal one to ensure that the summation does not under or overweight the particle neighborhood [45]. This condition is referred to as the *normalization condition*. The second property, known as the *Delta function property* requires that the function must approach the Delta function in the limit of the smoothing length $h \to 0$, shown in equation 3-21,

$$\lim_{h \to 0} W(x - x', h) = \delta(x - x'). \tag{3-21}$$

The third property, is the *compact condition* [55] [52]. This requirement ensured that the kernel approximation of W was only valid within its local region shown below,

$$W(x - x', h) = 0 \text{ when } |x - x'| > \kappa h, \tag{3-22}$$

where κ represents the cutoff value of h, typically κ has a value from two to three and κ is determined by the choice of kernel function [56]. The above approximations were useful for reconstructing a function from loose, scattered points, however, to reconstruct derivatives an additional property is needed. The spatial derivative were approximated through a similar fashion [50] [45] [39] [57],

$$\langle \vec{\nabla} f(x) \rangle = \int_{\Omega} f(x') \vec{\nabla} W(x - x', h)dx'. \tag{3-23}$$

This requires and additional property of the smoothing function where the gradient of the smoothing function must become zero, represented in Equation 3-24,

$$\int_{\Omega} \vec{\nabla} W(x - x', h) dx' = 0. \qquad 3\text{-}24$$

This ensures that the derivatives will not have a preference in spatial direction even if the points are scattered unevenly [52].

3.3.2 Particle Interpolation

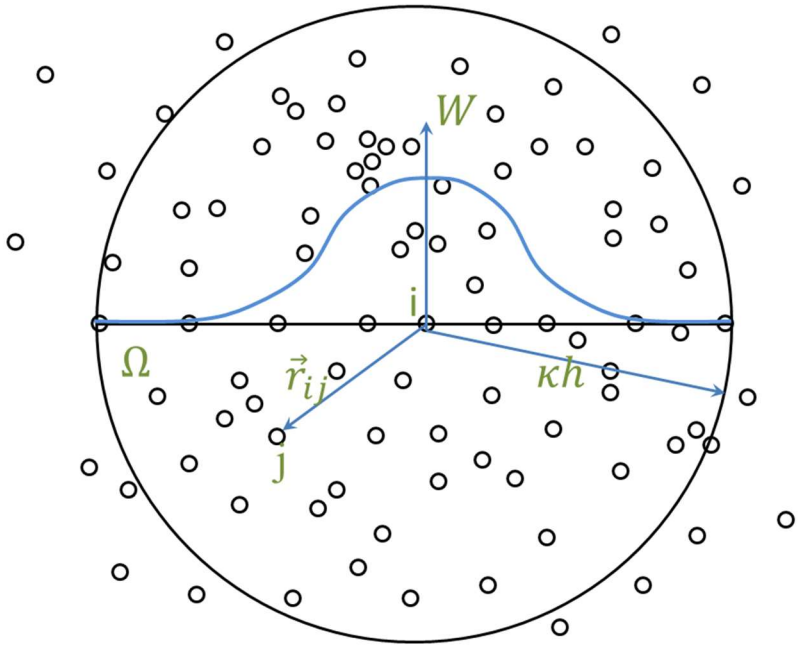

Figure 3-1: Particle value approximation by summation over weighted particle values. r_{ij} represents the distance of particle i to particle j. The support of the domain is over Ω. The compact support radius is shown by κh.

The prior discussion only approximated the value of a function by a kernel approximation. The next step was to apply this to a set of scattered points. Figure 3-1 and

Figure 3-2 illustrate how scattered point *i* was interpolated to by all of the points inside its neighborhood. Each particle had a discrete element that carries with it fluid properties such as temperature, pressure, density, etc. Equation 3-19 represented a continuous system and cannot be applied over the domain made up of discrete particles and their neighborhoods. The condition of equation 3-19 was relaxed to a weighted summation,

$$\langle f(x)\rangle = \sum_{j=1}^{N} \frac{m_j}{\rho_j} f(x_j) W(x - x_j, h_i) \tag{3-25}$$

where the parameter *N i*s the number of particles within the neighborhood of position *x*. The same process is used to calculate the derivative,

$$\langle \vec{\nabla} f(x)\rangle = \sum_{j=1}^{N} \frac{m_j}{\rho_j} f(x_j) \vec{\nabla} W(x - x_j, h_i) \tag{3-26}$$

the m_j/ρ_j term takes the place of volume within the integral [49]. The volume calculation is not limited to the m_j/ρ_j term. Several other methods for calculation of the volume were provided by references [58] [59] [60] [61] [62]. Additional ways of improving the calculation of the derivative had been put forth by Rosswog [52] and Garcia-Senz [51]. They used a matrix form of the derivative that was higher-order in space than presented in equation 3-26; however, the method was subject to singularity constraints of the matrix inversion. If the matrix becomes singular, which occurs if particles co-align in space, which is possible in expansion problems, then this process fails [51] [52]. To provide representation of a particle value at a given particle position equations 3-25 and 3-26 are updated to replace *x* with x_i,

$$\langle f(x_i)\rangle = \sum_{j=1}^{N} \frac{m_j}{\rho_j} f(x_j) W(x_i - x_j, h_i), \tag{3-27}$$

and

$$\langle \vec{\nabla} f(x_i) \rangle = \sum_{j=1}^{N} \frac{m_j}{\rho_j} f(x_j) \vec{\nabla} W(x_i - x_j, h_i). \qquad 3\text{-}28$$

Now, the equations represent the estimation through spline interpolation of a particles properties by weighted summation over a particles set of neighbors.

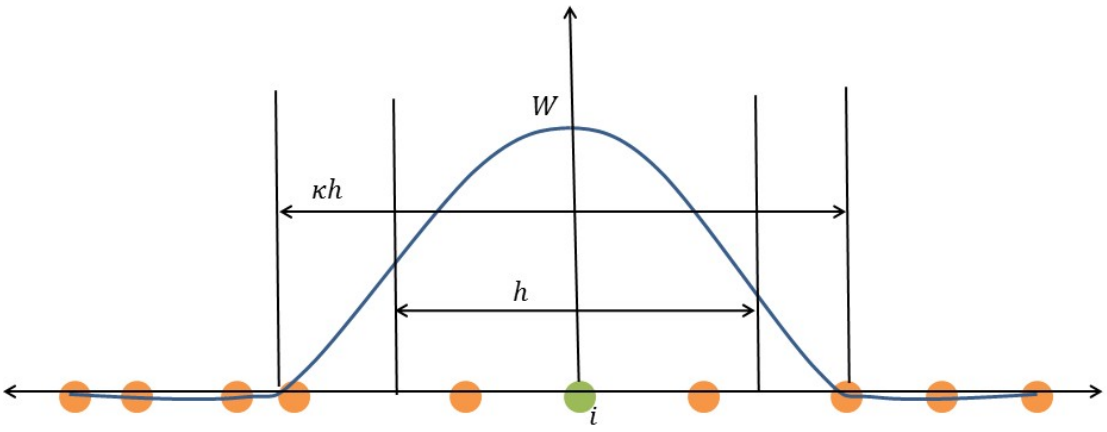

Figure 3-2: A weighting function such as a cubic B-spline or Gaussian function evaluated over the support domain of particle *i*. The smoothing distance *h* was the support width of the weighting function. The cutoff of the weighting function was by value κ, which represented the compact support domain of a smoothing kernel.

The choice of weighting function is varied and often dependent on the problem being solved. For this work a Wendland spline was used due to its property of being insensitive to the particle clumping phenomena [56] [52]. Equations 3-29 represent the weighting function in 1-D and 2-D respectively [56] [63],

$$W = \frac{5}{4}(1-q)^3(1+3q) \qquad \text{for 1--D } if\ q \le \kappa h\ else\ 0$$
$$W = \frac{7}{\pi}(1-q)^4(1+4q) \qquad \text{for 2-D } if \le \kappa h\ else\ 0 \qquad 3\text{-}29$$

The q term in the equation scales the position difference between particle i and j. This scaled value $q = r/\kappa h$, allows the function to be generic and scales the equation out to the cutoff distance κh. All functions followed a similar approach to compact support as equations 3-29. Desirable properties in a candidate function are [39]:

1. A weight that is positive and smoothly decreases with distance
2. The function is symmetric about the direction of drop-off
3. A relatively level region close to the central point to avoid drastic impacts by nearest neighbors.

Figure 3-3 shows the cubic spline and its derivative over a smoothing length. The cubic spline smoothly drops off and has a flat region that is desirable given property 1 above. The derivative was smooth and had a value of zero at the origin of the function. This allowed the spline to approximate the derivative of a function over the influence of the neighbor particles. Other candidate functions are the Gaussian:

$$W = \frac{\sigma}{h^{\nu}} e^{-\frac{(r_i - r_j)^2}{h^2}}, \tag{3-30}$$

which does not have a direct cutoff distance; instead it is terminated at $3h$ under usual circumstances. The most commonly used function, was the cubic B-spline [45],

$$W = \frac{\sigma}{h^{\nu}} \begin{cases} \frac{1}{4}(2-q)^3 - (1-q)^q, & 0 \le q < 1 \\ \frac{1}{4}(2-q)^3, & 0 \le q < 1' \\ 0, & q \ge 2 \end{cases} \tag{3-31}$$

where ν represents the spatial dimension and σ is a normalization factor $\sigma = \frac{2}{3}, \frac{10}{7\pi}, 1/\pi$.

The smoothing parameter h was an important consideration in the calculation of the weighting function. The h parameter controlled the smooth drop-off of the kernel and

its derivatives by affecting the width of the smoothing function. Unfortunately, it was often taken as a free parameter and its choice being decided by a user [39]. The smoothing parameter was tied to the local shape of the particles around the particle of interest *i*. The common method for determining the smoothing parameter was by iteration. The smoothing parameter was a function of the spline summation, shown in Equation 3-32 [45] [54] [50] [52] [39],

$$h(r) \propto \left(\sum_j W\left(r - r_j, h(r)\right) \right)^{-\frac{1}{\nu}}. \qquad 3\text{-}32$$

Equation 3-32 related the smoothing parameter to the inverse of the local smoothing function.

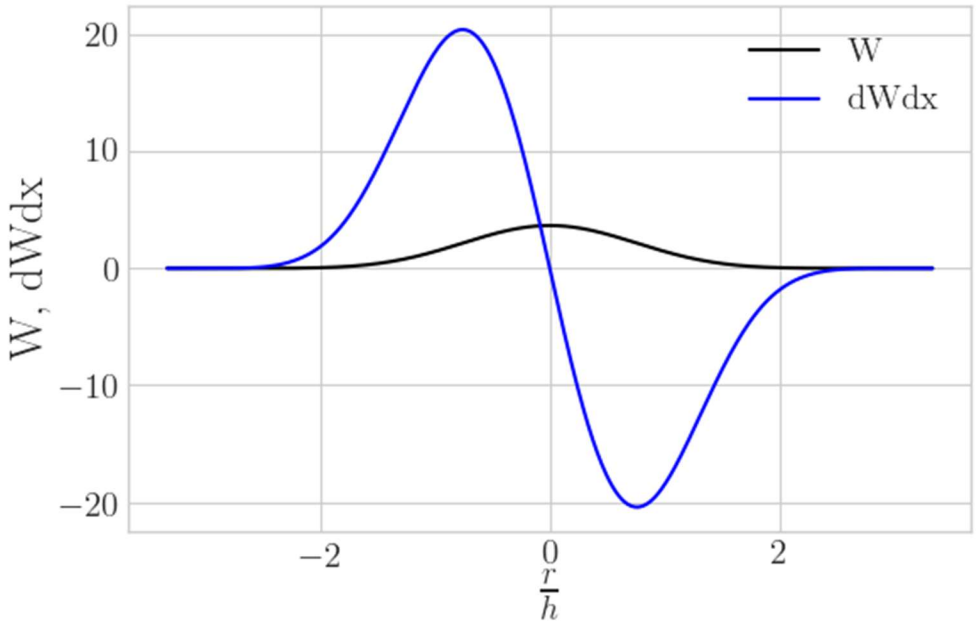

Figure 3-3: A typical spline function and its derivative evaluated over $3h$ spacing. The blue curve represents the spline value; its peak is at the center and smoothly drops off.

The derivative is a smooth value as well, its evaluation is zero at the center where the particle of interest would reside. This allows summations to be smoothly behaved.

A typical method in SPH is to calculate density by a summation of the local particle masses,

$$\rho_i = \sum_{i=1}^{N} m_j W(r_{ij}, h_i). \tag{3-33}$$

This provides a convenient feedback loop between density calculated in equation 3-33 and equation 3-32. Monaghan [45] suggested that the smoothing function be calculated as a function of particle mass and density,

$$h_i = \eta \left(\frac{m_i}{\rho_i}\right)^{\frac{1}{\nu}}, \tag{3-34}$$

where equation 3-34 relats h to the mass and density of its local particle i. The factor η is a constant of proportionality suggested by Price and Monaghan, and is determined based on the smoothing function. In this work for two-dimensions, η was set to 1.3. Springle and Hernquist [64] suggested an iterative method between equations 3-32 and 3-34 to calculate a self-consistent smoothing parameter. The process was as follows:

1. Guess a value for the smoothing parameter
2. Calculate the particle volume as $V = 1/\sum_j^N W(r_{ij}, h)$, where all neighbors that fall inside κh are used.
3. Relate that volume back to the mass volume of a particle by $V_i = m_i/\rho_i$ being substituted into equation 3-34 for the term in parenthesis
4. Recalculate volume $V = 1/\sum_j^N W(r_{ij}, h)$. Repeat steps until the value of h converges to some specified tolerance ~10^{-6}.

The typical number of iterations once h was suitably solved for is usually 5-10. This was a fast calculation that does not bottleneck the program. By doing this process the value of smoothing parameter was coupled with the mass, density, and volume of a particle. This led to the question of what a particle's mass should be? Price and Rosswog [65] [39] suggested that the particle mass remain constant for a problem. This effectively sets the resolution of the simulation to the particle mass. A fixed mass then fixed the spacing of particles through equation 3-34. Price and Rosswog then suggested that the mass and smoothing parameter be related by

$$m_i = h_i \, {}^{\nu}\rho_i = constant, \tag{3-35}$$

where equation 3-35 relates the density, a parameter that is usually known upon instantiation of a problem, mass an unknown but chosen parameter, and smoothing length which relates back through the iterative method outlined above. This tied the SPH methods smoothing length, mass, and density together into a consistent system.

3.3.3 Smooth Particle Magnetohydrodynamics

The prior discussion provided a backdrop and mathematical frame work to build the equations of motion. There are several methods for developing the equations of motion, the standard method was to start with the Lagrangian variational approach as suggested by Hernquist and Katz [66] and applied by Price and Monaghan [67].

The Lagrangian was simply the differences between the potential and kinetic energies:

$$L = T - V, \tag{3-36}$$

where, T is the kinetic energy and V is the potential energy. In MHD form the equation becomes [39]:

$$L = \sum_{j}^{N} m_j \left[\frac{1}{2} v_j^2 - u_j(\rho_j, s_j) - \frac{1}{2\mu_o} \frac{B_j^2}{\rho_j} \right]. \quad 3\text{-}37$$

The first term on the right side is the kinetic energy, the second is the internal energy and the final term was the magnetic field energy. The summation is performed over the local neighborhood of a particle. The discrete system shown in Equation 3-37 is derived by Morrison in reference [68]. The internal energy is a function of density and entropy while the kinetic energy was dependent on velocity of a particle. Following Price's derivation, the principle of least action is used to constrain the change on the Lagrangian,

$$\delta S = \int \delta L dt = 0. \quad 3\text{-}38$$

Equation 3-38 then assumes the Lagrangian to be written as a differentiable function of the particle positions and velocities [39]. Equation 3-38 can be written in terms of the differentiable function,

$$\delta S = \int \left(\frac{\partial L}{\partial \vec{v}} \cdot \delta \vec{v} + \frac{\partial L}{\partial \vec{r}} \cdot \delta r \right) dt = 0. \quad 3\text{-}39$$

This can be generically integrated using integration by parts and the following relation [39]: and

$$\delta \vec{v} = d(\vec{r})/dt, \quad 3\text{-}40$$

and,

$$d/dt = \partial/\partial t + \vec{v} \cdot \vec{\nabla}, \quad 3\text{-}41$$

which represented the total derivative. The final evaluation of the path difference δS is given by:

$$\delta S = \int \left\{ \left[-\frac{d}{dt}\left(\frac{\partial L}{\partial \vec{v}}\right) + \frac{\partial L}{\partial \vec{r}} \right] \cdot \overrightarrow{\delta r} \right\} dt + \left[\frac{\partial L}{\partial \vec{v}} \cdot \delta r \right]_{t_o}^{t} = 0. \quad 3\text{-}42$$

The first term in brackets was the Euler-Lagrange equation [69]. This term by its definition equals zero [70]. The partial derivatives of the Lagrangian was evaluated to

$$\frac{\partial L}{\partial \vec{v}} = m\vec{v}, \;\; \frac{\partial L}{\partial \vec{r}} = -m \frac{\partial u}{\partial \rho} \Big|_s \frac{\partial \rho}{\partial \vec{r}}. \quad 3\text{-}43$$

This assumption then allowed a small perturbation of the Lagrangian to be written as:

$$\delta L = m_i \vec{v}_i \cdot \delta \vec{v}_i - \sum_j^N m_j \left[\frac{\partial u}{\partial \rho_j} \Big|_s \delta \rho_j + \frac{1}{2\mu_o} \left(\frac{B_j}{\rho_j}\right)^2 \delta \rho_j + \frac{1}{\mu_o} \vec{B}_j \cdot \delta \left(\frac{\vec{B}_j}{\rho_j}\right) \right] \quad 3\text{-}44$$

where the perturbation is considered small in respect to the particle state. The change in energy used a constant entropy formulation, consistent with Price [39]. The change in internal energy is related to the pressure through:

$$\frac{\partial u}{\partial \rho} \Big|_s = \frac{P}{\rho^2}, \quad 3\text{-}45$$

where the relation was given by Price [39] and Rosswog [52]. Making substitutions into Equation 3-38

$$\delta S = \int \left\{ m_i \vec{v}_i \cdot \delta \vec{v}_i - \sum_j^N m_j \left[\frac{\partial u}{\partial \rho_j} \Big|_s \delta \rho_j + \frac{1}{2\mu_o} \left(\frac{B_j}{\rho_j}\right)^2 \delta \rho_j + \frac{1}{\mu_o} \vec{B}_j \cdot \delta \left(\frac{\vec{B}_j}{\rho_j}\right) \right] \right\} \mathrm{dt} = 0. \quad 3\text{-}46$$

Following the simplifications given by Price and Rosswog [39] [52], the momentum equations becomes

$$\frac{d\vec{v}_i}{dt} = -\sum_j^N m_j \left[\frac{\left(P_i+\frac{1}{2\mu_o}B^2\right)}{\Omega_i\rho_i^2}\vec{\nabla}W(h_i) + \frac{\left(P_j+\frac{1}{2\mu_o}B^2\right)}{\Omega_j\rho_j^2}\vec{\nabla}W(h_j)\right] + \frac{1}{u_o}\sum_j^N m_j \left[\frac{\vec{B}_i\left(\vec{B}_i\cdot\vec{\nabla}W(h_i)\right)}{\Omega_i\rho_i^2} + \frac{\vec{B}_j\left(\vec{B}_j\cdot\vec{\nabla}W(h_j)\right)}{\Omega_j\rho_j^2}\right]. \quad 3\text{-}47$$

The factor Ω to account for smoothing length change during time evolution has been incorporated into the derivatives [39]. The Ω scales the derivative summation depending to how the particles change position which in turn impacts density, and the local neighborhood to change the smoothing parameter. This term was calculated in accordance with Price's formulation [39]

$$\Omega_i = 1 - \frac{\partial h}{\partial \rho}\sum_j^N m_j \frac{\partial W(h_i)}{\partial h_i}. \quad 3\text{-}48$$

The derivative of h with respect to ρ is calculated using Equation 3-34,

$$\frac{\partial h}{\partial \rho} = -\frac{h}{\rho\nu}, \quad 3\text{-}49$$

where the term ν is the spatial dimension of the problem 1,2, or 3. Simplification of the continuity equation is performed by using a weighted summation of the masses of the particles multiplied by the weighting function of the smoothing kernel [45]. Equation 3-33 provides the density estimate used in this SPH simulation, it had the desirable properties that other formulations do not have, namely that it will always maintain a physical, positive value of density [45]. This allowed the code to remain "intact" when odd things happen in momentum or energy [45]. Use of a time-dependent continuity equation makes it possible for density to drop below zero, which is unphysical; use of the

mass summation prevents this occurrence [45]. The energy equation came directly from the hydrodynamic energy equation, presented by Price [39].

$$\frac{du_i}{dt} = \frac{P_i}{\rho_i^2}\sum_j^N m_j\left(\vec{v}_i - \vec{v}_j\right)\cdot\vec{\nabla}W(h_i). \tag{3-50}$$

The final equation needed to complete the ideal MHD equations in SPH form was the induction equation, given by Equation 3-4. In SPH form used the formulation provided by Vanaverbeke [40],

$$\frac{d\overrightarrow{B_i}}{dt} = \frac{1}{\rho_i}\sum_j^N m_j\left(\vec{B}_i\vec{v}_{ij} - \vec{v}_{ij}\vec{B}_i\right)\cdot\vec{\nabla}W_{ij}(h_i). \tag{3-51}$$

While Equations 3-47, 3-33, 3-50, and 3-51 represent a complete SPH formalism of the ideal MHD equations, there are several augmentations that need to be added. These are artificial terms that provide stability to the equations while solving strong discontinuities in the pressure, or magnetic fields. The equations below are the SPH equations with artificial terms,

$$\rho_i = \sum_{i=1}^N m_j W(r_{ij}, h_i), \tag{3-52}$$

$$\frac{d\vec{v}_i}{dt} = -\sum_j^N m_j\left[\frac{\mathcal{M}_i}{\Omega_i\rho_i^2}\vec{\nabla}W(h_i) + \frac{\mathcal{M}_j}{\Omega_j\rho_j^2}\vec{\nabla}W\left(h_j\right)\right] + \left(\frac{dv_i}{dt}\right)_{dis} + \left(\frac{dv_i}{dt}\right)_{Borve}, \tag{3-53}$$

$$\frac{du_i}{dt} = \frac{P_i}{\rho_i^2}\sum_j^N m_j\left(\vec{v}_i - \vec{v}_j\right)\cdot\vec{\nabla}W(h_i) + \left(\frac{du_i}{dt}\right)_{dis} + \left(\frac{du_i}{dt}\right)_{res}, \tag{3-54}$$

$$\frac{d\vec{B}_i}{dt} = \frac{1}{\rho_i}\sum_j^N m_j\left(\vec{B}_i\vec{v}_{ij} - \vec{v}_{ij}\vec{B}_i\right)\cdot\vec{\nabla}W_{ij}(h_i) + \left(\frac{d\vec{B}_i}{dt}\right)_{res}. \tag{3-55}$$

Several methods for handling discontinuities had been explored in the SPH formalism. The common method, and the one used in this analysis was to have stabilizing artificial terms in the momentum, energy, and induction equations. However, Imaeda and Inutsuka suggested corrections to the standard formulism to control density errors by changing the density formulation [71]. This would help control density inconsistency in shear flows and shocks. Another alternative was to use Godunov methods to solve particle discontinuities in shocks, this was proposed by Cha and Whitworh [72], Monaghan also experimented with Riemann type solvers in reference [73] as did Inutsuka in reference [74]. For this analysis it was decided to remain with well-known methods demonstrated in other MHD SPH formalisms. The use of artificial terms and MHD formalism in SPH had been looked at by several groups. Monaghan looked at resolving the tensile instability that can appear in MHD formalisms when the pressure gradient becomes negative [75]. Borve, Omang, and Trulsen formulated a version of the MHD equations in SPH, using a more traditional momentum and energy equation [76] [77]. Borve presented a way of correcting for the divergence of magnetic field that can crop up when numerical noise pollutes the derivatives [77],

$$\left(\frac{d\vec{v}}{dt}\right)_{Borve} = -\hat{\beta}\sum_{j}^{N} m_j B_i^k \left[\frac{B_i^l}{\Omega_i \rho_i^2}\nabla^{\mathrm{l}} W(h_i) + \frac{B_j^l}{\Omega_j \rho_j^2}\nabla^{\mathrm{l}} W\left(h_j\right)\right]. \qquad 3\text{-}56$$

Equation 3-56 simply subtracts off the unphysical accumulation of magnetic field due to the numerical errors. The $\hat{\beta}$ term was a constant determined by reference [40] and ranged from one to two. To control the other errors the artificial terms become:

$$\left(\frac{d\vec{v}_i}{dt}\right)_{dis} = \sum_j^N \frac{m_j\left(\alpha v_{sig}\vec{v}_{ij}\cdot\hat{r}_{ij}\right)}{\bar{\rho}_{ij}}\vec{\nabla}\bar{W}_{ij}(h_i). \quad 3\text{-}57$$

Equation 3-57 controls the artificial viscosity in the momentum equation. The α term was a switching term consistent with Dehen and Cullen's [78] switching term which was similar to Price's [39] without the tensor formulation. The term v_{sig} is the signal velocity. In the momentum equation $v_{sig} = a = \sqrt{\gamma\bar{R}T}$, which is the sound speed in the gas. Both Sigallotti [54] and Price [39] recommend a thermal conduction term to help mitigate the pressure blip that's caused at contact discontinuities,

$$\left(\frac{du_i}{dt}\right)_{dis} = \sum_j^N \frac{\alpha m_j\left(u_i - u_{bj}\right)}{\bar{\rho}_{ij}}\hat{r}_{ij}\cdot\vec{\nabla}\bar{W}(h_i), \quad 3\text{-}58$$

where, the same α was used in the viscosity equation. The MHD equations required a control on thermal energy due to evolution of the magnetic field. This was similar to Price [39] and Vanaverbeke [40],

$$\left(\frac{du_i}{dt}\right)_{res} = -\rho_i\sum_j^N \frac{m_j v_{sig}^B\alpha}{4\rho_{ij}^2}\left(\vec{B}_i - \vec{B}_i\right)^2\hat{r}_{ij}\cdot\vec{\nabla}\bar{W}(h_i). \quad 3\text{-}59$$

Equation 3-59 represents the magnetic field turned into thermal energy. The v_{sig}^B term was the Alfven velocity given by

$$v_{si}^B{}_i = \frac{1}{\sqrt{2}}\sqrt{a_i^2 + \frac{B_i^2}{\mu_o\rho_i} + \sqrt{\left(a_i^2 + \frac{B^2}{\mu_o\rho_i}\right)^2 - 4\,\frac{a_i^2\left(B_i\cdot\hat{r}_{ij}\right)^2}{\mu_o\rho_i}}}, \quad 3\text{-}60$$

where $\hat{r}_{ij}$ is the unit vector pointing along the direction $\vec{r}_{ij} = \vec{r}_i - \vec{r}_j$. The final artificial term is the resistivity term, to control magnetic field evolution,

$$\left(\frac{d\vec{B}_i}{dt}\right)_{res} = \rho_i \sum_j^N m_j \frac{v_{sig}^B}{2\rho_{ij}^2}\left(\vec{B}_i - \vec{B}_j\right)\hat{r}_{ij} \cdot \vec{\nabla}\overline{W}(h_i). \quad 3\text{-}61$$

The smoothing parameter correction term was not included in these terms. Instead the average of the particle *i* and particle *j* smoothing function are used to calculate an artificial term that was symmetric to both particles. This represents the complete SPH method used in the MHD modeling of the analysis.

It has been hypothesized that SPH formulated in a Lagrangian format is not capable of handling discontinuities [79]. The Lagrangian formulation and Equation 3-45, which uses a constant entropy assumption, explicitly cannot handle a discontinuity, such as a shock wave. The nature of the particle formulation assumes that all particles are discrete. This discrete nature causes the other issue with discontinuity capture. However, to remedy this situation and restore discontinuity capture, artificial terms presented above are added to the equation of motion [79]. To demonstrate SPH's capabilities in hyperbolic problems, we present both a standard Sod shock tube and the Brio and Wu shock tube. These test the hyperbolic form of the Euler equations and the ideal MHD equations.

3.4 Thermal Conduction in SPH

The final model used in the analysis that must be cast into SPH from is Equation 3-13, which represents the cross-field electron thermal conduction to or away from the plasma. Modeling of this method was consistent with SPH methods but the need for a second order derivative added some complexity to the SPH method. For this research the thermal conduction was modeled based on the work of Monaghan [80] and employed by Jubelgas et al. in reference [81] for cosmological simulations. The form of the thermal conduction in SPH becomes

$$\frac{du_i}{dt} = \sum_j^N \frac{m_j}{\rho_i \rho_j} \frac{\kappa_{\perp i} + \kappa_{\perp j}}{2} \left(T_j - T_i\right) \frac{\vec{r}_{ij}}{r_{ij}^2} \cdot \vec{\nabla} W(h_i), \tag{3-62}$$

where T_i is the temperature of the i^{th} particle. The second derivative is approximated as the first derivative divided by the radial distance, thus a pseudo second order derivative is defined. The complete SPH methodology model with augmented power terms is presented below. These are the complete equations used in this study,

$$\rho_i = \sum_{i=1}^N m_j W(r_{ij}, h_i), \tag{3-63}$$

$$\frac{d\vec{v}_i}{dt} = -\sum_j^N m_j \left[\frac{\mathcal{M}_i}{\Omega_i \rho_i^2} \vec{\nabla} W(h_i) + \frac{\mathcal{M}_j}{\Omega_j \rho_j^2} \vec{\nabla} W(h_j)\right] + \left(\frac{dv_i}{dt}\right)_{dis} + \left(\frac{dv_i}{dt}\right)_{Borve}, \tag{3-64}$$

$$\begin{aligned} \frac{du_i}{dt} = {} & \frac{P_i}{\rho_i^2} \sum_j^N m_j \left(\vec{v}_i - \vec{v}_j\right) \cdot \vec{\nabla} W(h_i) + \left(\frac{du_i}{dt}\right)_{dis} + \left(\frac{du_i}{dt}\right)_{res} + \left(\frac{du_i}{dt}\right)_{fus} \\ & - \left(\frac{du_i}{dt}\right)_{rad} - \left(\frac{du_i}{dt}\right)_{cnd} \\ & + \sum_j^N \frac{m_j}{\rho_i \rho_j} \frac{\kappa_{\perp i} + \kappa_{\perp j}}{2} \left(T_j - T_i\right) \frac{\vec{r}_{ij}}{r_{ij}^2} \cdot \vec{\nabla} W(h_i), \end{aligned} \tag{3-65}$$

$$\frac{d\vec{B}_i}{dt} = \frac{1}{\rho_i} \sum_j^N m_j \left(\vec{B}_i \vec{v}_{ij} - \vec{v}_{ij} \vec{B}_i\right) \cdot \vec{\nabla} W_{ij}(h_i) + \left(\frac{d\vec{B}_i}{dt}\right)_{res}. \tag{3-66}$$

3.5 Test Cases

To ensure accuracy of the models and their capabilities, several test cases have been performed. The following test cases provide a myriad of physics to test a methodology's correctness: Sod shock tube, Noh Infinite Shock, Kelvin-Helmholtz Instability, Hydrodynamic merger of plasma jets, Brio and Wu MHD shock tube, fusion power

balance equation, Thermal Conduction, and Bremsstrahlung radiation. These cases were chosen based on the physics they emulate or being a standardized test for any code that wants to replicate that type of physics.

3.5.1 Verification Procedure

To verify that the program was working correctly the test cases above are run and calculated back to either analytical results or experimental outcomes. In some cases there is no analytical result to compare against so the accepted numerical solution is used. The target goal was to be within 10% error of the accepted values. Both one-dimensional cases and two-dimensional cases were run to test the importance of dimensionality.

3.5.2 Sod Shock Tube

The Sod shock tube was the defining test of capturing a normal shock between two gases. The origin of this test case comes from reference [82], where the need to compare different implementations of finite difference solvers were compared. Sod's shock tube had an analytical solution, which makes it convenient to compare against and ensure accuracy.

Table 3-1: Sod shock tube setup.

Property	Left	Right
Density kg/m^3	1.0	0.25
Pressure Pa	1.0	0.1795

Problem setup had two gases separated by a diaphragm placed in the middle of a long tube. The left side of the diaphragm has a higher pressure, higher density gas. The right side has a low density, low pressure gas. The diaphragm was burst at time zero. This causes the high pressure gas to collide with the low pressure gas and immediately sets up

a normal shock that begins to run to the right. For this analysis, 5000 equal mass particles were placed along the axis of the shock tube. The particles being equal mass were spaced according to Equation 3-34, spacing each particle by its smoothing parameter. This causes the left side to have more particles than the right side to ensure the density was properly calculated. In this way, it's adapting the particle spacing to the SPH interpolation estimate [54].

Table 3-1 shows the left and right setup of the shock tube. The specific heats are constant across the problem, and a constant specific gas constant of 287 J/K was used on both sides. The equation of state used was the ideal gas law $P = \rho RT$, and this specifies the temperature and internal energy of the system. While some authors do recommend smoothing of the contact discontinuity to provide some relief to the numerical approximation [54], no smoothing of the contact discontinuity was performed.

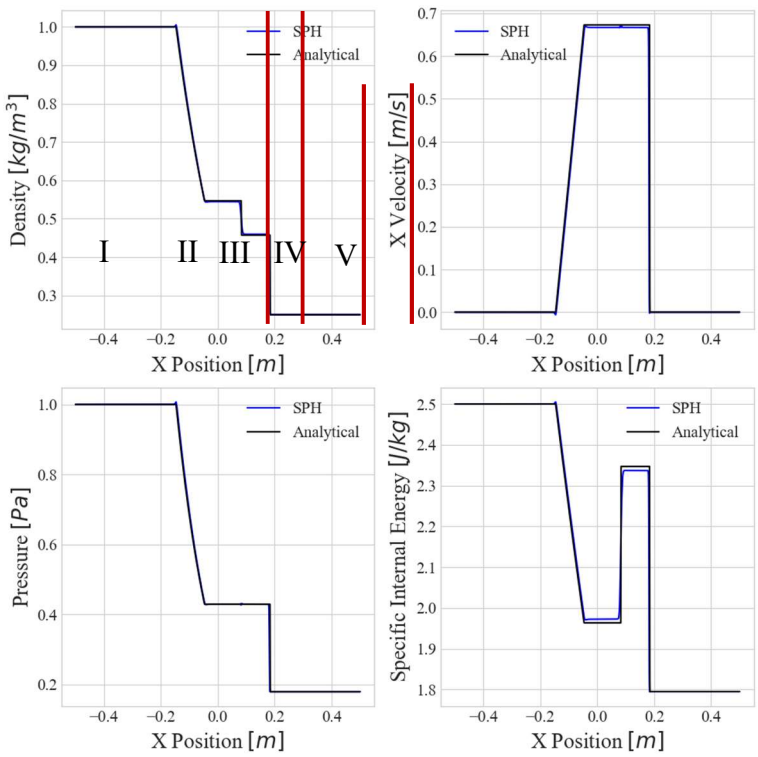

Figure 3-4: Results of the Sod shock tube problem, the shock, and expansion waves align well in time. The energy was captured to within 5% of the analytical solution.

The SPH solution represented the features of the shock well. Figure 3-4 shows the comparison of the SPH solution in blue to the analytical solution in black. The "pressure blip" phenomena known to SPH that occurs at the initial placement of the discontinuity was very small. The overall solution is within 5% of the analytical solution. The three key features of the shock tube are shown in roman numerals 3-5 of the first panel in Figure 3-1. The feature shown by numeral III is the rarefaction wave running to the left. The contact discontinuity is shown by numeral IV, and the right running shock wave is shown by numeral V. All features match the analytical solution and demonstrate the ability of the SPH code to solve strong normal shock problems.

3.5.3 The Noh Problem

The Noh problem was performed as a two-dimensional test case where an ideal gas was undergoing an implosion at the center point [83] [84]. Noh's purpose for this problem was to stress several different aspects of a methodology's behavior in strong shocks with a strong heating component [83]. Artificial terms in the heat conduction equation are necessary for controlling spurious oscillations that can occur in these problems. However, the controls often cause error in the internal energy causing an under or overshoot close to the central region of compression. The physical mechanism of this error was due to how the problem works. The setup had a uniform gas that had a constant radial velocity towards the center of the problem. At time zero, the center of the gas had an infinite stagnation shock that will move radial outward from the center [84]. The gas was initially cold, with a temperature close to zero in magnitude. As the shock wave moved outward, the gas that it had passed through was rapidly heated to extreme temperatures. This set up a discontinuity in the parameters behind and in front of the shock. The initial cold gas had a low sound speed, and when the shock formed, it was close to infinite in strength. These conditions provided a useful and easy to test case for the artificial terms to capture the correct solution. The Noh problem has an analytical solution, which made it a good test problem as it had a direct comparison to the answer [83].

According to Gehmeyr et al. the density of the post-shock region was calculated based on the ratio of specific heats [84] shown in Equation 3-67, if the solution is in the post-shock region.

$$\rho(x,t) = \rho_0 \left(\frac{\gamma+1}{\gamma-1}\right)^2. \quad 3\text{-}67$$

If the solution is outside of this region, then the solution becomes:

$$\rho(x,t) = \rho_0 \left(1 - \frac{u_0 t}{x}\right)^2. \quad 3\text{-}68$$

For this case, the ratio of specific heats was $\gamma = 5/3$, and the setup was consistent with the setup of Gehmeyr et al. [84]. A set of 20,000 points in a set of evenly spaced spirals, initialized to a uniform density of 1.0 kg/m^3. The velocity was 1.0 m/s directed radially inward towards the center of the cylinder. The pressure was a small but finite number $1x10^{-4}\ Pa$, so that the artificial terms provide reasonable starting points. The simulation was run from time zero to a time of 0.6 seconds. Using Equation 3-67, the post-shock density should be a value of $16\ kg/m^3$, the post-shock velocity should be zero. Figure 3-5 shows the results of the Noh cylindrical problem at a time of 0.6 seconds. The first panel shows the contour plot of the density, the cylindrical implosion was well maintained, and the system did not produce any unphysical asymmetric properties. The second panel shows the density in both the post-shock and pre-shock regions. The comparison of the analytical density with the SPH density shows that there was some error in the post-shock region; however, it was within the error tolerance specified. The maximum error was 7.5% of the analytical solution. The post-shock region shows that the density is dropping off below the analytical solution towards the center of the problem. This was due to some spurious wall heating caused by the simulation, and the artificial heat conduction terms. Noh's problem stresses this type

of thermal energy capture [84]. While that error did occur in the problem, it was not outside the error tolerance. A density drop at the edge of the problem around 0.4 m was due to the SPH density estimate. As particles lose neighbor resolution towards a vacuum, they experienced a density drop [45]. Noh's setup had an infinite gas collapsing inward, while this simulation was limited to a disk with radius 0.5 m.

Another aspect of the Noh problem unique to the SPH formalism was its ability to demonstrate whether or not particles are exhibiting a "clumping" phenomenon. Particle clumping occurs when the spatial resolution parameter h causes particles to overlap and aggregate together [56]. This happens because the spatial resolution of certain spline types can become poorly resolved as particles move around [56] [52]. Figure 3-6 shows the particle spacing of the problem space. The choice of a Wendland function for the weighting parameter was made to ensure no clumping occurs. Figure 3-6 shows that the post-shock region did not have disordered particles and the particles did not clump together. The pre-shock region showed the initial uniformly set up particles, forming a hexagonal lattice, common to multi-dimensional SPH simulations [39]. The shock region visible around the -0.2 m mark is also uniform; it caused the particles to shift so that the post-shock region was denser.

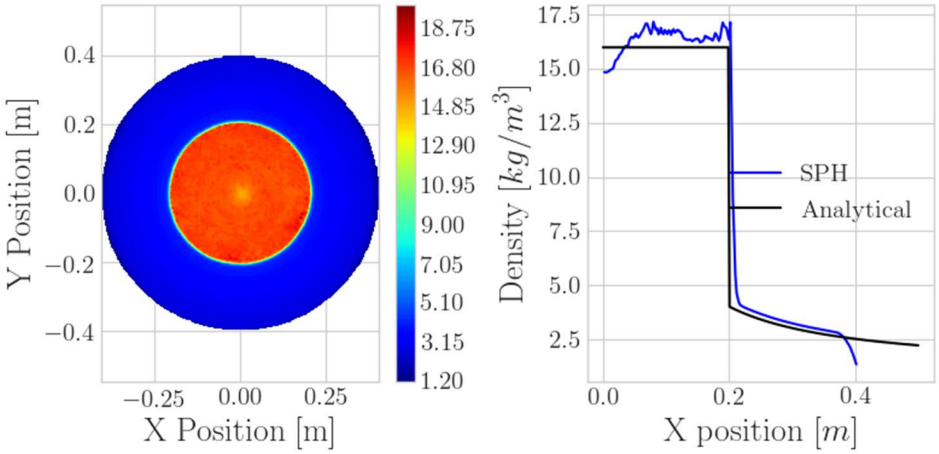

Figure 3-5: Noh's cylindrical test case evaluated at 0.6 seconds. The analytical value was shown in the black curve on the second panel. The blue curve shows the SPH solution. There was some noise evident in the SPH solution, however it does capture the shock region well and was within 7.5% of the analytical result. Some loss of density at the 0.0 mark was due the excess wall heating that Noh describes.

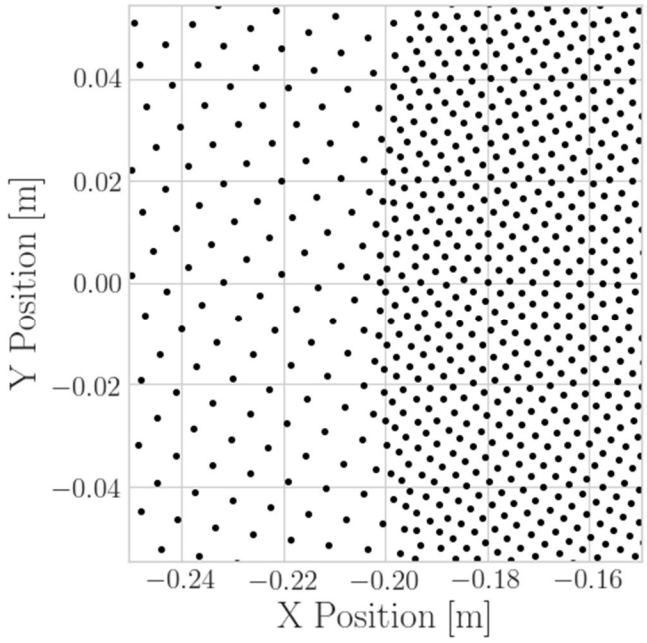

Figure 3-6: Particle resolution of the Noh cylindrical shock problem. The post-shock region is shown on the right side where the particles are more numerous. The pre-shock region shown on the left side has the initial particle spacing. The particles did not undergo any clumping and exhibit uniformity in their layout. The shock region does not show any instability in the particles or lead to clumping.

The important aspect was that the Noh problem result was well captured with respect to the analytical solution and particle behavior remains regular and uniform.

3.5.4 Kelvin-Helmholtz Instability

A Kelvin-Helmholtz instability problem was run to provide confidence in the SPH code's ability to capture instabilities [22]. There was a misconception that the SPH formalism cannot solve the K-H instability problem [62]. This was not correct as multiple authors have shown the capture of the K-H instability. Valcke et al. showed that SPH can capture

K-H instabilities [85], Price also demonstrated the capability of SPH to capture these instabilities [86]. McNally et al compared multiple numerical methods and standardized codes which included several main stream SPH codes [87]. Their findings showed that SPH was no better or worse than many other methodologies both gridded and meshless.

The Kelvin-Helmholtz instability is usually caused by two fluids of dissimilar densities moving in shear relative to each other [88]. The K-H problem not only tests the capability of the SPH method to form instabilities but it also tests the artificial terms to provide accurate control to the shearing fluids at the contact discontinuity between them. Chandrasekhar provided an analytical solution to the growth of the instability, shown in Equation 3-69.

$$\tau_{KH} = \frac{(\rho_1 + \rho_2)\lambda}{\sqrt{\rho_1 \rho_2}|v_1 - v_2|} \tag{3-69}$$

Equation 3-69 is the growth rate of the instability. The instability is a function of several factors. One is that to have the instability form there must be a difference in velocity, this is shown in the term $|v_1 - v_2|$ otherwise the instability is undefined. Second, the density of the two fluids may be different or equal and the instability can still form. The final value is the estimate wave length λ, where the wave length of the initial instability will set the growth rate.

The problem setup was consistent with the problem setup of McNally [87]. The main difference was that instead of modeling the fluid regions on both sides only one side was modeled. The length of the problem space was 1.0 m and the width was also $1m$. The density discontinuity was applied at the central point of the width taken to be 0.0 m. The lower density was set to be $\rho_1 = 1.0\ kg/m^3$, and the upper density was set to $\rho_2 =$

2.0 kg/m^3. A set of 120,000 particles was used spaced according to a constant particle mass. The specific heat was set to $\gamma = 5/3$. The pressure in both regions is uniform and set to 2.5 Pa. The particles were not provided an initial velocity in the y direction but the x direction velocity was -0.5 and 0.5 m/s for the top and bottom. The numerical noise in the shear layer will allow the K-H instability to form. The simulation was run to 2.0 seconds. Periodic boundary conditions were used on the left and right sides. These conditions ensure that the two sides provide reciprocity in the particle resolution and continuity across the borders to make the simulation continuous. The top and bottom borders of the simulation institute reflecting boundary conditions so that continuity of the particles is maintained. Figure 3-7 shows the formation of the Kelvin-Helmholtz instability at two seconds.

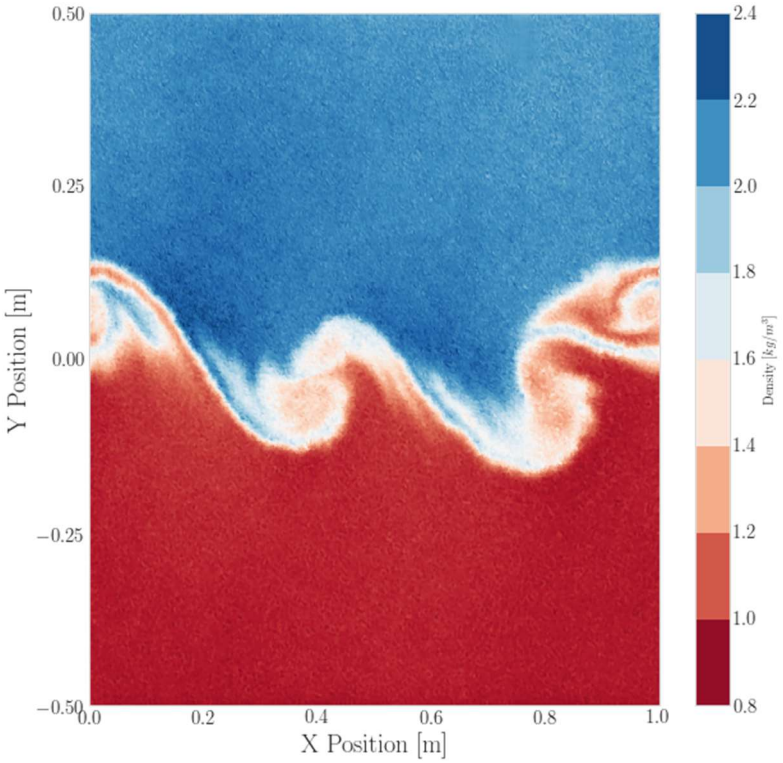

Figure 3-7: Kelvin-Helmholtz instability for a single shear layer in counter velocity flows. The classic vortices are formed and clearly visible.

The wave length was estimated from [59] to be $\lambda = 1/2$. Using Equation 3-69 and inserting the wave length into it, the growth rate was estimated to be.

$$\tau_{KH} = \frac{(\rho_1 + \rho_2)\lambda}{\sqrt{\rho_1\rho_2}|v_1 - v_2|} \approx 1.06 \qquad 3\text{-}70$$

Growth of the maximum specific kinetic energy in the y-direction is one metric used to compare the formation to the accepted values. McNally describes the energy as being

$$E_y = \frac{1}{2}\rho v_y^2 \qquad 3\text{-}71$$

Using Equation 3-71 and shown in Figure 3-8 the growth of the maximum energy was tracked in time. The SPH solution tends to gain energy very quickly but flatten out. These results are consistent with the results shown by McNally for SPH and other methods.

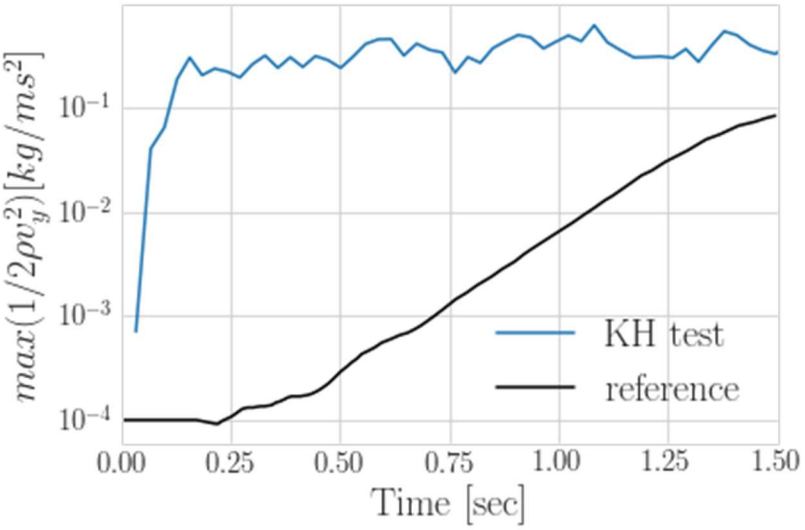

Figure 3-8: Specific y-kinetic energy growth in time compared to the accepted reference solution by McNally.

The growth rate of the instability can also be tracked in time. The growth of the instability trends with the standard reference case, where the initial deviation is due to our divergence from the standard setup. The solution does deviate from the accepted value but this is partially due to the way the initial perturbed velocity was set to zero. The final time point of the solution is close to the accepted solution.

While the solution to the K-H solution is not as good as desired it meets the goal of demonstrating the ability to capture the instability and have it manifest it with energy that approaches the accepted values. The exact need to capture the minutiae of these problems was not necessary for this analysis.

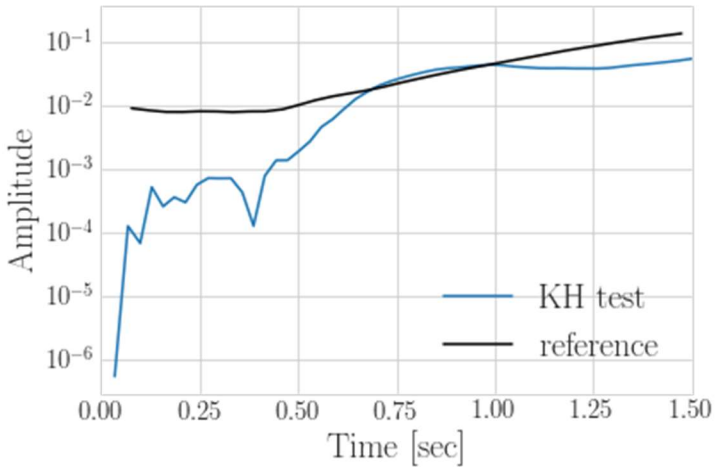

Figure 3-9: growth rate of the instability. This case follows a trend similar to other K-H tests. See reference [59]. Since no y-velocity component was used our solution starts at lower amplitude. A slightly different growth rate was due to no y-velocity initial component. The growth was slower during most of the simulation, which was consistent with other SPH K-H test growth rates.

3.5.5 Hydrodynamic merger of two plasma jets

The final hydrodynamic case was the comparison of the merger of two jets to the experimental case shown by Case et al. [15]. An experiment conducted in 2013 utilized some prior HyperV plasma railguns [89]. This experiment was conducted at Los Alamos, utilized two guns in a plane directing two jets to merge. These jets were separated at a 12º half angle along a 1.35 m axis and the jets were traveling at $40\,km/s$. It was noted that a region of low-density gas forms in the middle of the merged jet region. The

observation was made on the emission dip, consistent with a density drop confirmed in the interferometer data. In the CCD images of Figure 3-10 [89], undulations in the jets can be seen with scales of the order of 10 cm. While the scale lengths, densities, and some physics parameters are dramatically different, these structures were also observed in the bond zone in explosive clad metals and various high-energy metal working techniques [90].

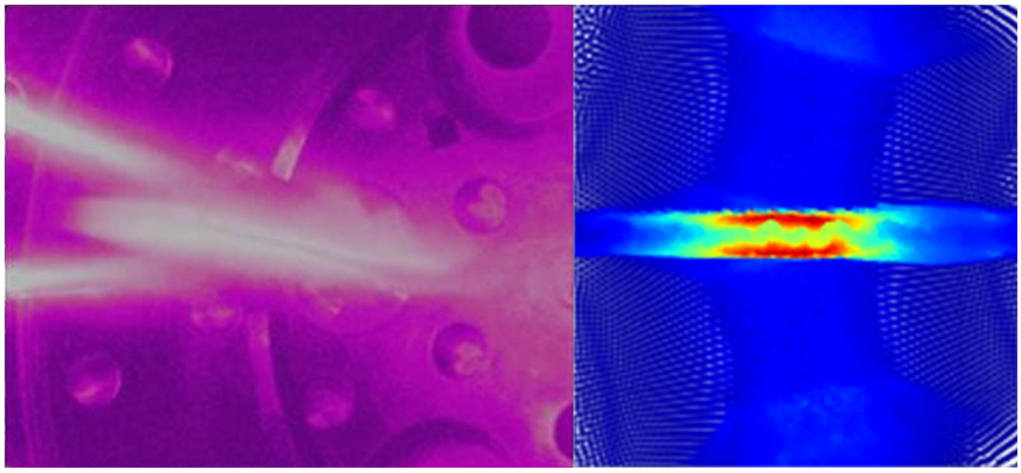

Figure 3-10: Comparison of the experimental jet merger on the left and the simulation of a jet merger on the right. Both are set to a merge half angle of 12 degrees. The experimental case and the simulation exhibit the separation region in between the two jets as they merge.

The setup for the jets cases was as follows and shown in Figure 3-11. The numerical setup neglects the plasma gun formation and assumes uniform properties. All jets start out with an initial uniform density of 1.2 kg/m^3. The velocities of the jets are initially 40 km/s, and the temperature is 32,000 K. A gas constant of 287 kJ/kg and specific heat ratio γ of 1.4 are used. The motivation for these angles was driven by comparison to 2013

experiment [89] and the PJMIF setup. In PJMIF, multiple jets merge to form a liner for target implosion. A typical PJMIF setup will use many jets arrayed in either a cylindrical or spherical configuration [10] [21] [23] [2]. The angle between the merging jets will be small and in the range of 6-18°, consistent with the experimental setup and the numerical simulation. In the numerical simulation the jets expand thermally while traveling to the intersection point. This gives the jets time to form gradients in density and temperature comparable to what was seen in the experiments, which was a Gaussian profile with higher densities and temperatures at the center.

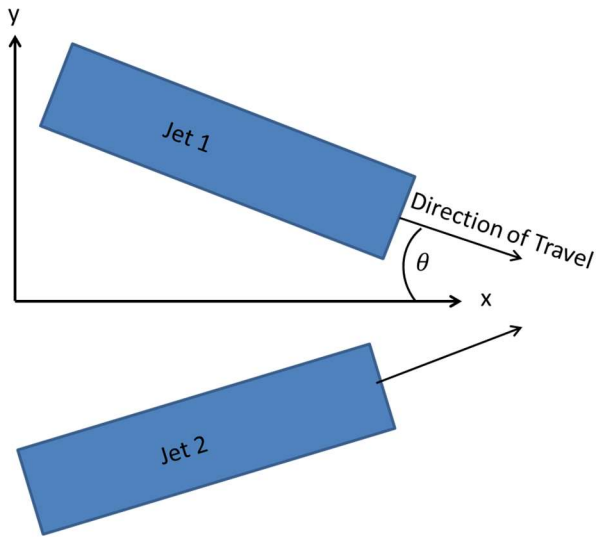

Figure 3-11: Setup for the two jet merger. The initial half angle of the jets is defined. The jets propagate along the x-y plane until they collide. The jets will expand in this process and the lower density regions will intersect first.

The simulation proceeds through several steps. First the jets propagate through a vacuum along their lines of intersection to the impact point. Thermal expansion at a rate of ~2c/(γ-1) caused the jets to expand both radially and longitudinally, creating a lower

density layer ahead of the main jets, where c was the sound speed and γ was the specific heat ratio [91]. The low-density region of the expanded jet first intersected with the opposing jet, creating an initial shock layer that can be approximated in strength by oblique shock theory using the initial jet Mach number and intersection half angle θ. The intersection plane which formed a virtual wall acted as a free slip plane line between the two jets, and in the reference frame of the jets this slip plane acted as a stationary deflection which caused a pair of oblique shocks to form, one for each of the jets. In the hypersonic limit, the density jump will scale as $(\gamma+1)/(\gamma-1)$ while the temperature jump was $\sim 2\gamma(\gamma-1)/(\gamma+1)^2 \, M^2 \, \theta^2$ where we have assumed the small angle approximation and thin shock assumption [30]. Following the initial merging of the jets, the bulk flow passes through the shock wave, and then expands thermally at a higher rate downstream.

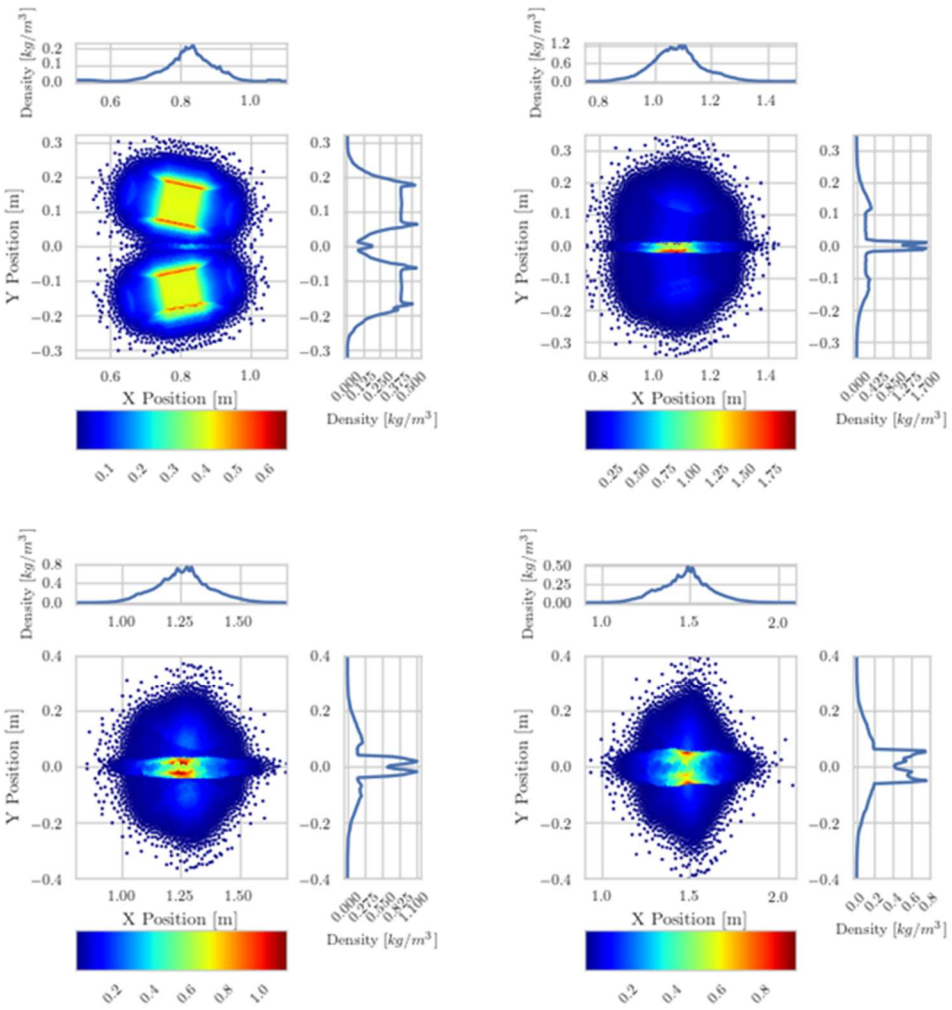

Figure 3-12: Mass density of the merging jets for a 12° half angle at 18 μs (upper left), 25μs (upper right), 30 μs (lower left), and 35 μs (lower right). The horizontal line slice above each contour plot goes through the merge plane at y=0. The vertical line slice to the right of each plot gives the density at x = 0.8, 1.1, 1.25, and 1.5 m, respectively. In comparing plots across time steps, it should be noted that the x and y scales and the color bar scale change across the figures to maximize contrast in the density field at each given time step.

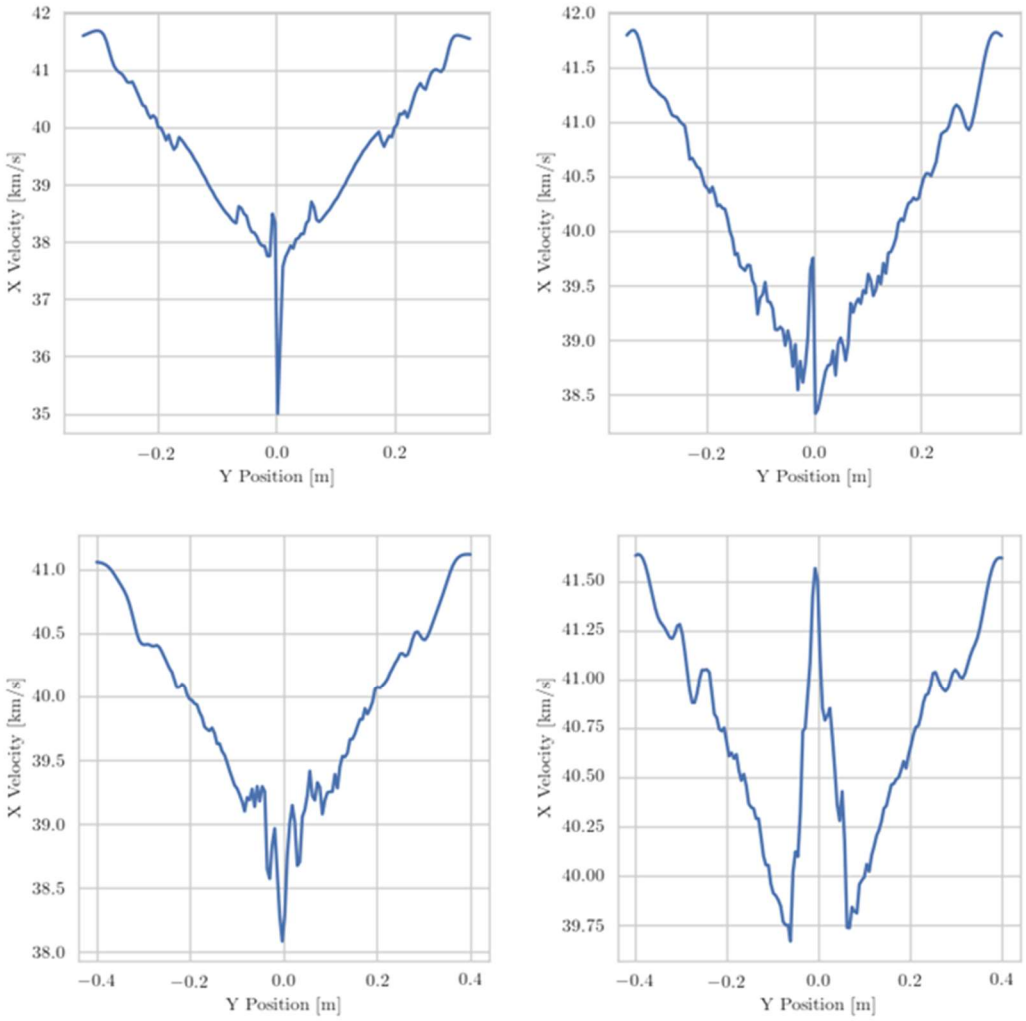

Figure 3-13: X-velocity (km/s) profiles through the y direction slices in Figure 3-12, 18μs (upper left), 25μs(upper right), 30μs (lower left), 35 μs (lower right). The central region of the plots shows the merged jet region. Velocity sign changes are due to where the slices are taken.

Figure 3-12 shows the merging of two plasma jets with an initial 12 degree half angle separation. The contour plots show the mass density in kg/m^3 of the jets as they merge.

The abscissa and ordinate are the relative position of the jets with respect to the chamber wall in units of meters. To quantify the merger process, two line slices are included for each of the four contour plots. On top of each plot is a line slice through the slip plane between jets (y=0), in which the x-axis is aligned with the contour plot. A vertical line slice is taken through the center of mass of the jets (locations given in figure caption). These slices were taken to facilitate a quantified interpretation of the results. At 18 μs, the thermally expanded halo around each jet is at least an order of magnitude below the ~0.3 kg/m^3 central core of the jets which are of the order of 15 cm in width at this time. The expanded regions interact first, creating a shock at the intersection which grows and eventually exceeds the core density, as the main jets reach the merge plane at 25 μs. At 25 μs, the central cores of each jet begin merging and have a pre-shock width of ~40 cm across the jets. The structure of the density field at the interface develops an interesting feature in which the shock region is highest at the top and bottom boundary just behind the shock, and exhibits a dip in the middle. This feature can be seen at 25, 30 and 35 μs and is consistent with the observations made in the PLXα experiment as seen in Figure 1. By 35 μs, most of the mass has entered the shock which is now about 15 cm across. The reason for this is that thermal expansion of the jets prior to reaching the slip line causes the outer edge of the jet to be less density, while the inner core remains high. Thus, the density drop is due to the outer low-density expanded plasma increasing in accordance with the jump conditions given the Mach number and turning angle, while the inner higher density portion of the jet experiences the same proportional shock jump but a higher initial density, thereby producing the observed dip at the interface.

In Figure 3-12, the density has an undulation along the central axis consistent with an instability formation. The undulation changes with time and begins to set up nonzero rotational flow as the jets continue to merge. The main objective of this paper is to offer a possible explanation for that feature which is seen in both the experiments and simulations. It has been hypothesized here that it is due to a Kelvin-Helmholtz instability, which in the reference frame of the simulations requires a non-zero velocity gradient du/dy. Figure 3-13 gives vertical line slices of the x component of velocity at the same time sequences of Figure 3-12. Figure 3-12 shows the progression of the jets merging. Using Figure 3-13 in conjunction with Figure 3-12 gives a qualitative understanding for the formation of a velocity gradient within the merging region of the jets. The initial shock forms a velocity shear evident from the large velocity change in the first panel of Figure 3-13. As the merger process continues the formation of the K-H instability can be seen in the upper right panel of Figure 3-12, while the corresponding velocity profile in Figure 3-13 demonstrates a large shear on the order of 50km/s/m. The lower right panel shows the continuation of both the merger and the oscillation in density and the velocity is apparent in the central regions of both figures. The lower right panels show the final merging of the jets with the density gradients and velocity gradients. The progression of the jets with the density change in the center is consistent with instability of the K-H type.

The nature of the two jets interacting in an oblique manner is inherently unstable. From Chandrasekhar's "Hydrodynamics and Hydromagnetic Instability" chapter 11, page 484, equation 33 [88]:

$$\lambda^2 \alpha_1 \alpha_2 (v_1 - v_2)^2 > gk(\alpha_1 - \alpha_2). \quad 3\text{-}72$$

Equation 3-72 governs the formation of the Kelvin-Helmholtz instability. The λ term on the left is the wave number of the instability, dependent on the problem formulation. The α terms are the ratio of one jet's density to the summed density of the two jets $\alpha_1 = \frac{\rho_1}{\rho_1 + \rho_2}$ [88]. The *v* terms are the velocity of the fluids. The right hand side is a gravitational term. In this case the gravity term is neglected due to the speed of the jets and the magnitude of the gravity term being insignificant, reducing to,

$$\lambda^2 \alpha_1 \alpha_2 (v_1 - v_2)^2 > 0. \quad 3\text{-}73$$

Equation 3-73 indicates that any velocity gradient will initiate instability in the absence of gravity [88]. The growth rate of the instability can be recovered by taking the square root of the left hand side of equation 3-73 and inverting it yields equation 3-71. We can conclude from Figure 3-13 that the velocity gradient is approximately 10,000 m/s per meter. Referring back to Figure 3-12, perturbations are visible at 25 μs and grow in size as the merger process continues. Comparing the case back to the experimental case shows favorable results. The experimental case has an oblique shock interface of 5° while the simulated shock interface has an oblique shock occurring at 4.2°. These cases are occurring at 30 μs. The jet setup mirrors the experimental setup with the wall being the origin and propagation being in the positive direction. Jet merger occurs at similar times and at similar points. The differences are from the simulation being discrete rectangular jets while the experimental results are jets that have a more drawn out appearance.

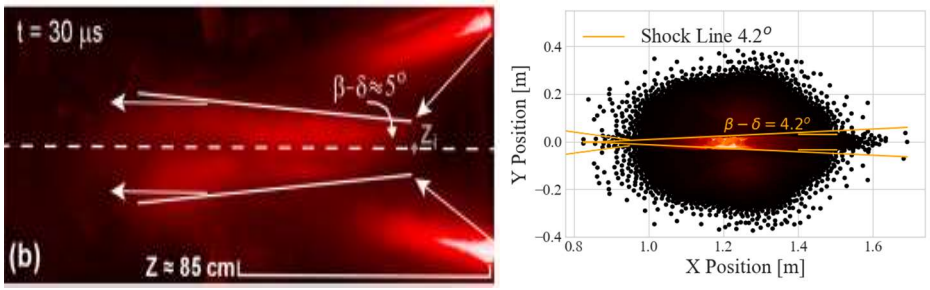

Figure 3-14: The left panel shows the merging of two jets experimentally. The right panel shows the simulated merging of two jets. The simulated jet merger shows a similar interface and shock angle as the experimental case. Both cases are at 30 µs from the beginning of the process start.

The growth of the possible Kelvin-Helmholtz instability can be predicted by examining the pre-shock and post-shock conditions and estimating conditions at these zones. The pre-shock density is about 0.25 kg/m^3 and post-shock density is 1 kg/m^3. Velocity shear across the shock is approximately 250 m/s. We apply a best fit to the discrete measured values at of 25, 30, and 35µs using the growth model, $A_o e^{\omega t}$. This best fit returns ω which is $121kHz$. This value of ω is implemented in equation 3-71 along with the velocities and shears estimated above to get the wave number. The estimate of the wave number is 4,848 per meter which corresponds to, $\frac{1}{0.00825\ _{jet}}$. From our model we estimate the starting amplitude to be 0.5% of the initial jet radius.

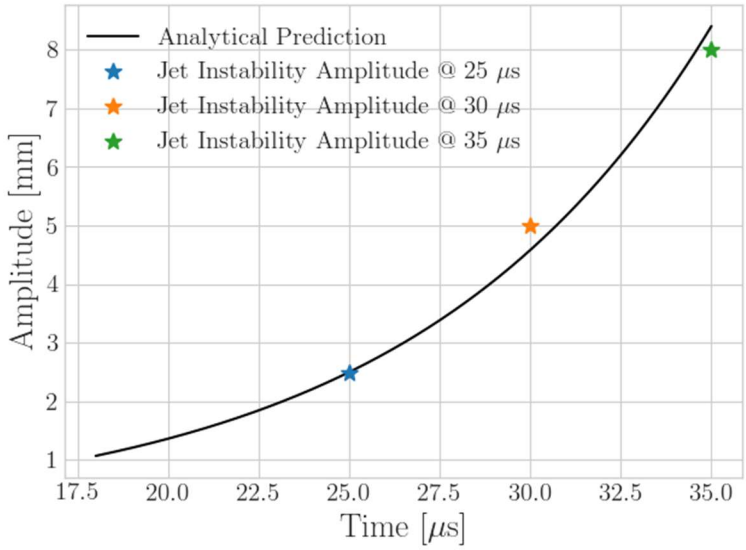

Figure 3-15: Growth of the amplitude of the Kelvin-Helmholtz instability within the jet merger region. The time scale is related to the start of the simulation. Where 18 µs is the estimated start of jet merger time and 35µs is the completion of the merger process.

3.5.6 Brio and Wu shock tube

The Brio and Wu shock tube test is the MHD analogy to the Sod shock tube test [40]. The purpose of this case is to stress the ability for a code to handle multiple physical regimes, including shocks in both the hydrodynamic and magnetic components [92]. Brio and Wu created this case to test upwind differencing schemes in gridded codes, but it has since become a staple problem of any method trying to solve MHD shocks [93]. This problem excites different modes in the MHD waves and demonstrates their ability to propagate [93]. The setup for the MHD shock tube is similar to the Sod shock tube. A diaphragm separates two gases at varying densities and pressures. The gasses have an

additional component, which is the magnetic field. The specific heat $\gamma = 2$ was used in place of the $\gamma = 1.4$, which was used in the Sod shock tube.

Table 3-2 shows the setup parameters for the Brio and Wu MHD shock tube case. This case is identical to the case run in references [40] and [39].

Table 3-2: Brio & Wu MHD shock tube initialization parameters.

Property	Left	Right
Density	1.0	0.125
Pressure	1.0	0.1
Magnetic field x component	0.75	0.75
Magnetic field y component	1.0	-1.0
γ	2.0	2.0

Shown in Figure 3-16 and Figure 3-17 are the results of the MHD shock tube. The SPH scheme captures the major components of the MHD shock tube. The most significant difference was in the right running slow shock. The right running shock was slightly underperforming to the analytical result and expended energy in the velocity terms. This outcome has been the case in other results, such as Price [39] and Vanaverbeke [40]. Overall, the solution was within a 10% error of the accepted solution. This problem demonstrated the codes ability to capture multi-component physics with many wave types at once.

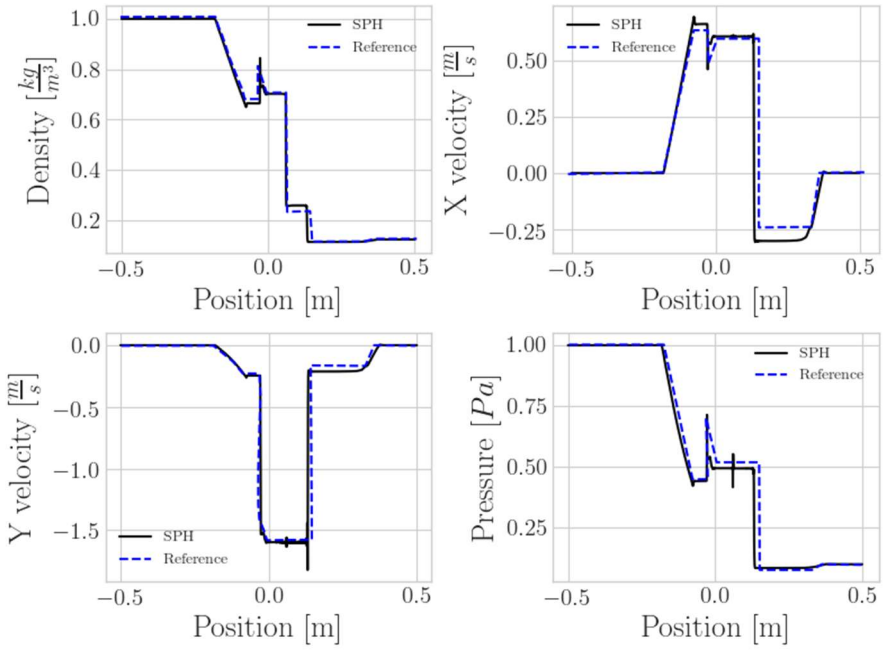

Figure 3-16: Comparison of the SPH solution (in black) to the accepted solution (in blue). The first panel is density, and the necessary components of the shock, rarefaction waves, and MHD waves are visible, the magnitudes are correct. A slight delay in the discontinuity, as well as undershoot, was shown. This undershoot was due to the incorrect energy, compared to the reference case. The second panel represents the x component of velocity, which represented the velocity well. The first panel on the bottom is the y velocity, which compared well to the reference case. The final panel was the pressure it also demonstrated all critical features and is reasonably matched the reference. The worst error is 10% of the reference case.

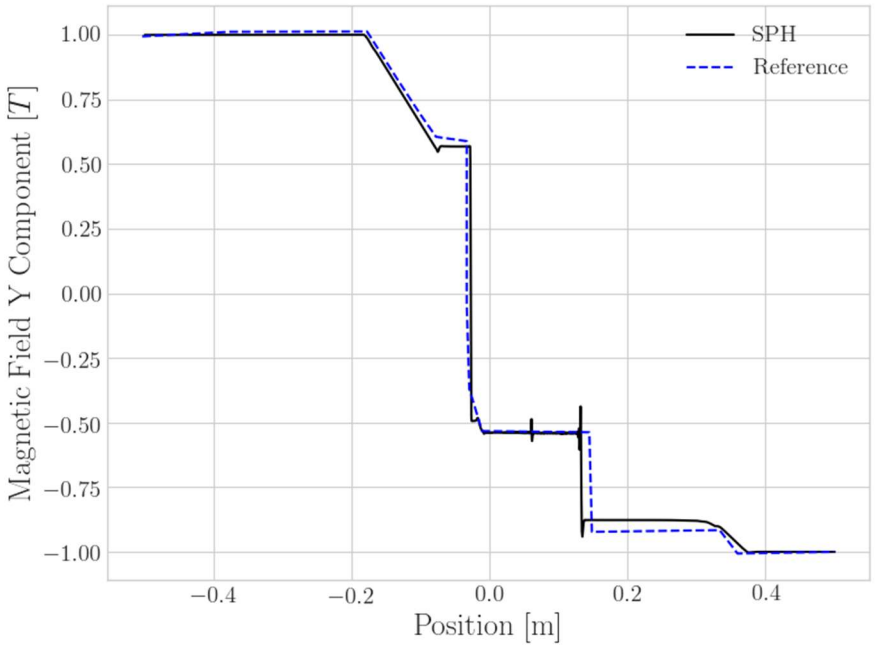

Figure 3-17: Results of the y component of the MHD shock tube. The components of the MHD waves are well represented and captured within a 10% error. The slight undershot in the SPH result (black line) compared to the accepted result (blue line) was due to the difference in the energy between the accepted result and the numerical result.

3.5.7 Fusion Power Equation

Fusion power balance is an important aspect of this analysis. Proper capturing of the fusion power deposition into the plasma target and liner is necessary to achieve fusion ignition and continued burn [17]. The fusion power is given by Equation 3-6 and is a function of several components. The η term is a factor for energy deposition. The $\overline{\sigma v}$ term is the cross-section of the reaction for DT. The number density of Deuterium and Tritium is the third term. The final term is the alpha particle creation energy. A DT reaction created an alpha particle at 3.5 MeV. The cross-sectional energy is a complex function; for this analysis, it was simplified down to be a function of the temperature in

keV of the SPH particle. A fourth-order curve fit was produced to represent the fusion reactions presented in Figure 3-18. Figure 3-18 shows that the curve fit reproduces the fusion reactivity with small deviations. The reactivity is set to zero when below the 1 keV range and set to the last good reactivity value at the 1000 keV range. The NRL Plasma Formulary provided the reactivity data for the DT reactions [28].

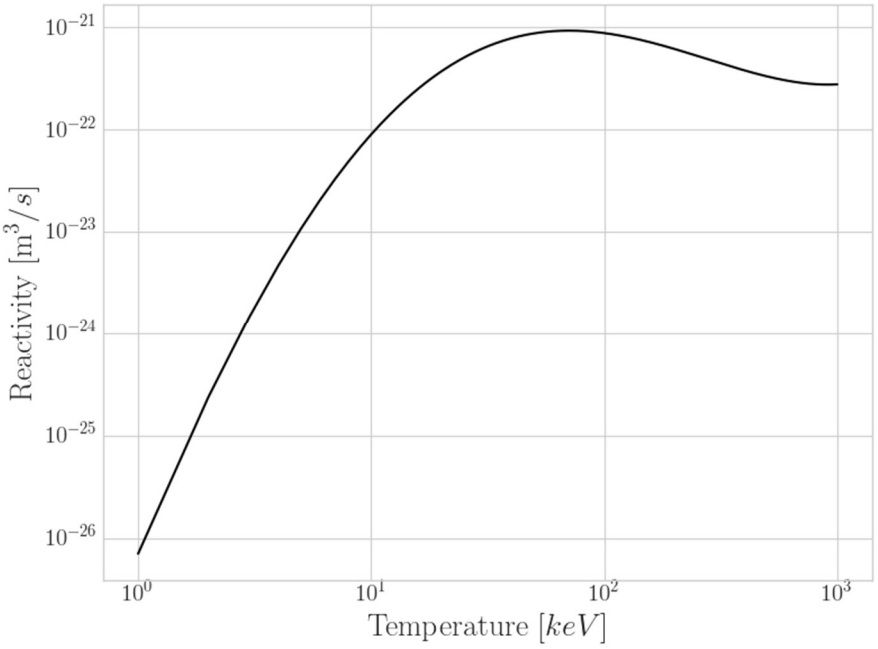

Figure 3-18: Fusion cross-section reactivity in blue, compared to a 4th order curve fit in black. The curve fit represented the exact fit well, but deviated beyond the limits of the temperature axis. If the temperature was below 1 keV, it assumed that the fusion cross-section is zero if the temperature was above 1000 keV, the reactivity was held constant to the last value.

To test the deposition and heating of a fusion plasma a simple integration of Equation 3-6 was performed in time. The energy term calculated in Equation 3-6 was

deposited back into the system and the process repeated over a time of 0.1 μs. This time frame was the anticipated time frame of a PJMIF process. The setup consisted of a plasma density of 10^{28} #/m^3 plasma equally split by DT. The Starting temperature was 5 keV, which was similar to the analysis cases presented in the next chapter.

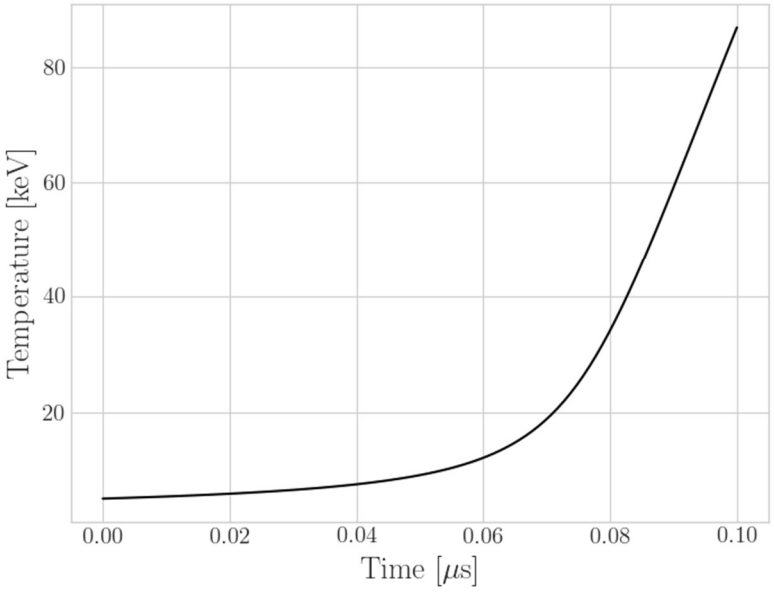

Figure 3-19: Fusion deposition test case. The fusion power deposition showed that positive fusion heating will occur if the temperature was within the temperature band of the reactivity curve.

Figure 3-19 shows the heating capabilities of just a fusion power term starting at a reasonably small temperature of 5 keV. No loss terms are shown so the plasma was free to heat without loss demonstrating heating capabilities.

3.5.8 Thermal Conduction

Thermal conduction can be a source of significant heat loss from the target, as noted by Kirkpatrick in reference [16]. The SPH method was modified to include a heat conduction term in the internal energy equation. The conduction was modeled using Equation 3-62. The test case of Jubelgas was utilized to test the accuracy of the thermal conduction model [81]. This problem was a one-dimensional test case; two slabs are in contact with different temperatures, but similar thermal conductivities. The initial internal energy profile of the slabs is discontinuous across the contact point. As time passes, the slabs thermally equalized and formed a smooth energy gradient across the contact. This test had two crucial points. One, it had an analytical solution allowing for direct comparison of the method back to a fixed solution. Two, it tested the energy transfer and capture of the second-order derivative and its ability to maintain the total energy of the system. The analytical solution to the one-dimensional conduction problem is given by reference [81] and presented in Equation below:

$$u(x,t) = u_o + \frac{\Delta u}{2}\operatorname{erf}\left(\frac{x - x_m}{\sqrt{4\alpha t}}\right). \qquad 3\text{-}74$$

The term u_o was the mean thermal energy of the system and x_m was the contact point of the two slabs. The term Δu was the difference in thermal energies at the starting point.

The setup used 250 particles of equal mass and spacing. The thermal conductivity was set to a value of $\alpha = 1cm^2/s$, in both materials. The material density in both slabs is set to $1kg/m^3$. The internal temperature of the left slab was set to $0.1J/kg$, and the right slab was set to $0.2J/kg$. The contact point was set to the origin of the system and both slabs were $0.5\ m$ in length. The test case was run to a time of 5 seconds. Figure 3-20 shows the SPH and analytical results of the thermal conduction test case. The SPH solution was in

good agreement with the test case and can maintain energy of the system while calculating the time evolution of the energy profile.

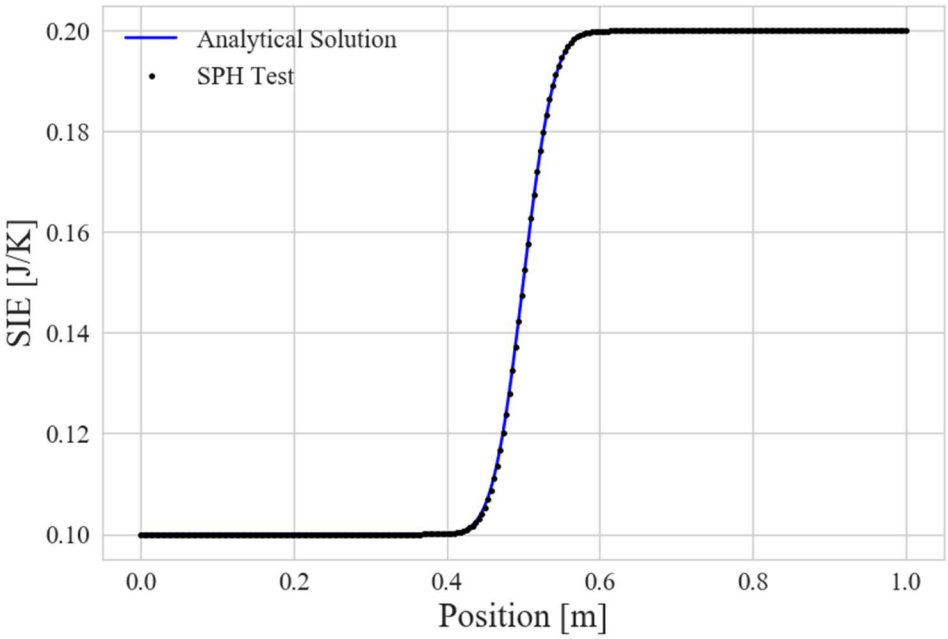

Figure 3-20: Thermal conduction test case. The analytical solution in blue and the SPH solution in black are identical with a maximum error being less than 1%.

3.5.9 Bremsstrahlung Radiation Test

The final test case is to demonstrate the ability of an SPH particle to radiate with Bremsstrahlung power based on its density and pressure. In this test case a set of particles were set to a constant density and uniform temperature. Only the Bremsstrahlung power was turned on. The particles are allowed to radiate away energy without any absorption. The loss in energy was compared to the numerically integrated Bremsstrahlung power given in Equation 3-12. In this case 250 particles were set to a density of 1 kg/m^3 and a

temperature of $1\ keV$. A specific heat ratio $\gamma = 5/3$ was used. Pressure was calculated with the ideal gas law and the specific gas constant $\bar{R} = 287\frac{J}{kg-K}$ was used. The system was integrated for $8\mu s$. This case was representative of temperatures that will be seen in analysis cases in the following chapter. Figure 3-21 was the outcome of the test case.

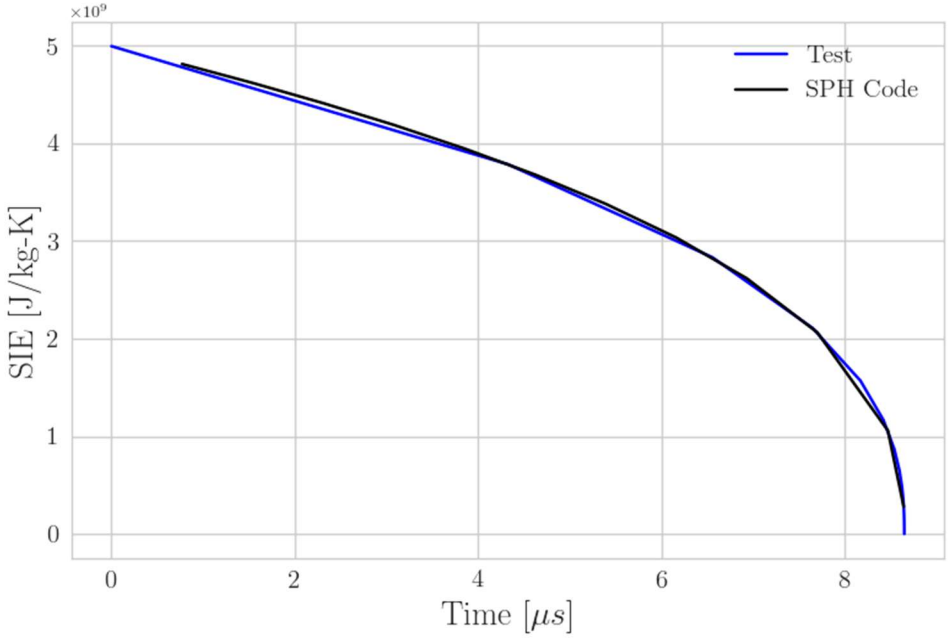

Figure 3-21: Bremsstrahlung radiation loss of an SPH particle. In blue, the test case accepted the result, and in black was the SPH case. Both cases are in good agreement through time and represent the energy loss to radiative cooling well.

The SPH case followed the integrated test case very well in time. The energy was lost at the same rate through time.

CHAPTER 4. RESULTS

4.1 Introduction

The analysis initially intended to explore compression to ignition of a cylindrical target and liner. Unfortunately, we did not find the compression of a target by the multilayer liner able to reach ignition conditions. Exploratory studies showed that target compression was to slow to overcome the losses from thermal conduction and radiation. Earlier analysis used time-independent models to calculate power balance, because of this method, compressional work was shown to be useful for raising the target to ignition. However, target thermal rates were different for each of the power balance terms, with the compression being slowest.

The initial target temperature was 700 eV. The compression of the target initially increased the temperature toward 1 keV, but radiation and thermal conduction would cause the target to dramatically cool. Cooling quenched the fusion reactions and prevented target ignition due to the $\overline{\sigma v}$ term inside the fusion reactivity (Equation 3-6) is dependent on the temperature, below 1 keV fusion reactions are too infrequent to heat the target. Therefore, the only heating mechanism during the initial phase was the heat produced from the compression, which was unable to overcome the loss terms.

The lack of ignition pushed initial target temperatures upward. Target temperatures were raised from 700 eV to 5 keV in 1 keV increments. A pronounced increase in heating occurred at a target temperature of 5 keV. At this point, compression of the target caused an initial increase in temperature, and the target heating was faster than the loss terms

would remove energy. This temperature became the reference point for the analysis presented below.

Table 4-1: Reference case values for the setup of the target and liner.

Reference Parameter	**Value**
Density of Target	5.5 kg/m^3
Target Radius	30 cm
Target Temperature	5 keV
Target Magnetic field (z direction)	50 T
Target Velocity	100 km/s
Inner Liner Radius (DT)	9 cm
Outer Liner Radius (Ar)	39 cm
Liner Temperature	2.5 eV
Inner Liner Density (DT)	5.5 kg/m^3
Outer Liner Density (Ar)	55 kg/m^3
Liner Velocity	100 km/s

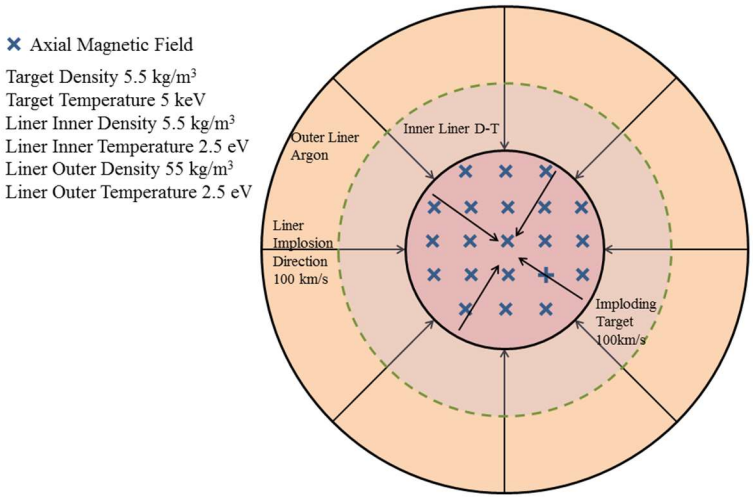

Figure 4-1: Target and liner setup for the cylindrical PJMIF cases studied. The target was uniformly compressed by a plasma liner. Both the target and liner shared the same implosion velocity. The multilayer liner acted as a containment system to the high temperature target. Thermal conduction of energy from the target acted as a source of heating to the inner DT layer of the liner.

4.2 Results and Discussion

The reference case consisted of a cylindrical liner compressing a self-imploding target. Figure 3-1 provides a schematic of the target and liner configuration. Both the target and the liner are imploding radially inward at 100 km/s. The target consisted of an equal mixture of both DT, while the liner was comprised of two layers, an inner equal mixture ratio of DT and an outer layer of singly ionized argon. The initial conditions for the reference case setup are shown in Table 4-1. The parameter case was chosen so that the ρR term and minimum temperature were in a positive fusion yield space based on the work of Kirkpatrick and Lindemuth [8] [12].

Kirkpatrick and others made use of Lindl-Widner (L-W) diagrams for prediction of regions of positive gain [9] [13] [94] [14]. L-W diagrams are a zeroth order power balance model used in ICF and PJMIF modeling. L-W diagrams are a contour map of the power balance of a target based on its initial conditions. The L-W diagrams map regions of positive gain by relating the initial aerial density (ρR) to temperature of the target. The power balance model consisted of four terms: work done by compression, fusion energy deposition, radiation loss, and thermal conduction loss. Equation 4-1 is the power balance model used in this paper and in the L-W diagrams:

$$\frac{du}{dt} = \left(\frac{du}{dt}\right)_{Work} + \left(\frac{du}{dt}\right)_{Fusion} - \left(\frac{du}{dt}\right)_{radiation} - \left(\frac{du}{dt}\right)_{conduction}. \quad 4\text{-}1$$

The first term on the right-hand side was the work done by compression of the target. This term represented the hydrodynamic effects of compression on a target. In our analysis this term was modeled using the ideal MHD equations provided in the modeling section. The second term represented the energy deposited back into the plasma from the fusion alpha particle products. Fusion reactions within the target produced alpha particles, which provided a source of heating. Target heating was necessary to increase the reactions in the target and achieve fusion burn. This term was modeled by Equation 3-6 using the deposition factor calculated by the Basko and Kemp model [6]. The deposition modeled the effect of an alpha particle traveling through the plasma, colliding and transferring part of its energy to the target. Energy deposition was modeled using Equations 3-7:3-11. Radiation was the third term on the right-hand side and was modeled using Bremsstrahlung radiation (Equation 3-12). Bremsstrahlung radiation was the dominant radiation term for these processes based on the work of Kirkpatrick [9].

Radiation was a loss term, thus, it was subtracted from the power balance. Energy lost by radiation was assumed to be removed from the system. No attempt at absorption was made in this analysis. The final term was the power loss due to the thermal conduction of energy from the target. This was modeled using the SPH methodology and was based on Equation 3-62. Kirkpatrick determined that thermal conduction across the field lines would be a dominant loss term for power balance. Thermal conduction represented the energy removed from the target by being in contact with a cold liner. Thermal conduction was a loss term and was subtracted from the overall power balance. Figure 4-3 is a L-W diagram of the fusion gain space for a cylindrical target at a magnetic field strength of 50T. The reference case was chosen so that it falls into the region of positive heating. The L-W diagram predicted that the reference case will have a gain greater than unity. This analysis determined the final gain for the reference was on the order of three.

In previous work, the liner compressed a preheated (~200 eV) target to fusion ignition conditions. In this work we found that the liner compression alone was too slow to overcome radiative and thermal conduction losses for cylindrical compression, and this may be attributed to cylindrical instead of spherical compression. These thermal losses led to the liner being used as a confinement device to prevent the target from expanding and cooling. We chose cylindrical compression in this work to explore possible parameters for ignition in cylindrical geometries, which may reduce complexity of experimental testing at the expense of the more favorable $1/r^2$ compression of spherical targets.

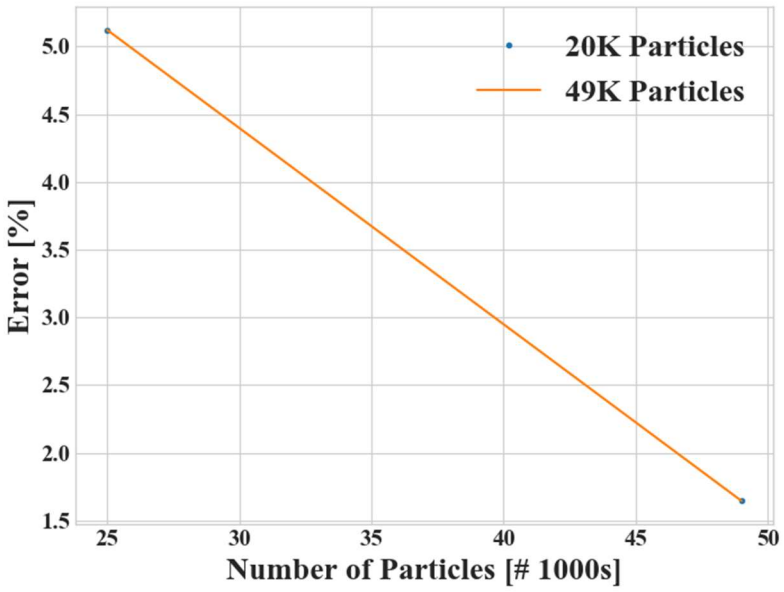

Figure 4-2: Convergence testing of different particle resolutions.

Several cases at differing particle resolutions were run to ensure proper grid convergence was attained. The particle numbers were 25k, 49k, and 68k particles in the reference case, with the last particle density being used as truth. Figure 4-2 shows the results of convergence testing. The baseline case for the reference was run using 49k particles, which had an error of 1.5%. This error was considered acceptable for the following results, and subsequent higher resolution cases were not needed.

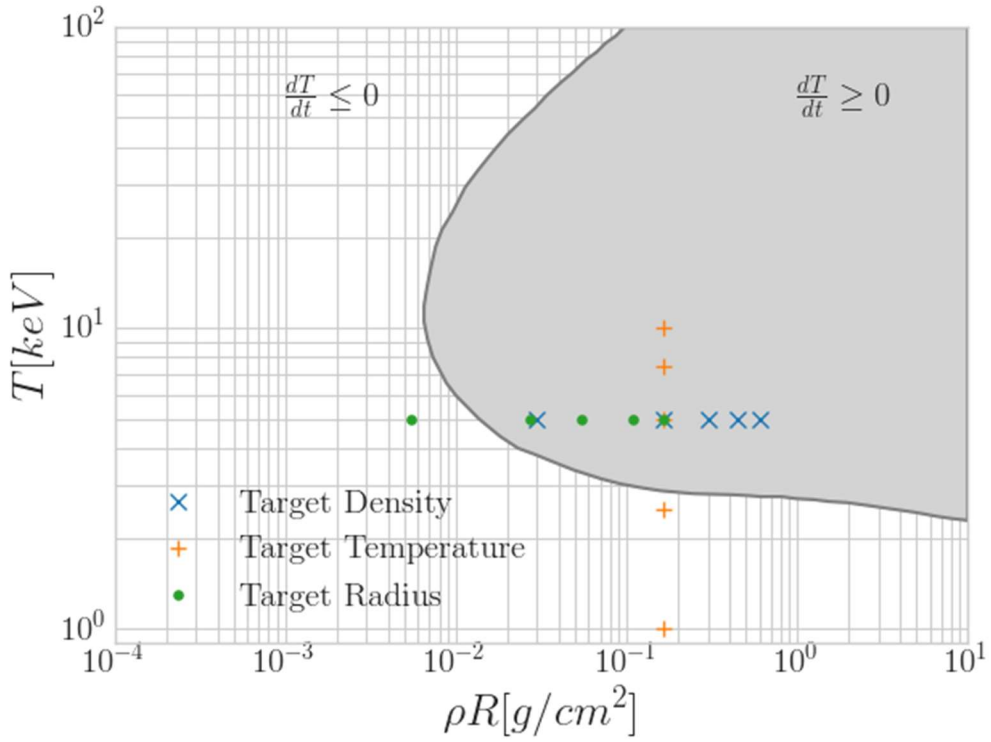

Figure 4-3: The Lindl-Widner parameter space for a cylindrical target with 50 T magnetic field. The grey region is the point at which target ignition becomes possible due to proper scaling of the target parameters in the ρR vs T parameter space. The test cases are shown in the color-coded markers. Cases were designed to test the interior, exterior, and dividing point of the region.

Six time-sequential line plots were used to analyze the reference case's power balance and explore fusion ignition. Each figure is a snapshot in time of density, temperature, and power balance terms across a radial cross section of the target and liner. The initial setup of the simulation is provided in Figure 4-4 using the initial conditions given in Table 4-1. The target was modeled as a circle and was encompassed by the liner. The density was

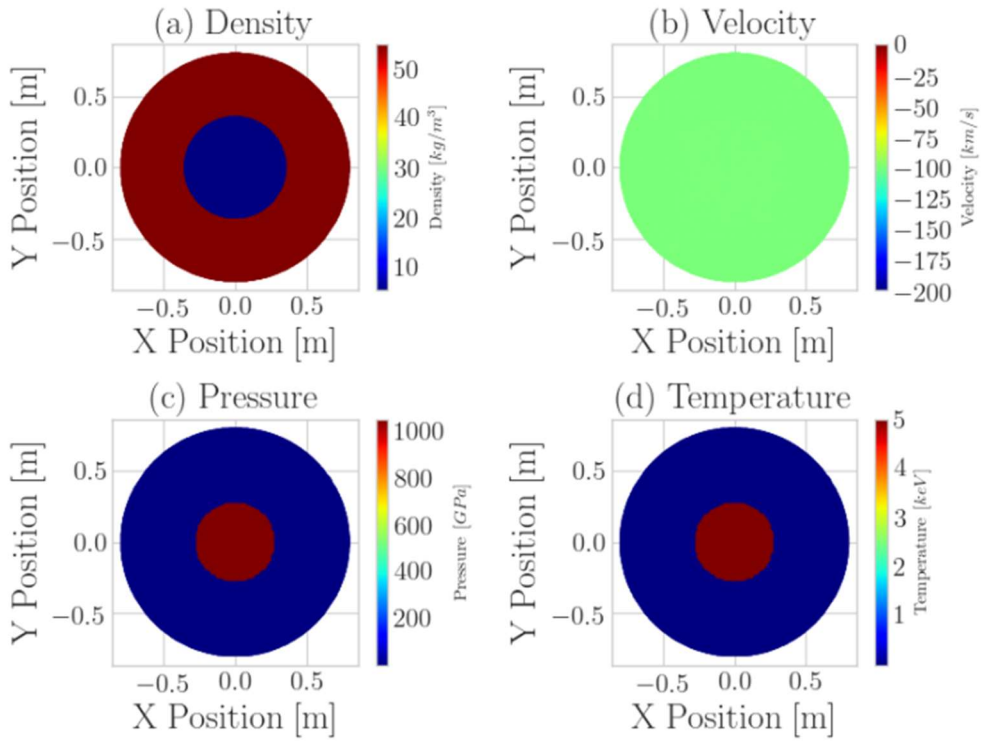

Figure 4-4: Initial conditions for the reference case as described in Table 4-1

discontinuous at the interface of the inner and outer liner. The velocity of the system was directed radially inward at 100 km/s. Pressure and temperature reflected the initial setup. Figure 4-4 shows the density, temperature, and power balance of the reference case at the initial setup. Three regions are denoted on the plots, representing the target, inner, and outer liner. The upper plot shows the density, with the inner liner and target at a density of 5.5 kg/m^3. A sharp discontinuity existed between the inner liner and the outer liner, due to the higher-density argon that made up the outer liner. Argon acted as a high-density pusher to contain the target during the fusion process. Temperature was discontinuous between the target and the inner liner. The target initial temperature was 5 keV while the inner liner was 2.5 eV. This was modeled based on the expectation that

the liner will be comprised of cold jets that have coalesced into a uniform liner [89] [22] [23]. The final plot is a comparison of the four power balance terms in the L-W model. The compressional work term is represented in blue.

The center of the target, represented at a radial value of zero, showed that the inward motion of the target increased the compressional work. This was shown by the positive increase in the blue curve at the center of the target. The power output in the target and the liner was significant, due to this we used the abbreviation EW to represent exawatts of power produced. Compression was the dominant power term at 2 EW/kg. The outer target and liner were at similar velocities and did not experience compression at the start of the process.

The target's initial temperature of 5 keV provided an initial fusion power that is 0.5 EW/kg, shown by the black curve. Because the temperature was constant across the target, the fusion power term was also constant. At the interface between the target and liner, the sharp temperature drop caused the fusion power to fall to zero. This was due to the fusion reactivity being a function of temperature, with the sharp drop in temperature effectively turning off the fusion power.

The thermal conduction is represented by the gold curve. The uniform conditions of the target and the liner made the thermal conduction zero in the central regions of the target and liner. The interface between the target and the inner liner had a temperature gradient which led to a large conduction of energy (~4-6 EW/kg) from the target to the inner liner.

Bremsstrahlung radiation is represented by the red curve. Radiation is dependent on two main factors, density and temperature. Equation 3-12 showed that radiation is a function of number densities for DT. Since they are equal mixtures this was approximately the

square of the number density. This implied that higher densities will have greater radiation. The radiation was also dependent on the square root of the temperature. Evident in the plot is that radiation was present in the target at the start of the simulation; however, radiation was not dominating the overall power balance. Total power balance was provided by the purple curve. Total power closely followed the compressional work towards the center of the target. Progression out from the center showed that fusion power became the dominant term until it reached the target/liner interface. Once at the target/liner interface the overall power balance dropped to a small fraction (< 0.1 EW/kg) of the power.

Atenzi and Meyer-Ter-Vehn suggested that if a central hot spot should form, it could ignite fusion burn [95]. To accomplish this, a hot spot must gain energy at a specified rate of:

$$t_{sh} = \frac{E_h}{W_{dep}}, \tag{4-2}$$

where E_h is the energy of the hot spot and W_{dep} is the deposited energy in the hot spot from fusion and compressional work. In our current setup, the target was the hot spot with energy at the center point of $2.8\text{x}10^{11}$ J/kg. The energy deposited into the hot spot of our target was estimated from the central region of Figure 4-5 to be $2\text{x}10^{18}$ J/kg-s. We used these values in Equation 4-2 and estimated a hot spot ignition time of 0.14 μs. The upper bound on fusion burn was provided by the confinement time of the liner. The liner confinement time can be approximated as the time it takes for a sound wave to propagate through the liner. This is shown below:

$$t_{con} = \frac{th_{liner}}{\sqrt{\nu \bar{R} T}}, \tag{4-3}$$

where t_{liner} is the thickness of the liner. In this analysis the outer liner thickness was used. The outer liner thickness for the reference case was 0.39 m. The denominator was the sound speed with γ as the specific heat ratio and was 5/3 in this analysis. $\bar{R}$ Was the specific gas constant, 3306 J/kg-K. The final term was the temperature, with the target at 5.8×10^7 K. Substituting these values into Equation 4-3 showed the estimated confinement time to be 0.6 μs. This showed that for the reference case, fusion ignition should begin to manifest by 0.14 μs and the expected process time for burn should be approximately 0.6 μs. The next time point was analyzed at the hot spot ignition time.

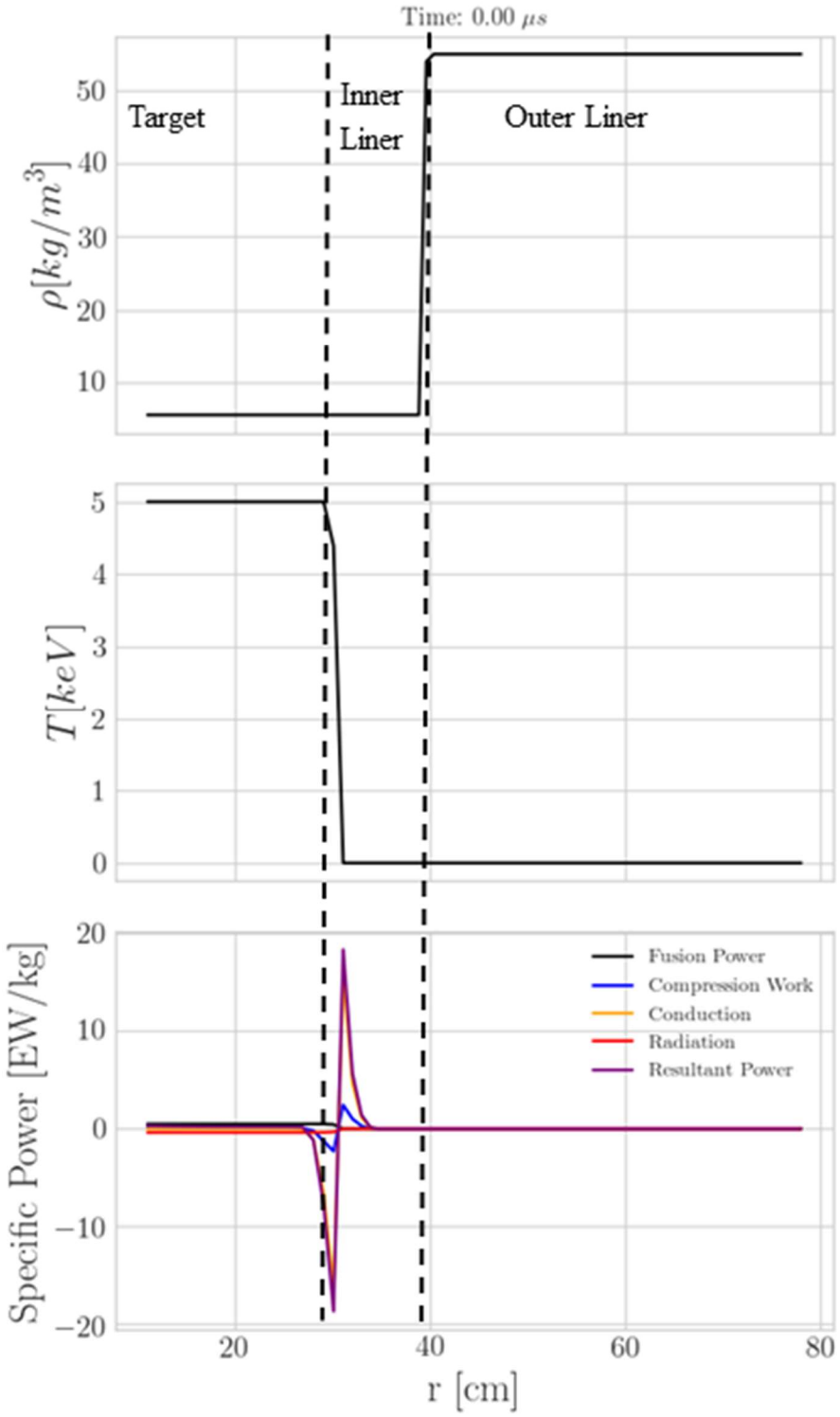

Figure 4-5: Initial radial configuration of the simulation. There are three regions: target, inner liner, and outer liner.

Figure 4-6 shows the radial change of density, temperature, and power balance at a time of 0.14 μs. At this point in time, compression of the target coupled with fusion heating had increased the density of the target from 5.5 kg/m^3 to 7.5 kg/m^3. The outer liner density had also increased but to a lesser extent. The biggest contrast in density change was at the inner liner. The inner cold liner was compressed against the hot high-pressure target. This caused the inner liner density to increase. The inner liner density was now ranging from 7 kg/m^3 to 55 kg/m^3. Temperature within the target had significantly increased from the starting value of 5 keV to 7.5 keV. The target was conducting away a significant amount of power, evident by the rounding of the temperature profile, shown in the thermal conduction profile. The inner liner now had a sharp thermal gradient. The inner liner had gained energy from the target through thermal conduction and the target/liner interface was at a temperature of 4 keV. At 4 keV the inner liner was starting to produce fusion energy approximately equal to the loss from conduction and radiation. This was seen at the edge of the target liner interface where fusion power was starting to rise. Fusion power was the sole dominant term at this stage of the process; this was expected from the ignition burn time. The work done by compression was limited. Compressional work was oscillating about the zero point and this indicated that the target was beginning to stagnate. Stagnation was evident by the overall compressional work being zero. The very center of the target had a negative work term that implied the central portion of the target was trying to expand. Conduction carried away energy from the hot central portion of the target to the outer region of the target and the inner liner. Thermal loss from the target degraded the overall instantaneous yield of the target. Thermal

conduction heated the inner liner to fusion temperatures. This was an important and expected process for PJMIF. Thio and Kirkpatrick hypothesized that a cold inner layer of DT of the liner could be made to ignite and bootstrap fusion gain [23]. Radiation continued to be a loss term but its relative importance to the power balance model put it last in the overall energy balance. Since the target density had not significantly changed, the overall radiation was constant and proportional to the starting value. The total energy was positive from the center of the target out to 20 cm. Most of the target was heating and producing fusion power.

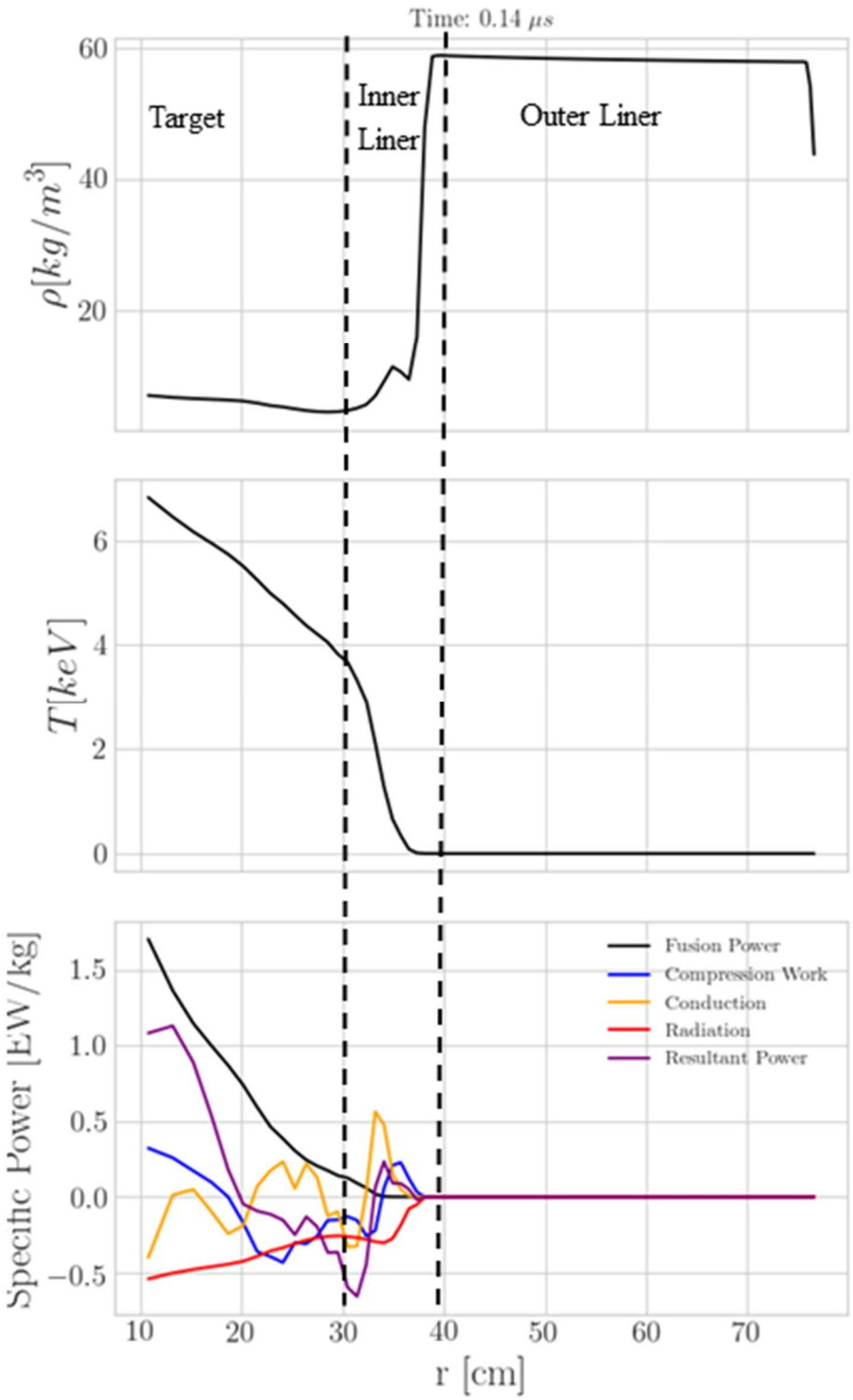

Figure 4-6: Profile of density, temperature, and power balance in the target and liner at 0.14 microseconds.

Figure 4-7 shows the density, temperature, and power balance at 0.24 μs. Density for the target had only a slight change, dropping from 7.5 kg/m^3 to 6.5 kg/m^3. The inner liner density transitioned between the target density and the outer liner density of 55 kg/m^3. The outer liner compressed the inner liner slightly and a shock formed on the interface distinguished by the uptick in density at the inner/outer liner interface. Target temperature increased from 7.5 keV to 12.5 keV. This temperature increase was due to the fusion power being deposited back into the target from alpha particle collisions. The central region of the target was the hottest part and a thermal gradient was causing thermal conduction to carry energy away from the center of the target to the outer target and inner liner, shown by the gold thermal conduction curve. The inner liner temperature crept up slightly from before, as had the fusion power at the target/liner interface. Target fusion power was now at 7.5 EW/kg which was a factor of three increase from the previous time analysis. Bremsstrahlung radiation had not changed and continued to be a minor source of energy loss for the target. Notably, compression was now negative from the center of the target to the very edge of the inner/outer liner interface. This implied that the target stagnated and was starting to expand outward.

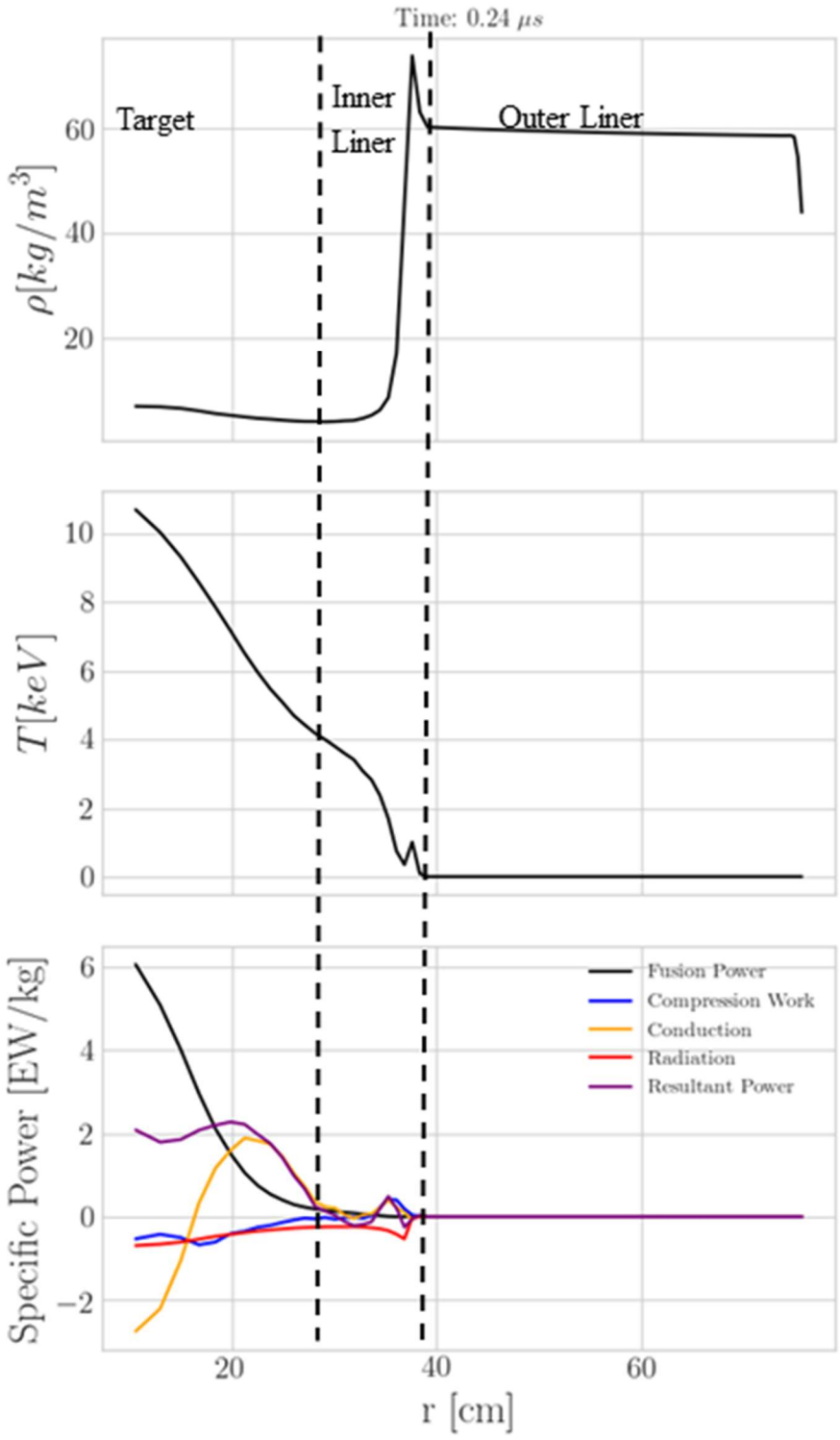

Figure 4-7: Profile of density, temperature, and power balance in the target and liner at 0.24 μs.

Figure 4-8 shows the density, temperature, and power balance at a time of 0.3 μs. The trends of the previous time analysis continued. The density of the target and inner liner had not significantly changed, with the target central density being 6.25 kg/m^3. The target temperature continued its upward rise as fusion power continued to heat the target. The inner liner rose to 8 keV at the target/liner interface and tapered off as it approached the outer liner interface. Fusion power at the center of the target was evenly matched with thermal conduction loss, both at about 12.5 EW/kg in magnitude at the center of the target. Radiation and compressional work were both negative. Target expansion was under way; however, the outer liner was preventing any major expansion of the target. Total energy was positive from the target to the outer liner. The inner liner received thermal conduction from the target and lost energy through conduction to the outer liner. The shock at the interface between the outer and inner liner caused the density at that point to rise to 100 kg/m^3. This impacted the fusion power in the liner in subsequent time steps. Increase in density increased fusion reactivity per Equation 3-6 and assisted in liner heating.

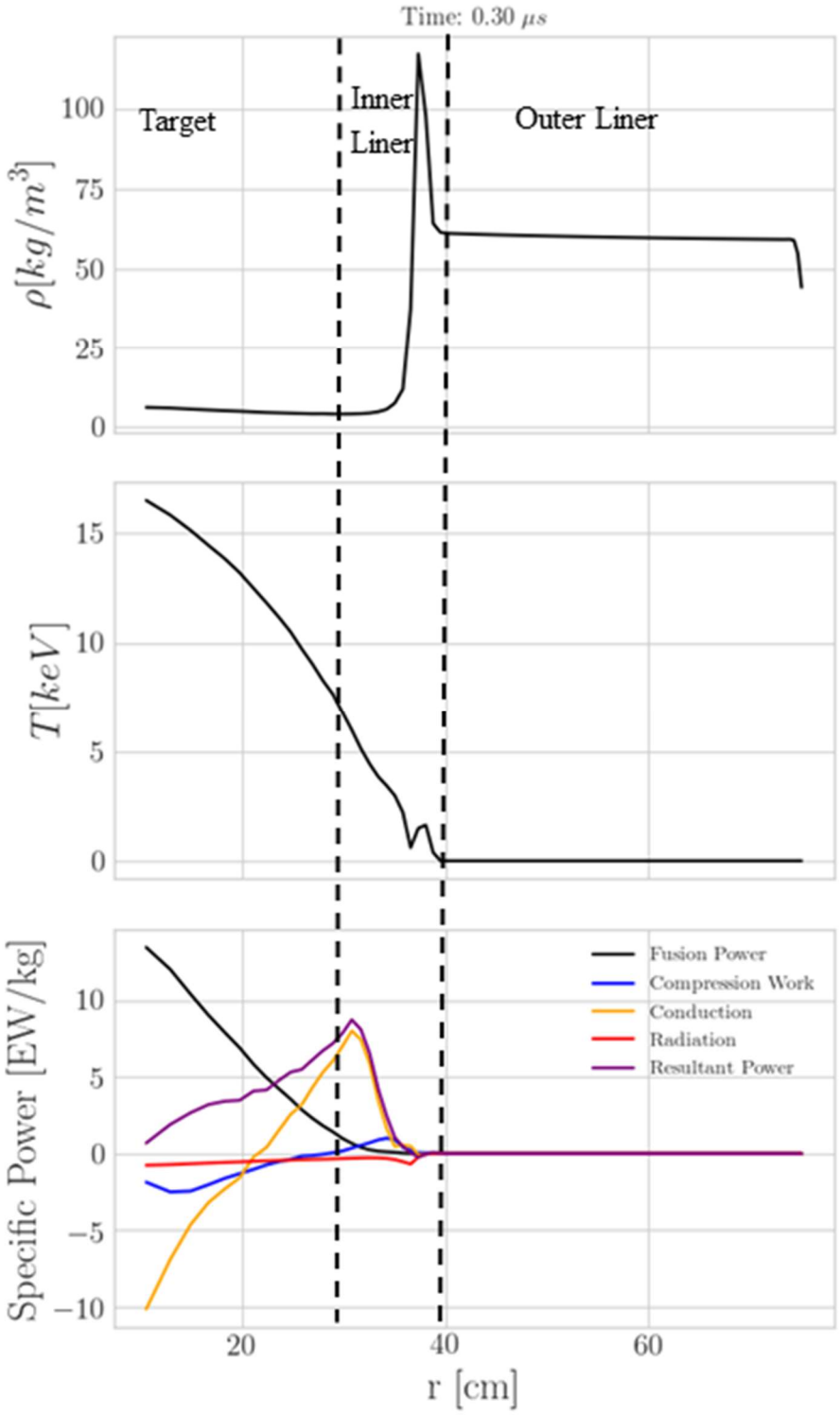

Figure 4-8: Profile of density, temperature, and power balance in the target and liner at 0.3 µs.

Figure 4-9 shows the density, temperature and power balance at 0.34 μs. Again, density did not significantly change; a drop in the central density to 5.25 kg/m^3 occurred. Temperature within the target and inner liner increased. The target central temperature was now 22.5 keV. The rounding of the target temperature profile tapered off and was flatter than previous time steps. The inner liner had significantly increased temperature. The contact point between the inner liner and the target was at 17.5 keV. The majority of the inner liner was at a temperature greater than 10 keV with the contact point between the inner and outer liner dropping to 2.5 keV. This temperature increase in the liner was important because now the total fusion power across the target and inner liner was on the order of 10-20 EW/kg. The inner liner produced fusion power at a level approaching that of the target. The increase in density and temperature of the inner and outer liner caused a rise in fusion reactivity at this point. Thermal conduction caused energy to move from the target to the liner. Compressional work in the target was negative; however, the inner liner was still being compressed by the outer liner. An increase in the compressional work at the inner liner was seen. That the liner produced fusion power and indicated that the liner ignited was in contrast to Parks's research. Parks's research did not show that inner liner burn was possible [5]. Parks's work made several assumptions about the thermal conduction to the liner. First, they assumed that the liner would only receive heating through escaped alpha particles. Next, they assumed either an isobaric model for the inner liner or an isochoric model. Their outcome was the inner liner heated to temperatures less than 1 keV. In contrast, we assumed that thermal conduction to the liner was possible. Instead, the hydrodynamics were allowed to progress based on the physic that occurred between the target and the liner. Parks's model assumed liner densities of

~1000 kg/m^3 at ignition, where our model found liner densities of ~7.5 kg/m^3.This difference in our model allowed for heat transfer from the hot target to the initially cold inner liner. Our model heated the inner liner to temperatures that approached 5 keV. This increase in temperature brought the fusion reactivity up within the inner liner and achieved fusion ignition.

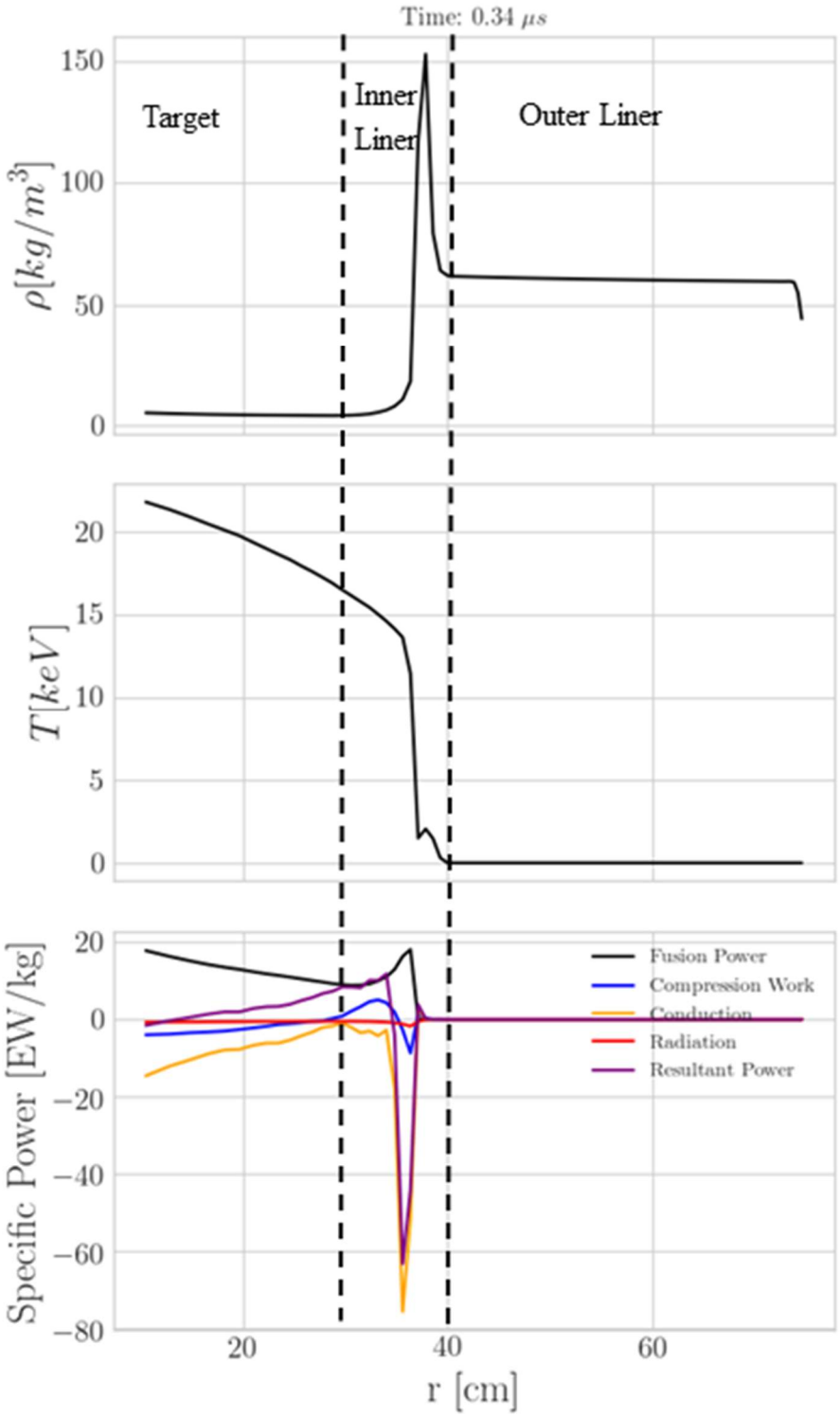

Figure 4-9: Profile of density, temperature, and power balance in the target and liner at 0.34 μs.

Figure 4-10 shows the final density, temperature, and power balance plot for the reference case at 0.37 μs. Target central density continued to drop and was at 4.9 kg/m^3. Inner liner density increased above the target density and was 10 kg/m^3. The temperature of the inner liner surpassed the temperature of the target. The target temperature reached 27 keV and the liner peak temperature reached 30 keV. Fusion power within the target was at 25 EW/kg while the inner liner fusion power peaked at 50 EW/kg. Thermal conduction heated the outer liner, shown by the negative power from the inner liner. The compressional work of the inner liner was positive at the target/liner interface and negative at the inner/outer liner interface. The inner liner attempted to expand both inward and outward radially. The overall power balance from target to middle of the inner liner was positive.

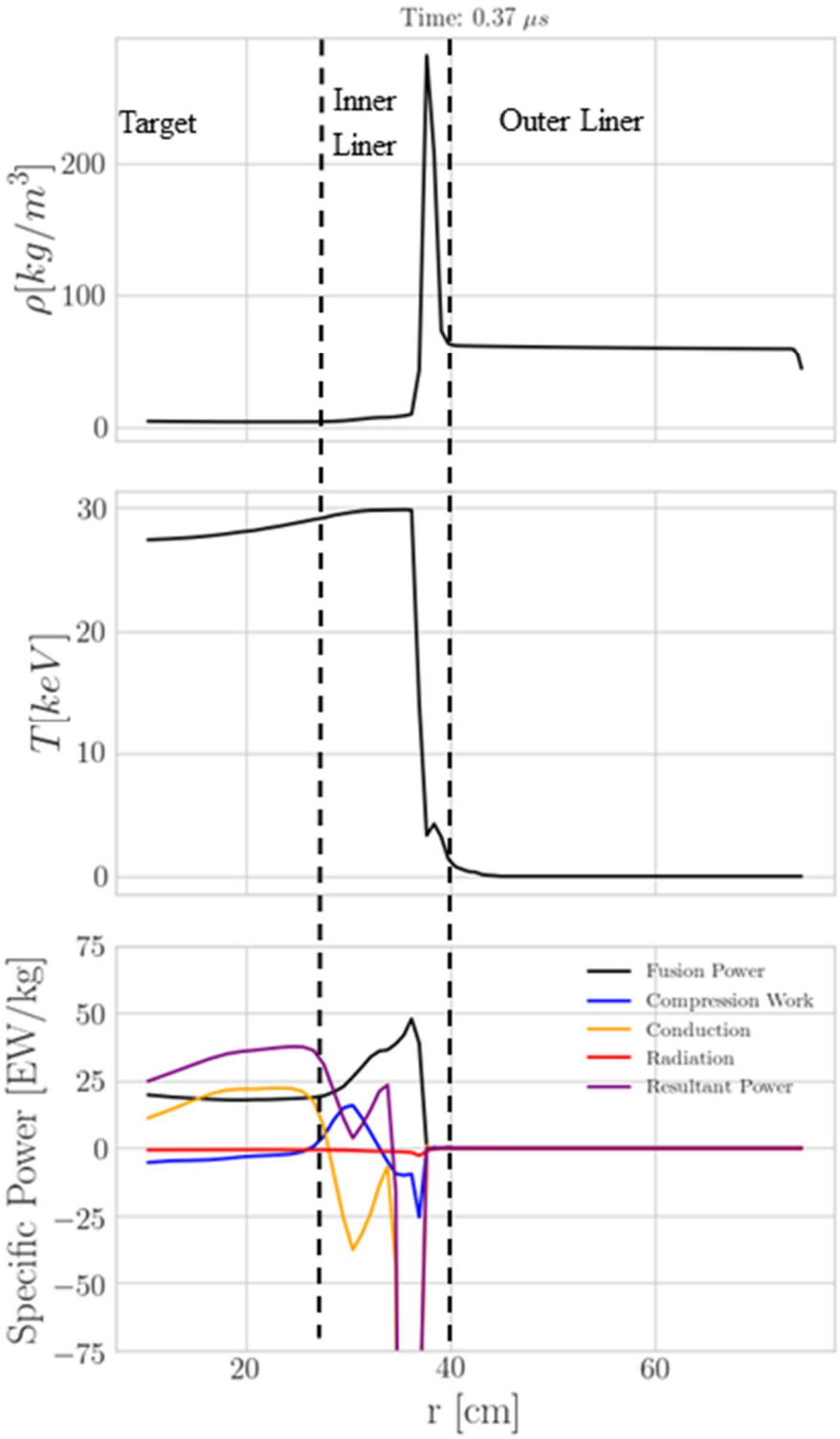

Figure 4-10: Profile of density, temperature, and power balance in the target and liner at 0.37 μs.

Figure 4-11 shows the contour plots of the final state for the reference case. Figure 4-11 (a) shows the density contour plot. The target in the center was at a density of 4.9 kg/m^3. The inner liner ranged from 4.9-80 kg/m^3. The inner liner and outer liner had a shock region that caused the density increase. The shock region was best represented by Figure 4-11 (c) which is the pressure. The central red region was the shock between the inner and outer liner. The target was at a pressure of 5,000 GPa. The outer liner had a 2,000 GPa pressure. The velocity is represented in Figure 4-11 (b). The outer liner continued to compress inwardly at 100 km/s. The central portion of the target was stagnant, but the inner liner expanded outwardly at 400 km/s. The temperature contour is presented in Figure 4-11 (d). Both the target and inner liner were at 30 keV while the outer liner was still very cold at 2.5 eV.

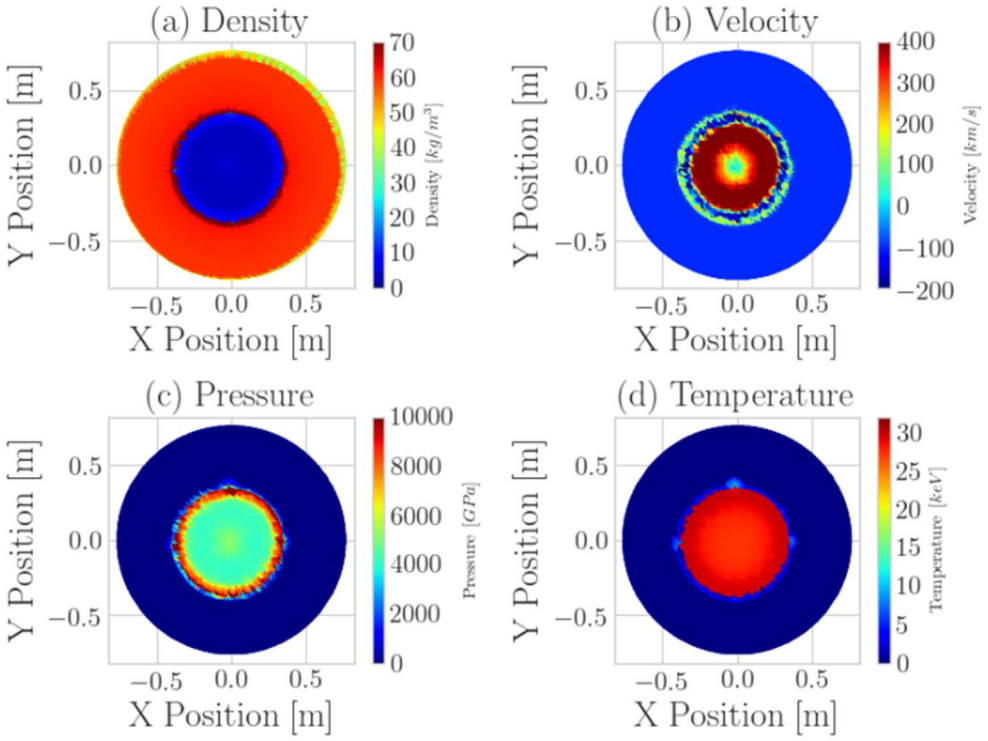

Figure 4-11: Final conditions of the reference case target and liner at a time of 0.37 μs.

Figure 4-12 and Figure 4-13 show the time-dependent change of temperature and density of a central particle in the target. The six time analysis points are plotted on each of the figures. The temperature of the central particle had a continuous increase throughout the ignition process. This was consistent with the temperature changes shown in the radial analysis. While temperature did increase through time, it was not a linear trend with different points changing rate for heating due to the interactions of the power balance terms. The density had a more unique profile. Initially the density increased which was consistent with the target imploding and being compressed by the liner. At 0.14 μs the target density peaked. From that point forward the density decreased. Density decreases were associated with expansion of the target. Target expansion was shown in the compression terms and was seen in the final contour plots shown in Figure 4-11. The

central velocity was stagnant but the inner liner and outer portion of the target were expanding outwardly via their velocity contours.

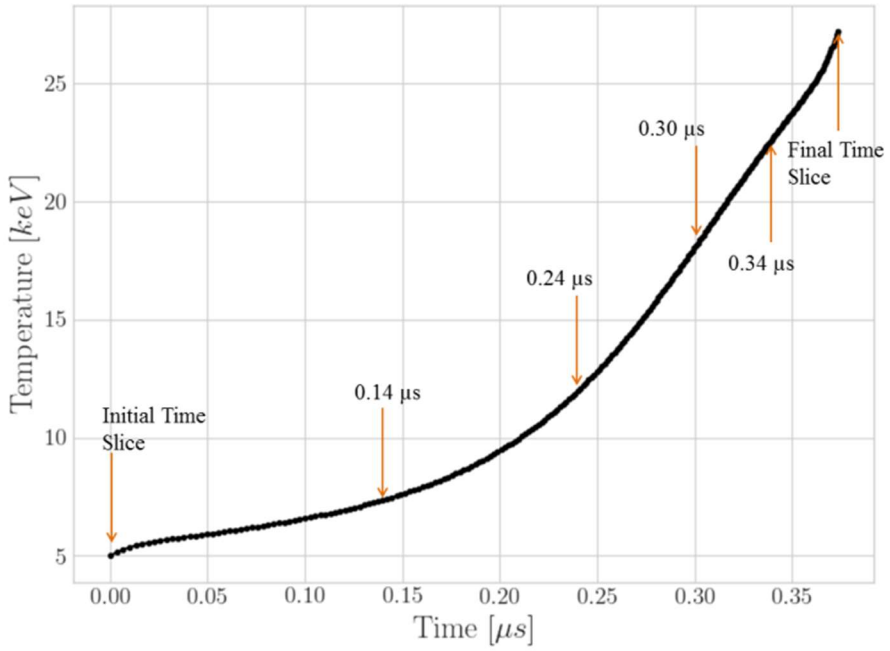

Figure 4-12: Temperature profile in time of a central particle within the target.

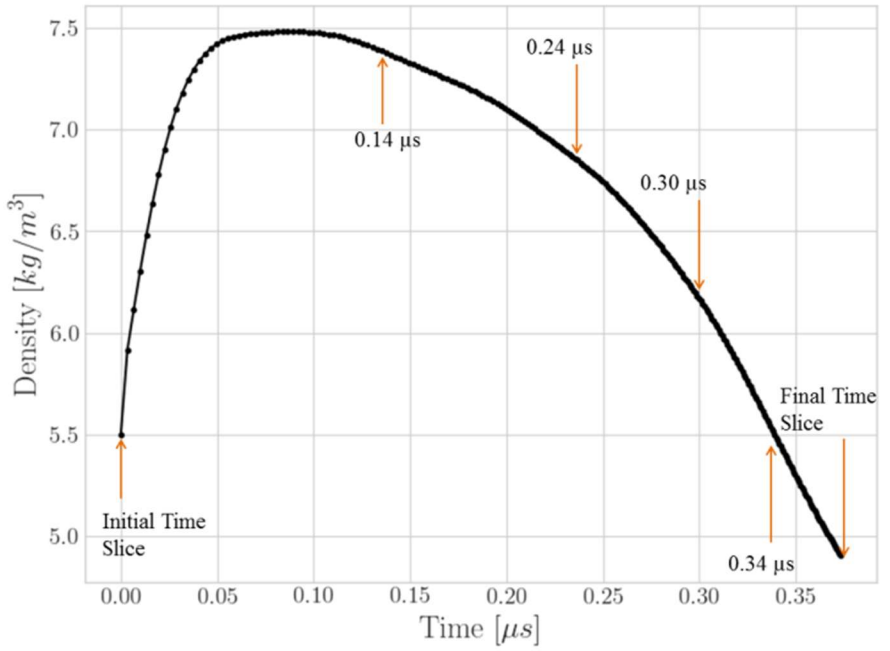

Figure 4-13: Density profile in time of a central particle within the target.

Figure 4-14 was the trajectory of the reference case burn through the ρR vs. T parameter space. The trajectory started at the initial conditions for the reference case. As the case progressed, the increase in temperature caused the target gain to move upward along the T axis of the L-W diagram. The radius of the target was constant through the burn process. This was attributed to the liner compression balanced by balanced by the thermal energy/pressure of the target. The dashed black line represents the liner ignition. The liner density was approximately the same as the target through the burn process. The liner was treated as a sudden increase in target radius and moved the burn trajectory to the right in the ρR axis of the L-W diagram. The progress of the target and liner burn then continued upward along the T axis. The inclusion of liner burn allowed the overall process to move deeper into positive temperature region. The ignition of the liner provided the capability to increase overall yield within the parameter space.

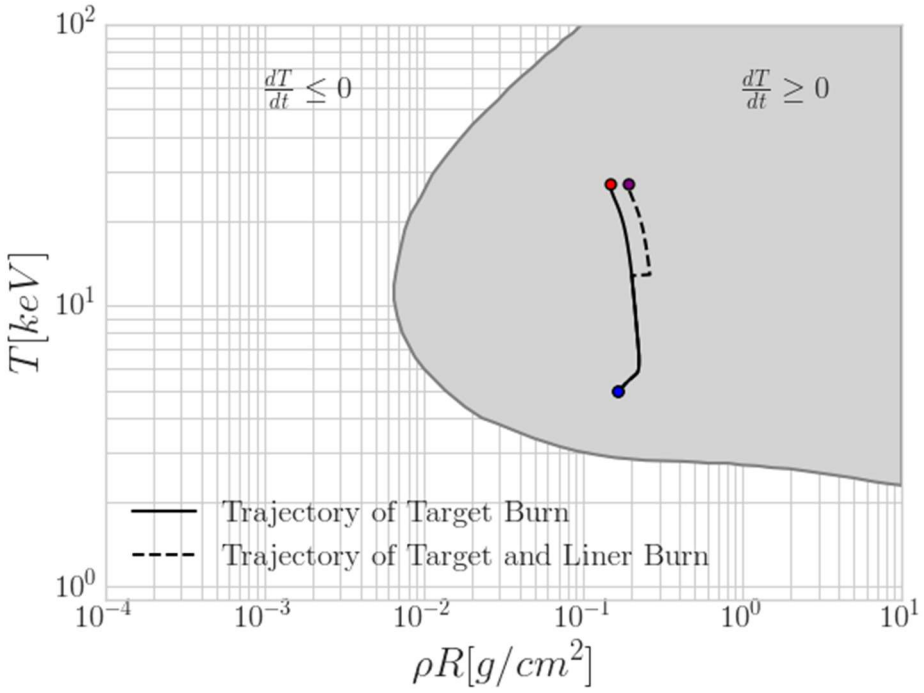

Figure 4-14: The trajectory of the reference case burn through the ρR vs T parameter space. The black line represents the trajectory for only the target burn. The black dashed line represents the inner DT liner ignition augmenting the target burn.

Table 4-2: Parameters varied to determine sensitivity of gain.

Parameter	Case 1	Case 2	Case 3	Case 4	Case 5	Units
Target Density	1	5.5	10	15	20	kg/m^3
Target Temperature	1	2.5	5	7.5	10	keV
Target Radius	1	5	10	20	30	cm
Liner DT:Ar Thickness (r_{in}/r_{total})	9/48	12/48	15/48	20/48	35/48	cm/cm

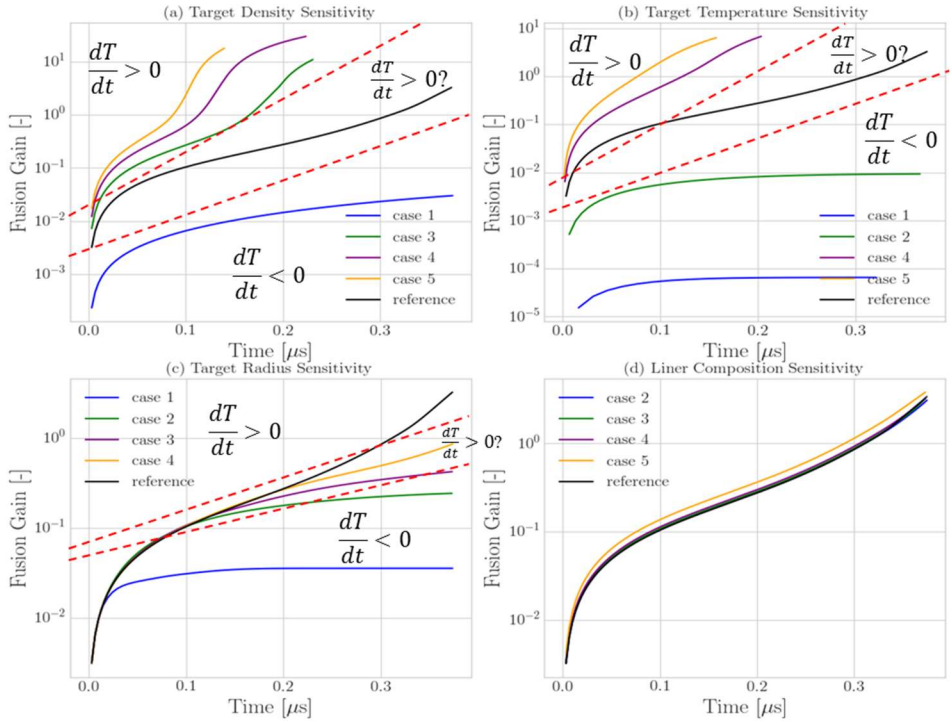

Figure 4-15: Time-dependent gain curves for each of the test parameters. Regions of positive gain, uncertain gain, and no gain are shown in subplots (a)-(c) by the red dashed curves.

4.3 Gain Sensitivity to Target and Liner Parameters

Four critical parameters were varied to understand gain sensitivities. The four parameters varied were the target starting density, the target starting temperature, target starting radius, and liner thickness regions of DT to argon. Table 4-2 provides the varied parameter for each of the test cases. Target density is one of the two parameters that make up the horizontal axis of the L-W diagrams (see Figure 4-3). The ρR term has a direct influence on the region of dT/dt that was reached. The second parameter was initial temperature; this is directly related the vertical axis of the L-W diagrams. A higher initial temperature allowed for greater fusion heating at the initial stages of the process. This was due to the reactivity being a function of the temperature (see Equation 3-6). The third term was the radius of the target and is also contained in the horizontal axis of the

L-W diagrams. The final parameter was the composition of the liner. The increase in DT provided more fuel for the target to heat and potential increase gain, while potentially limiting the Argon liner's confinement time by reducing its thickness. Confinement time was attributed to the liner compressing the target and inner liner and was estimated from Equation 4-3. Once this process stopped the whole system expanded and cooled. The lighter material in the inner liner, which had less inertia, stopped sooner than the heavier argon layer. To keep the analysis consistent all sensitivities were analyzed at the $0.125\ \mu s$ time point. This point was chosen because it provided a reasonable point that all cases pass through and was close to the ignition time of the hot spot provided in Equation 4-2. Figure 4-15 shows the time history of the gain for all cases and outlines three regions. The upper red dashed line delineates a positive gain region that always achieved a gain greater than unity and is represented by the grey region on the L-W diagram in Figure 4-3. A second region, a cusp between positive fusion heating and quenching, is represented between the two dashed red curves. This region lies on the perimeter of the L-W diagram and depending on the physical loss parameters, caused the case to potentially be greater or less than unity. The final region is below the lower red dashed curve and fell outside of the positive temperature gain that is represented by the white region of Figure 4-3. The last set of conditions asymptotically approached a terminal point that was less than unity. These regions existed because of the power balance of the terms in Equation 4-1.

The density/gain sensitivity is the first row in Table 4-2. This case was important because it slid the starting conditions along the horizontal axis in the L-W plot. Density impacted every term of the power balance model. Density influenced the hydrodynamic terms and

influenced how the compression and expansion of the target occurred. Density changes adjusted the fusion power through the number density shown in Equation 3-6. Density also influenced radiation, with increased density increasing radiation loss, shown in Equation 3-12. Finally, density appeared in the thermal conduction term shown in Equation 3-13. Due to density's prevalence its impact on fusion gain was significant. Figure 4-16 shows the density vs gain correlation. The lower regions did not show gain at the evaluation point—which did not mean they did not achieve gain later in the fusion burn process—however, by the later cases gains of greater than unity were achieved. The highest density case showed a gain of almost 12. Increasing density increased the ρR parameter and from Figure 4-3 indicated that gain should increase. The reference case had a ρR space of 0.165, with the highest point having a ρR space of 0.6. Each of these cases was well within the positive heating region of the L-W diagrams. Figure 4-16 indicates that an experiment looking to increase gain should start by adjusting density.

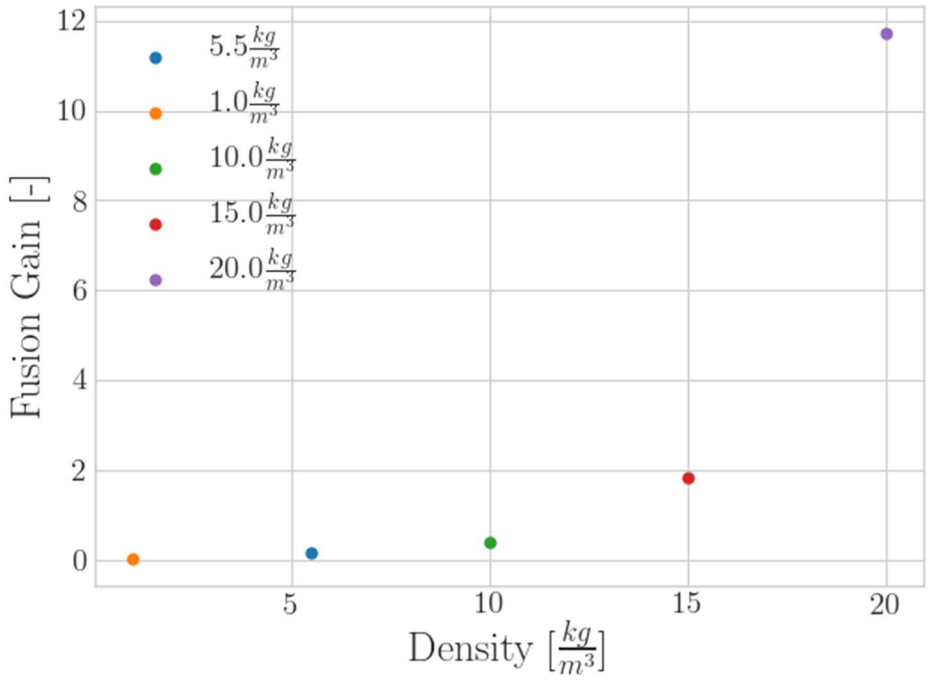

Figure 4-16: Fusion gain vs target starting density.

Figure 4-17 is the sensitivity of the gain to the initial target temperature. This is the second row in Table 4-2, with the starting density varied from 1 to 10 keV. Referencing back to the L-W diagram in Figure 4-3, we varied the vertical axis, with the lower values falling outside the region of positive heating. Like density, temperature was prevalent in all four of the power balance terms. The influential factors for temperature were the fusion power and the thermal conduction. Fusion reactivity was dependent on the temperature with higher temperatures increasing reactivity. Thermal conduction gradients were dependent on temperature differences. The gradients between the target and liner became larger as target temperature increased. Similar to the density sensitivity, lower temperatures did not achieve gain greater than unit at the evaluation point. Unfortunately, the lower temperature values of 1 and 2 keV were below the cusp region shown in Figure 4-15 and quenched the reaction. This was due to them being outside and off the perimeter

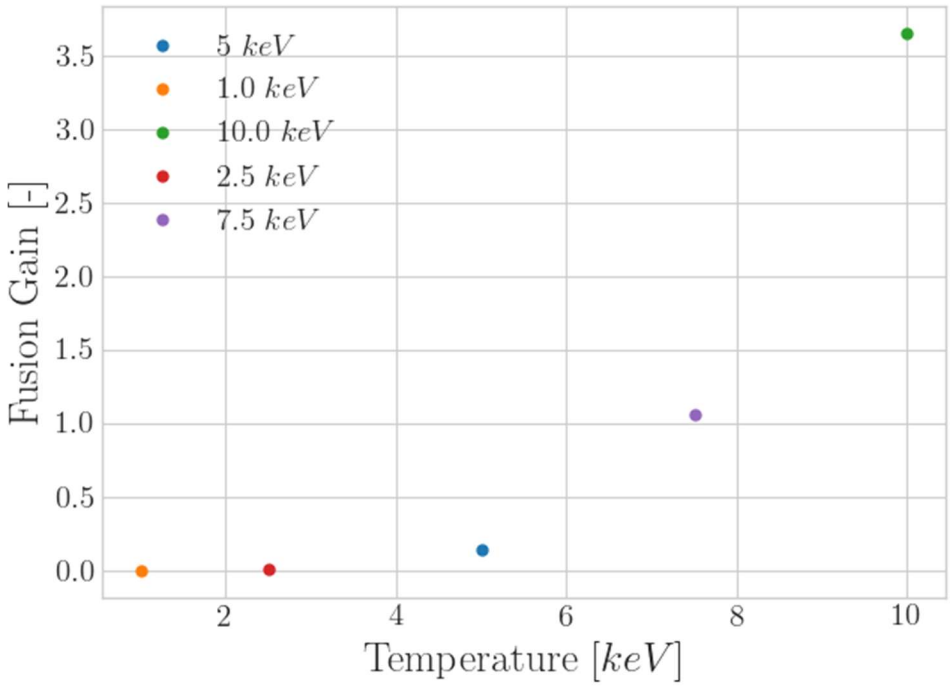

Figure 4-17: Fusion gain vs target starting temperature.

of the L-W diagram. The upper values of 5-10 keV showed a stark improvement in gain. The last two temperatures achieved unity by the evaluation point. This was due to the points being in the positive heating region of the L-W diagrams. The middle case, which is also the reference case, was within the cusp region. The reference case was just inside the lower edge of the positive heating region shown in Figure 4-3. It did not achieve gain at the evaluation point; however, in time it did achieve a gain of three by 0.37 μs. Higher starting temperatures, like higher starting densities, pushed the initial conditions into the positive heating regions of the L-W diagram.

Figure 4-18 represents the fusion gain sensitivity to the variation in target radius. Target radius was the other factor in the horizontal axis of the L-W diagram shown in Figure 4-3. Target radius did not appear explicitly in the power balance terms. Its strongest influence was in the fusion power deposition factor. The energy deposition was dependent on target radius for alpha deposition of energy. Equations 3-7:3-11 were used

to perform the calculations for deposition of energy. Increasing target radius increased alpha deposition by increasing the distance an alpha particle must travel to leave the system. Increased travel distance increased alpha particle collisions and energy transfer. If target density was held constant but its radius was increased, it will slide to the right on Figure 4-3's horizontal axis. If the temperature within the target was above approximately 3 keV and the radius was increased, the power balance will move into the grey positive region. Conversely, lowering the target radius moved the initial conditions left and out of the grey region. Figure 4-18 indicates that the radius impacted the gain at the evaluation point only slightly until the radius was 1 cm. The overall gain through time was more telling. The reference case at 30 cm was the highest achieving gain case out of the radii cases. The next highest gain was only 0.98 for the 20 cm target. The other three cases of 1, 5, and 10 cm targets did not achieve a gain of unity. The 5 and 10 cm cases were inside the grey region of the L-W curve; however, they were on the edge of that curve. Time-dependent processes neglected by the zeroth order model were over-predicting the ignition capabilities of these cases.

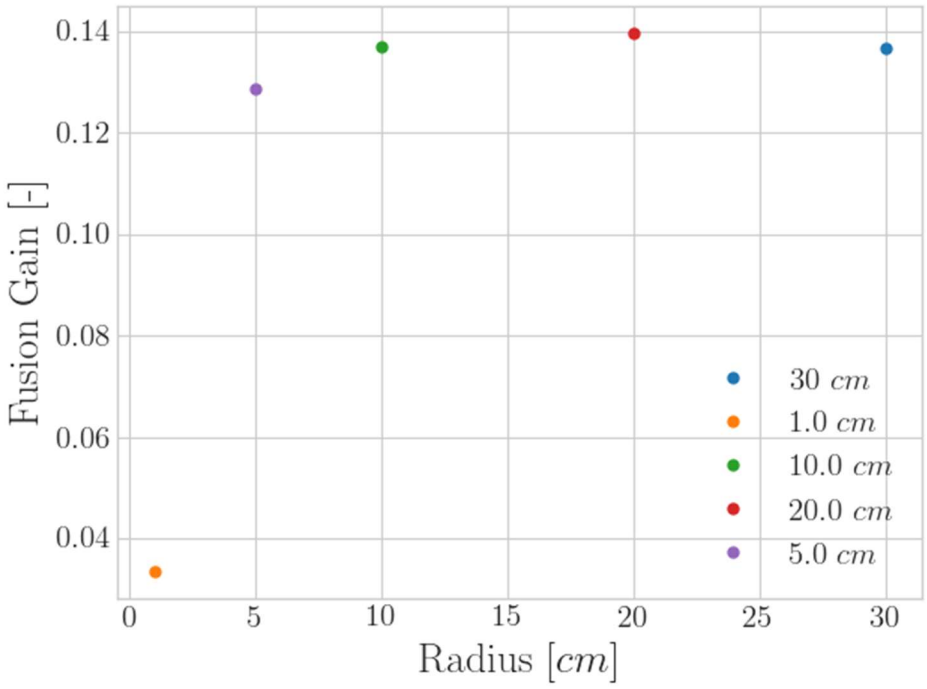

Figure 4-18: This figure shows the impact of changing the initial target radius.

The final sensitivity case is the composition of the liner. Liner composition did not appear in the L-W diagram; however, it was important to the PJMIF modeling community. The ability to augment fusion gain by additional fuel while providing confinement was an additional boon. Several researchers have debated the efficacy of using a cold inner fuel layer to improve fusion gain. Kirkpatrick and Thio predicted that additional gain could be achieved, while Parks's research proved contrary to this statement. One aim of this research was to use the multidimensional physics model to determine if improved gain could be seen through secondary burning of the plasma liner. The time analysis of the reference case showed that heat transfer from the target to the liner did cause the inner liner to ignite and burn. Figure 4-19 shows the gain sensitivity to the liner make up ratio. Increasing the fuel inside the inner liner did increase the gain at

the evaluation point. Figure 4-15 shows that the time history of the gain for each of the mixture cases was very similar; the final case had a slightly greater gain than the other cases. This analysis did not extend the simulations out to the completion of the compression cycle and overall confinement times based on mixture was not evaluated. It is suspected that increased fuel will decrease the confinement time due to the lower inertia of the liner.

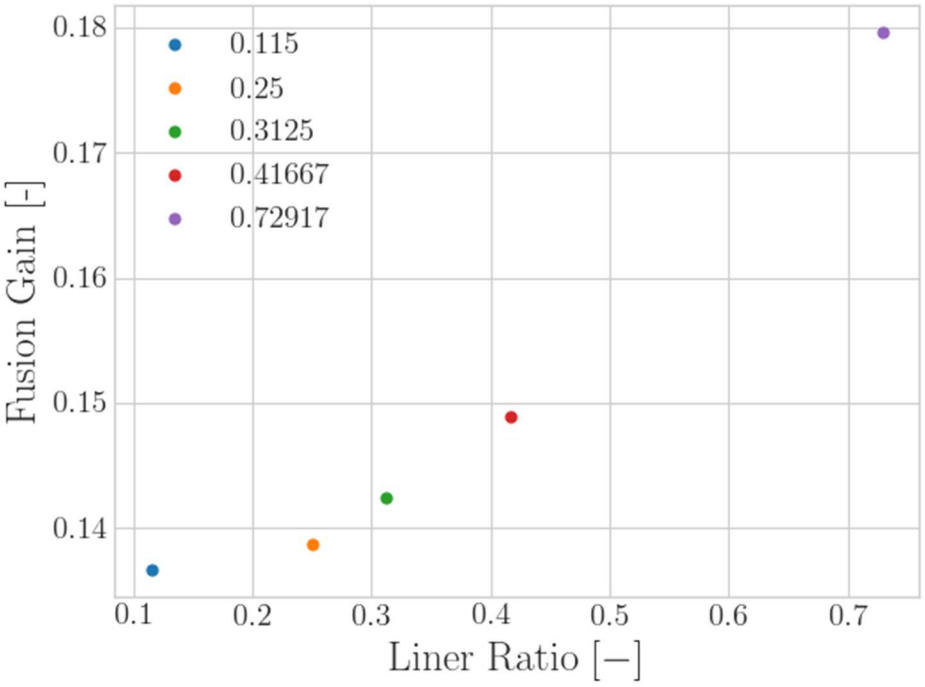

Figure 4-19: Fusion gain is dependent on the composition of the liner.

CHAPTER 5. CONCLUSIONS

A 2D time-dependent simulation of a cylindrical configuration multilayer plasma liner imploding on a magnetized target was performed using an ideal MHD SPH code. This code was augmented with the power balance model terms of the standard Lindl-Widner parameter space: fusion alpha particle deposition, thermal conduction, and Bremsstrahlung radiation. This approach attempts to elucidate the differences between the time-independent 0D analysis of previous work and the multi-dimensional time-dependent effects of the physics involved in the fusion ignition of magnetized targets.

This study verified the 2D code with several standardized test cases. These cases were: the Sod shock tube, the Noh Infinite shock, the Kelvin-Helmholtz instability, the Brio and Wu MHD shock tube, Bremsstrahlung radiation loss, alpha particle deposition from fusion power, and thermal conduction. In these test cases, the error was within 10% of either the analytical or accepted test value. The code was anchored against the numerical experiment of two merging plasma jets performed by Los Alamos National Labs [89]. There was good agreement between the experimental results and the numerical model. The SPH methodology accurately recreated the central density dip. Also, the shock angles and post-shock values of the test case reflected the outcome of the experiments. It was believed that the cause of the undulations was most likely the outcome of a Kelvin-

Helmholtz instability forming, because the thermal expansion and oblique interaction establishes a vertical velocity gradient at the interface, and the growth time is consistent with observed growth of the perturbation [22]. These results provided the framework to move forward with our investigation of the magnetized target ignition problem.

We developed a reference case that consisted of a target at a density of 5.5 kg/m^3, a radius of 30 cm, and a temperature of 5 keV. It was capable of achieving fusion gain of three in 0.375 μs. This case was chosen to be inside the region of positive fusion heating predicted by the L-W power balance. These results indicated that a cold inner liner consisting of deuterium and tritium was able to heat via thermal conduction from the fusing target to ignition temperatures and provide increased fusion yield. The approach showed that the L-W parameter space correctly anticipates a gain over unity of a magnetized target; however, the compressional work that is traditionally calculated using self-similar principles over-predicts the capabilities of liner compression effects. Our analysis did not find the liner capable of compressing a target to fusion ignition conditions; however, the liner was able to provide confinement to an already thermally conditioned target.

Gain sensitivities were conducted by performing a parametric analysis around the reference case, and the results were compared to the L-W power balance model to assess L-W predictions to time-dependent calculations. There were 16 cases performed in which the initial target: density, temperature, radius, and inner/outer liner thickness ratio were varied. Increased density or temperature increased overall yield, and shortened the time to

reach break-even conditions, consistent with the L-W modeling. A factor of four target density increase led to a four times increase in gain when measured against the reference case. Doubling target temperature led to break-even conditions an order of magnitude sooner than the reference case. When the target radius was decreased, gain dropped, which trended similar to the L-W predictions. The lowest target radius of 1 cm, led the target to cool rapidly and unable to achieve appreciable fusion reactions. Liner ratio was varied and demonstrated that increased inner liner thickness (DT) could increase yield at the observation point, but has the trade-off that it may lower target confinement times. These results point to a need to explore higher density and temperature regions for the starting point of PJMIF. Radiation and thermal conduction remain the important loss terms and validate Kirkpatrick's earlier assumptions [31]. The outcome of this study found that the sensitives agreed with the earlier L-W predictions, namely that fusion power must balance the radiative and thermal conduction losses.

In summary of the 2D MHD results, the time-dependent analysis provided new insight into the complex burn physics and transfer of energy between the target and the liner. Most importantly, this study found that burning of a cold fuel layer is possible. This is significant because it opens the possibility for high gain MIF targets in cylindrical geometries. To achieve gain over unity, starting temperatures of 5 keV in the target were necessary. Cylindrical targets do not have the more favorable $1/r^2$ compression seen in spherical targets. This difference could be the reason for the failed compression ignition of the cases studied in the work presented here. Future work should focus on plasma liner

compression of the target and other heating mechanisms to determine how sufficient hot spot temperatures can be reached in these geometries. Also, effects of the magnetic field should be explored for control of thermal conduction and tuning of liner burn coupled with target ignition.

REFERENCES

[1] J. Cassibry, R. Cortez, M. Stanic, A. Watts, W. Seidler, R. Adams, G. Statham and L. Fabisinski, "Case and Developement Path for Fusion Propulsion," *Journal of Spacecraft and Rockets,* vol. 52, no. 2, pp. 595-612, 2015.

[2] J. T. Cassibry, M. Stanic, S. C. Hsu, S. I. Abarzhi and F. D. Witherspoon, "Tendency of Spherically Imploding Plasma Liners Formed by Merging Plasma Jets to Evolve Toward Spherical Symmetry," *Physics of Plasmas,* vol. 19, no. 5, 2012.

[3] K. Hyougkeun, R. Samulyak, L. Zhang and P. Parks, "Influence of Atomic Processes on the Implosion of Plasma Liners," *Physics of Plasmas,* vol. 19, no. 5, 2012.

[4] S. A. Slutz, M. C. Hermann, R. A. Vesey, A. B. Sefkow, D. B. Sinars, D. C. Rovang, K. J. Pererson and M. E. Cuneo, "Pulsed-Power-Driven cylindrical Liner Implosions of laser preheated fuel Magnetized with an Axial Field," *Physics of Plasmas,* vol. 17, no. 5, 2010.

[5] P. B. Parks, "On the Efficacy of Imploding Plasma Liners for Magnetized Fusion Target Compression," *Physics of Plasmas,* vol. 15, no. 6, 2008.

[6] M. M. Basko, A. J. Kemp and J. Meyer-ter-vehn, "Ignition conditions for magnetized target fusion in cylindrical geometry," *Nuclear Fusion,* vol. 40, no. 1, pp. 59-68, 2000.

[7] R. C. Kirkpatrick, "Magnetized Target Fusion for Advanced Space Propulsion," in *Space Technology and Applications International Forum 18th Symposium on Space Nuclear Power and Propulsion*, Albuquerque, 2001.

[8] R. C. Kirkpatrick, "A Tutorial on Ignition and Gain for Small Fusion Targets," in *7th Symposium on Current Trends in International Fusion Research*, Washington DC, 2007.

[9] R. C. Kirkpatrick, "Ignition critical profiles for small fusion targets," *Nuclear Fusion,* vol. 21, no. 11, pp. 1457-1466, 1981.

[10] C. E. Knapp and R. C. Kirkpatrick, "Possible Energy Gainfor Plasma Liner Driving Maneto-inertial Fusion Concept," *Physics of Plasmas,* vol. 21, no. 7, 2014.

[11] I. R. Lindemuth and R. C. Kirkpatrick, "PARAMETER SPACE FOR MAGNETIZED FUEL TARGETS IN INERTIAL CONFINEMENT FUSION," *Nuclear Fusion,* vol. 23, no. 3, pp. 263-284, 1983.

[12] I. R. Lindemuth, "The Ignition DesignSpace of Magnetized Target Fusion," *Physics of Plasmas,* vol. 22, no. 12, 2015.

[13] J. D. Lindl, "Physics of Ignition for ICF Capsules," in *Inertial Confinement Fusion Course and Workshop*, Yarenna, 1989.

[14] S. B. Thompson, Lindl-Widner Diagrams for Plasma Liner Driven Magneto-inertial Fusion, Huntsville: University of Alabama in Huntsville, 2007.

[15] A. Case, S. Messer, S. Brockington, F. D. Witherspoon and R. Elton, "Merging of High Speed Argon Plasma Jets," *Physics of Plasmas,* vol. 20, no. 1, 2013.

[16] R. C. Kirkpatrick and J. A. Wheeler, "The physics of DT ignition in small fusion targets," *Nuclear Fusion,* vol. 21, no. 3, p. 389, 1981.

[17] R. C. Kirkpatrick, I. R. Lindemuth and M. S. Ward, "Magnetized Target Fusion: An Overview," *Fusion Technology,* vol. 27, no. 3, pp. 201-214, 1995.

[18] G. A. Wurden, T. P. Intrator, J. M. Taccetti, S. Zhang, S. C. Hsu, Z. Wang, W. Waganaar, D. W. Begay, M. G. Tuszewski, C. Grabowski, J. Degnan, E. Ruden and B. Martinez, "FRX-L: A Plasma Injector for Magnetized Target Fusion," Los Alamos National Labs, Los Alamos, 2003.

[19] J. M. Taccetti, T. P. Intrator, G. A. Wurden, S. Y. Zhang, R. Aragonez, P. N. Assmus, C. M. Bass, C. Carey, S. A. deVries, W. J. Fienup, S. C. Hsu, M. P. Kozar, M. C. Langner, J. Liang, R. J. Maqueda, R. A. Martinez, P. G. Sanchez, K. F. Schoenberg, K. J. Scott, R. E. Siemon, E. M. Tejero, E. H. Trask, M. Tuszewski and W. J. Waganaar, "FRX-L: A field-reversed configuration plasma injector for magnetized target fusion," *Review of Scientific Instruments,* vol. 74, no. 10, 2003.

[20] S. Hsu, F. D. Witherspoon, J. Cassibry, M. Gilmore, R. Samulyak and P. Stoltz, "The PLX-α Project: Progress and Plans," in *APS Division of Plasma Physics Meeting 2016*, San Jose, 20166.

[21] F. Y. Thio, C. E. Knapp, C. E. Kirkpatrick, R. E. Siemon and P. J. Turchi, "A Physics Exploratory Experiment on Plasma Liner Formation," *Journal of Fusion Energy,* vol. 20, no. 1, pp. 1-11, 2001.

[22] S. Thompson and J. Cassibry, "Effects of propagation distance and half angle on the merging of hypervelocity plasma jets," *Physics of Plasmas,* vol. 26, no. 5, pp. 052701-1 - 052701-12, 2019.

[23] Y. C. Thio, "Magnetized Target Fusion in a Spheroidal Geometry with Standoff Drivers," in *2nd Int. Symp. Current Trends Int. Fusion Res.*, 1999.

[24] J. P. Friedberg, Plasma Physics and Fusion Energy, Cambridge: Cambridge University Press, 2007.

[25] H. Goedbloed and S. Poedts, Principles of Magnetohydrodynamics, Cambridge: Cambridge University Press, 2004.

[26] R. J. Goldston and P. H. Rutherford, Introduction to Plasma Physics, New York: Taylor & Francis Group, 1995.

[27] F. F. Chen, Introduction to Plasma Physics and Controlled Fusion Volume 1: Plasma Physics, New York: Plenum Press, 1984.

[28] J. D. Huba, "NRL Plasma Formulary," Naval Research Laboratory, Washington D.C., 2016.

[29] R. C. Kirkpatrick, C. C. Cremer, L. C. Madson, H. H. Rogers and R. S. Cooper, "Sturctured Fuison Target Designs," *Nuclear Fusion,* vol. 15, no. 2, p. 333, 1975.

[30] J. D. Anderson, Modern Compressible Flow With Historical Perspective, Boston: McGraw-Hill, 2003.

[31] R. C. Kirkpatrick, "An overview of design space for small fusion Targets," *Nuclear Fusion,* vol. 19, no. 1, pp. 69-79, 1979.

[32] R. B. Lazarus and R. D. Richtmyer, "Similarity Solutions for Converging Shocks,"

Los Alamos National Labs, Los Alamos, 1977.

[33] I. R. Lindemuth and M. M. Widner, "Magnetohydrodynamic behavior of thermonuclear fuel in a preconditioned electron," *Physics of Fluids,* vol. 24, no. 4, p. 746, 1981.

[34] I. R. Lindemuth and R. E. Siemon, "The fundamental parameter space of controlled thermonuclear fusion," *American Journal of Physics,* vol. 77, no. 5, p. 407, 2009.

[35] S. Lagendorf, S. C. Hsu and S. J. Langendorf, "Semi-analytic model of plasma-jet-driven magneto-inertial fusion," *Physics of Plasmas,* vol. 24, no. 3, 2017.

[36] R. Samulyak, P. Parks and L. Wu, "Spherically symmetric simulation of plasma liner driven magnetoinertial fusion," *Physics of Plasmas,* vol. 17, no. 9, pp. 1-10, 2010.

[37] S. A. Slutz, C. A. Jennings, T. J. Awe, G. A. Shipley, B. T. Hutsel and D. C. Lamppa, "Auto-magnetizing liners for magnetized inertial fusion," *Physics of Plasmas,* vol. 24, no. 1, 2017.

[38] S. A. Slutz and R. A. Vesey, "High-Gain Magnetized Inertial Fusion," *Physical Review Letters,* vol. 108, no. 2, 2012.

[39] D. J. Price, "Smoothed Particle Hydrodynamics and Magnetohydrodynamics," *Journal of Computational Physics,* vol. 231, no. 3, pp. 759-794, 2012.

[40] S. Vanaverbeke, R. Keppens and S. Poedts, "GRADSPMHD: A Parallel MHD Code Based on the SPH Formalism," *Computer Physics Communications,* vol. 185, no. 3, pp. 1053-1073, 2014.

[41] J. D. Lawson, "Some Criteria For a Useful Thermonuclear Reactor," Atomic Energy

Research Establishment, Harwell, Berkshire, U. K., 1955.

[42] S. I. Braginskii, Transport Process in a Plasma, New York: Consultants Bureau, 1965.

[43] L. Spitzer and R. Harm, "Transport phenomena in a completely ionized gas," *Physical Review,* vol. 89, no. 5, p. 977, 1953.

[44] R. A. Gingold and J. J. Monaghan, "Smoothed particle hydrodynamics: theory and application to non-spherical stars," *Monthly Notices of the Royal Astronomical Society,* vol. 181, pp. p. 375-389, 1977.

[45] J. J. Monaghan, "Smoothed Particle Hydrodynamics," *Annual Reviews in Astrophysics,* vol. 30, pp. 543-574, 1992.

[46] L. B. Lucy, "A numerical approach to the testing of the fission hypothesis," *Astronomical Journal,* vol. 82, pp. p. 1013-1024, 1977.

[47] T. Weaver and Z. Xiao, "Fluid Simulation by the Smoothed Particle Hydrodynamics Method: A Survey," in *11th International Conference on Computer Graphics Theory and Application*, Valletta, Malta, 2016.

[48] M. Ihmsen, J. Orthmann, B. Solenthaler, A. Kolb and M. Teschner, "SPH Fluids in Computer Graphics," Eurographics, 2014.

[49] M. B. Liu and G. R. Liu, "Smoothed Particle Hydrodynamics (SPH): an Overview and Recent Developments," *Archives of Computational Methods in Engineering,* vol. 17, no. 1, pp. 25-76, 2010.

[50] G. Liu and M. Liu, Smoothed Particle Hydrodynamics: A Meshfree Particle Method, 2003.

[51] D. Garcia-Senz, R. M. Cabezon and J. A. Escartin, "Improving Smoothed Particle Hydrodynamics with an Integral Approach to Calculating Gradients," *Astronomy & Astrophysics,* vol. 538, 2012.

[52] S. Rosswog, "SPH Methods in the Modelling of Compact Objects," *Living Rev Comput Astrophys,* 2015.

[53] G. E. Fasshauer, Meshfree Approximation Methods with MATLAB, Hackensack: World Scientific Publishing Co, 2007.

[54] L. D. Sigalotti, H. Lopez, A. Donoso, E. Sira and J. Klapp, "A Shock Capturing SPH Scheme Based on Adaptive Kernel".

[55] M. B. Liu and G. R. Liu, "Restoring particle consistency in smoothed particle hydrodynamics," *Applied Numerical Mathematics,* vol. 56, no. 1, pp. 19-36, 2006.

[56] W. Dehnen and H. Aly, "Improving convergence in smoothed particle hydrodynamics simulations without pairing instability," *Monthly Notices of the Royal Astronomical Society,* vol. 425, pp. 1068-1082, 2012.

[57] J. Monaghan, "Smoothed particle hydrodynamics," *Reports on Progress in Physics,* vol. 68, pp. 1703-1759, 2005.

[58] D. Avesani, M. Dumbser and A. Bellin, "A New Class of Moving-Least-Squares WENO-SPH schemes," *Journal of Computational Physics,* pp. 278-299, 2014.

[59] N. Frontiere, C. D. Raskin and J. M. Owen, "CRKSPH-A Conservative Reproducing Kernel Smoothed Hydrodynamics Scheme," *Journal of Computational Physics,* vol. 332, pp. 160-209, 2017.

[60] J. P. Vila, "On Particle Weighted Methods And Smooth Particle Hydrodynamics,"

Mathematical Models and Methods in Applied Sciences, vol. 9, no. 2, pp. 161-209, 1999.

[61] B. B. Moussa, N. Lanson and J. P. Vila, "Convergence of Meshless Methods for Conservation Laws Applications to Euler equations," *Hyperbolic Problems: Theory, Numerics, Applications,* 1999.

[62] P. F. Hopkins, "A General Class of Lagrangian Smoothed Particle HydrodynamicsMethods and Implications for Fluid Mixing Problems," *Monthly Notices of the Royal Astronomical Society,* vol. 428, no. 4, pp. 2840-2856, 2013.

[63] H. Wendland, "Piecewise polynomial, positive definite and compactly supported radial functions of minimal degree," *Advances in Computational Mathematics,* 1995.

[64] V. Springel and L. Hernquist, "Cosmological smoothed particle hydrodynamics simulations: the entropy equation," *Monthly Notices of the Royal Astronomical Society,* vol. 333, no. 3, pp. 649-664, 2002.

[65] S. Rosswog and D. Price, "MAGMA: a three-dimensional, Lagrangian magnetohydrodynamics code for merger applications," *Monthly Notices of the Royal Astronomical Society,* vol. 379, no. 3, pp. 915-931, 2007.

[66] L. Hernquist and N. Katz, "TREESPH-A unification of SPH with the hierachical tree method," *Astrophysical Journal Supplement Series,* vol. 70, pp. 419-446, 1989.

[67] J. J. Monaghan and D. J. Price, "Variational principles for relativistic smoothed particle hydrodynamics," *Monthly Notices of the Royal Astronomical Society,* vol. 328, no. 2, pp. 381-392, 2001.

[68] P. J. Morrison, "Hamiltonian description of the ideal fluid," *Reviews of Modern*

Physics, vol. 70, no. 2, pp. 467-521, 1998.

[69] D. A. Wells, Lagrangian Dynamics, New York: McGraw-Hill, 1967.

[70] D. E. Kirk, Optimal Control Theory, Englewood Cliffs: Dover, 2004.

[71] Y. Imaeda and S.-i. Inutsuka, "SHEAR FLOWS IN SMOOTHED PARTICLE HYDRODYNAMICS," *The Astrophysical Journal,* vol. 569, no. 1, pp. 501-518, 2002.

[72] S. -H. Cha and A. P. Whitworth, "Implementations and tests of Godunov-type particle hydrodynamics," *Monthly Notices of the Royal Astronomical Society,* vol. 340, no. 1, p. 73–90, 2003.

[73] J. J. Monaghan, "SPH and Riemann Solvers," *Journal of Computational Physics,* vol. 136, no. 2, pp. 298-307, 1997.

[74] S. I. Inutsuka, "Reformulation of Smoothed Particle Hydrodynamics with Riemann Solver," *Journal of Computational Physics,* vol. 179, pp. 238-267, 2002.

[75] J. J. Monaghan, "SPH without a Tensile Instability," *Journal of Computational Physics,* vol. 159, no. 2, pp. 290-311, 2000.

[76] S. Borve, M. Omang and J. Trulsen, "Two-dimensional MHD Smoothed Particle Hydrodynamics Stability Analysis," *The Astrophysical Journal,* vol. 153, no. 2, p. 447–462, 2004.

[77] S. Borve, M. Omang and J. Trulsen, "Regularized Smoothed Particle Hydrodynamics: A New Approach to Simulating Magnetohydrodynamic Shocks," *The Astrophysical Journal,* vol. 561, no. 1, p. 82»93, 2001.

[78] L. Cullen and W. Dehnen, "Inviscid Smoothed Particle Hydrodynamics," *Monthly*

Notices of the Royal Astronomical Society, vol. 408, no. 2, pp. 669-683, 2010.

[79] D. J. Price, "Smoothed Particle Hydrodynamics Things I wish my mother taught me," 2011.

[80] P. W. Cleary and J. J. Monaghan, "Conduction Modelling Using Smoothed Particle Hydrodynamics," *Journal of Computational Physics,* vol. 148, no. 1, pp. 227-264, 1999.

[81] M. Jubelgas, V. Springel and K. Dolag, "Thermal conduction in cosmological SPH simulations," *Monthly Notices of the Royal Astronomical Society,* vol. 351, no. 2, pp. 423-435, 2004.

[82] G. A. Sod, "Survey of several finite difference methods for systems of nonlinear hyperbolic conservation laws," *Journal of Computational Physics,* vol. 26, no. 4, pp. 1-31, 1978.

[83] W. F. Noh, "Errors for calculations of strong shocks using artificial viscosity and an artificial heat flux," *Journal of Computational Physics,* vol. 72, no. 1, pp. 78-120, 1987.

[84] M. Gehmeyr, B. Cheng and D. Mihalas, "Noh's constant-velocity shock problem revisited," *Shock Waves,* vol. 7, no. 5, pp. 255-274, 1997.

[85] S. Valcke, S. D. Rijcke, E. Rodiger and H. Dejonghe, "Kelvin-Helmholtz Instabilities in Smoothed Particle Hydrodynamics," *Monthly Notices of the Royal Astronomical Society,* vol. 408, no. 1, pp. 71-86, 2010.

[86] D. J. Price, "Modelling discontinuities and Kelvin–Helmholtz instabilities in SPH," *Journal of Computational Physics,* vol. 227, no. 24, pp. 10040-10057, 2008.

[87] C. P. McNally, W. Lyra and J.-C. Passy, "A WELL-POSED KELVIN–HELMHOLTZ INSTABILITY TEST AND COMPARISON," *The Astrophysical Journal Supplement Series,* vol. 201, no. 18, p. 17pp, 2012.

[88] S. Chandrasekhar, Hydrodynamic and Hydromagnetic Stability, New York: Oxford University Press, 1961.

[89] E. C. Merritt, A. L. Moser, S. C. Hsu, C. S. Adams, J. P. Dunn, A. M. Holgado and M. A. Gilmore, "Experimental evidence for collisional shock formation via two obliquely merging supersonic plasma jets," *Physics of Plasmas,* vol. 21, no. 5, 2014.

[90] A. Nassiri, A. Vivek, T. Abke, B. Liu, T. Lee and G. Daehn, "Depiction of Interfacial Morphology in impact welded Ti/Cu bimetalic systems using smoothed particle hydrodynamics," *Applied Physics Letters,* 2017.

[91] D. C. Pack, "The Motion of a Gas Cloud Expanding Into A Vacuum," *Monthly Notices of the Royal Astronomical Society,* vol. 113, pp. 43-51, 1952.

[92] M. Brio and C. C. Wu, "An upwind differencing scheme for the equations of ideal magnetohydrodynamics," *Journal of Computational Physics,* vol. 75, no. 2, pp. 400-422, 1988.

[93] J. M. Stone, J. F. Hawley, C. R. Evans and M. L. Norman, "A Test Suite for Magnetohydrodynamical Simulations," *The Astrophysical Journal,* vol. 388, pp. 415-437, 1992.

[94] M. M. Widner, "Fuel Energy Balance Studies of Pellet Ignition Requirements," Sandia Laboratories, Albuquerque, 1979.

[95] S. Atenzi and J. Meyer-Ter-Vehn, Inertial Fusion: Beam Plasma Interaction,

Hydrodynamics, Dense Plasmas, Oxford: Oxford University Press, 2004.